

A SEARCH FOR SUPERSYMMETRY IN EVENTS WITH A Z
BOSON, JETS, AND MISSING TRANSVERSE ENERGY IN $p - p$
COLLISIONS WITH $\sqrt{s}=13$ TEV WITH THE ATLAS DETECTOR

TOVA RAY HOLMES



Physics Department
University of California, Berkeley

August 2016 – version 1.0

Tova Ray Holmes: *A Search for Supersymmetry in Events with a Z Boson, Jets, and Missing Transverse Energy in $p - p$ Collisions with $\sqrt{s}=13$ TeV with the ATLAS Detector*, © August 2016

ABSTRACT

PUBLICATIONS

Some ideas and figures have appeared previously in the following publications:

Put your publications from the thesis here. The packages `multibib` or `bibtopic` etc. can be used to handle multiple different bibliographies in your document.

ACKNOWLEDGEMENTS

Put your acknowledgements here.

CONTENTS

I INTRODUCTION	1
1 INTRODUCTION	3
II THEORY AND MOTIVATION	5
2 THEORY AND MOTIVATION	7
2.1 The Standard Model	7
2.1.1 Matter	8
2.1.2 Forces	10
2.1.3 Phenomenology of Proton-Proton Collisions	17
2.1.4 Problems in the Standard Model	19
2.2 Supersymmetry	20
2.2.1 The Minimal Supersymmetric Standard Model	21
2.2.2 Solutions to Standard Model Problems	23
2.2.3 Simplified Models of Supersymmetry	24
2.3 Monte Carlo Generation	25
III THE EXPERIMENT	29
3 THE LARGE HADRON COLLIDER	31
3.1 The Injector Complex	32
3.2 Operation of the Large Hadron Collider	33
3.3 Luminosity	35
3.4 Pile-up in proton-proton Collisions	37
4 THE ATLAS DETECTOR	39
4.1 Coordinate System Used in the ATLAS Detector	39
4.2 The Inner Detector	40
4.2.1 The Pixel Detector	40
4.2.2 The Silicon Microstrip Tracker	42
4.2.3 The Transition Radiation Tracker	42
4.3 The Calorimeters	43
4.4 The Muon Spectrometer	44
4.5 The Magnet System	47
4.6 The Trigger System and Data Acquisition	48
5 OBJECT RECONSTRUCTION IN THE ATLAS DETECTOR	53
5.1 Electrons	53
5.2 Photons	55
5.3 Muons	57
5.4 Jets	59
5.5 Overlap Removal	63
5.6 Missing Transverse Energy	63
6 APPLICATION OF A NEURAL NETWORK TO PIXEL CLUSTERING	65
6.1 Clustering in the Pixel Detector	65

6.1.1	Charge Interpolation Method	66
6.1.2	Improving Measurement with Neural Networks	66
6.2	Impact of the Neural Network	67
6.2.1	The Neural Network in 13 TeV Data	68
IV	SEARCHING FOR SUPERSYMMETRY	73
7	BACKGROUND PROCESSES	75
7.1	Data and Monte Carlo Samples	77
8	OBJECT IDENTIFICATION AND SELECTION	79
8.1	Electrons	79
8.2	Muons	80
8.3	Jets	81
8.4	Photons	81
9	EVENT SELECTION	83
9.1	Trigger Strategy	84
9.2	Signal Efficiency and Contamination	86
10	BACKGROUND ESTIMATION	89
10.1	Flavor Symmetric Processes	89
10.1.1	Flavor Symmetry Method	89
10.1.2	Sideband Fit Method	91
10.2	Z/ γ^* + jets Background	92
10.2.1	Photon and Z Event Selection	96
10.2.2	Smearing of Photon Events	96
10.2.3	p_T Reweighting of Photon Events	98
10.2.4	Determining the $m_{\ell\ell}$ Shape	100
10.2.5	Subtraction of V γ Events	102
10.2.6	Validation in Data	102
10.3	Fake and Non-Prompt Leptons	103
10.4	Diboson and Rare Top Processes	107
11	SYSTEMATIC UNCERTAINTIES	113
11.1	Uncertainties on Data-Driven Backgrounds	113
11.1.1	Uncertainties on the Flavor Symmetry Method .	113
11.1.2	Uncertainties on the γ + jets Method	117
11.1.3	Uncertainties on the Fakes Background	120
11.2	Theoretical and Experimental Uncertainties	122
11.3	Impact of Uncertainties on the Signal Region	123
12	RESULTS	127
13	INTERPRETATIONS	129
V	CONCLUSIONS	131
14	CONCLUSIONS	133
15	OUTLOOK	135
	BIBLIOGRAPHY	137

LIST OF FIGURES

Figure 1	The Standard Model of particle physics, containing all known bosons and fermions, with the addition of the hypothetical graviton. [55]	8
Figure 2	Gluon self coupling Feynman diagrams involving 3- and 4-gluon interactions.	12
Figure 3	Quark couplings to the different types of gauge bosons. The $q_{u,d}$ labels represent any up- or down-type quarks.	13
Figure 4	The running of the strong coupling constant, α_s . [70]	13
Figure 5	Trilinear gauge couplings in the Standard Model (SM).	15
Figure 6	Weak couplings to leptons in the SM.	15
Figure 7	Higgs couplings to the weak gauge bosons in the SM.	17
Figure 8	Higgs couplings to fermions in the SM.	18
Figure 9	2008 MSTW Parton Distribution Functions (PDFs) for various particle types given as a function of x and Q^2 , the square of the parton-parton momentum transfer. [68]	18
Figure 10	Galactic rotation curve showing that the discrepancy between the observed luminous matter and the total mass in the system can be described as a non-luminous halo of matter. [79]	19
Figure 11	Two example vertices allowed by the Minimal Supersymmetric Standard Model (MSSM).	22
Figure 12	Running of the strong, weak, and electromagnetic coupling constants for the SM (left) and MSSM (right). [1]	23
Figure 13	Feynman diagram of the decay considered in the simplified models used in the analysis presented in Part iv.	25
Figure 14	Number of secondary vertices in a module in the first layer of the pixel detector in data (top) and Monte Carlo simulation (MC) (bottom). There are more events in the data than the MC [25].	27
Figure 15	The Large Hadron Collider (LHC) main collider ring and pre-accelerator Super Proton Synchrotron (SPS) overlaid on a map of Switzerland and France, with the four main LHC experiments identified.	31

Figure 16	The pre-accelerators of the LHC	32
Figure 17	Bunch structure in the Proton Synchrotron (PS), SPS, and LHC	33
Figure 18	Cross-section of a cryodipole magnet in the LHC .	34
Figure 19	Beam spot in the ATLAS detector for one run in 2015. Distributions show only the highest p_T vertex per event. Left is the $x - y$ distribution of vertices, while the right plot shows the $x - z$ distribution.	34
Figure 20	Cross-sections for many SM processes at the Tevatron and LHC [2].	35
Figure 21	Instantaneous luminosity of one fill of 7 TeV data in 2011.	36
Figure 22	ATLAS luminosity for Run 1 and Run 2, as of September 2016.	37
Figure 23	Average number of interactions per crossing shown for 2015 and 2016 separately, as well as the sum of the two years.	37
Figure 24	Diagram of the ATLAS detector, with subsys- tems and magnets identified.	39
Figure 25	Diagram of the ATLAS Inner Detector, contain- ing the Pixel, SCT, and TRT subsystems.	41
Figure 26	Diagram of one-quarter of the ATLAS Inner Detector in the $R - z$ plane, with lines drawn to indicate various η locations.	42
Figure 27	The calorimeter system of the ATLAS detector. An $x-y$ view of the Muon Spectrometer (MS). In it, the three barrel layers are visible, as well as the overlapping, differently sized chambers. The outer layer of the MS is about 20m in di- ameter.	43
Figure 28	45	
Figure 29	An $r-z$ view of the MS. The three layers of the barrel and endcap MS are visible, and all muons at $ \eta < 2.7$ should traverse three detectors, as- suming they propagate in an approximately straight line from the interaction point.	46
Figure 30	The magnet system of the ATLAS detector. The inner cylinder shows the solenoid which gives a uniform magnetic field in the Inner Detector (ID). Outside of that are the barrel and endcap toroids, which provide a non-uniform magnetic field for the MS.	47

Figure 31	Plots of the magnetic field within the ATLAS detector. Top is the field (broken into its R and z components) as a function of z for several different values of R . Bottom is the field integral through the Monitored Drift Tubes (MDTs) as a function of $ \eta $ for two different ϕ values.	49
Figure 32	Level One (L1) trigger rates for for a run in July 2016 as a function of luminosity block, an approximately 60-second long period of data-taking. The total rate is lower than the combined stack because of overlapping triggers.	50
Figure 33	High Level Trigger (HLT) trigger rates for for a run in July 2016 as a function of luminosity block, an approximately 60-second long period of data-taking. The total rate is lower than the combined stack because of overlapping triggers.	51
Figure 34	Trigger efficiencies as a function of E_T for data and MC . Efficiencies are given for offline selected loose electrons.	51
Figure 35	Identification efficiencies from MC samples for loose, medium, and tight working points. Left is the efficiency for identification of true electrons taken from $Z \rightarrow ee$ MC , and right is the efficiency for mis-identification of jets as electrons taken from dijet MC [51].	54
Figure 36	Combined electron reconstruction and identification efficiencies measured as a function of η for data (using the tag-and-probe method on $Z \rightarrow ee$ events) and $Z \rightarrow ee$ MC . Distributions include all electrons with $E_T > 15$ GeV. [51].	55
Figure 37	Comparison of tight identification efficiency measurements from data and $Z \rightarrow \ell\ell\gamma$ MC for unconverted (left) and converted (right) photons, with an inclusive η selection. The bottom of each figure shows the ratio of data and MC efficiencies. [73].	57
Figure 38	Muon reconstruction efficiency for the Medium working point measured with $Z \rightarrow \mu\mu$ events in data using the tag-and-probe method and in MC as a function of η . The ratio between the two is shown at the bottom. [43]	59
Figure 39	Muon reconstruction efficiency for the High- p_T working point measured with $Z \rightarrow \mu\mu$ events in data using the tag-and-probe method and in MC as a function of η . The ratio between the two is shown at the bottom. [43]	60

Figure 40	Distribution of event p_T density, ρ , taken from MC dijets for different numbers of primary vertices. [13]	61
Figure 41	Energy response as a function of energy and η for Electromagnetic (EM) jets in dijet MC. [13] . .	62
Figure 42	Dijet MC distributions of the number of pile-up jets passing the Jet Vertex Tagger (JVT) and Jet Vertex Fraction (JVF) cuts (left) and the efficiency for jets from the primary vertex (right) as a function of number of primary vertices in the event [10].	62
Figure 43	A few possible types of clusters in the Pixel Detector. (a) shows a single particle passing through a layer of the detector, (b) shows two particles passing through the detector, creating a single merged cluster, and (b) shows a single particle emitting a δ -ray as it passes through the detector.	65
Figure 44	One example of a two-particle cluster and its truth information compared with the output of the Neural Networks (NNs). The boxes represent pixels, with a color scale indicating Time Over Threshold (ToT). At top, the $p(N = i)$ values give the output of the Number NN, the probabilities that the cluster contains 1, 2, and 3 particles. Given the highest probability is for $N = 2$, the other NNs predict the position and errors of the two particles (in white). The black arrows and squares represent the truth information from the cluster, and the black dot and dotted line show the position measurement for the un-split cluster.	68
Figure 45	x resolutions for clusters with 3 (top) and 4 (bottom) pixels in the x direction in 7 TeV data for Connected Component Analysis (CCA) and NN clustering taken from MC.	69
Figure 46	Fraction of cluster classes as a function of the distance between tracks for IBL (top) and 2nd pixel layer (bottom).	70

Figure 47	Performance of the pixel neural network used to identify clusters created by multiple charged particles, as a function of constant coherent scaling of the charge in each pixel in the cluster. The top figure shows the rate at which the neural network wrongly identifies clusters with one generated particle as clusters with multiple particles. The bottom figure shows the rate at which the neural network correctly identifies clusters generated by multiple particles as such.	71
Figure 48	An example Feynman diagram of $t\bar{t}$ production and decay.	75
Figure 49	An example Feynman diagram of the production and decay of a WZ event.	76
Figure 50	An example Feynman diagram of the production and decay of a $Z/\gamma^* + \text{jets}$ event.	76
Figure 51	Schematic diagrams of the control, validation and signal regions for the on-shell Z (top) and edge (bottom) searches. For the on-shell Z search the various regions are shown in the $m_{\ell\ell} - E_T^{\text{miss}}$ plane, whereas in the case of the edge search the signal and validation regions are depicted in the $H_T - E_T^{\text{miss}}$ plane.	84
Figure 52	Signal region acceptance (left) and efficiency (right) in SRZ for the simplified model with gluino pair production with $\tilde{\chi}_2^0$ decays to $\tilde{\chi}_1^0$ and an on-shell Z boson with 1GeV neutralino LSP. Acceptance is calculated by applying the signal-region kinematic requirements to truth objects in MC, which do not suffer from identification inefficiencies or measurement resolutions.	86
Figure 53	Expected signal contamination in CRT (left) and CR-FS (right) for the signal model with gluino pair production, where the gluinos decay to quarks and a neutralino, with the neutralino subsequently decaying to a Z boson and a 1GeV neutralino LSP.	87
Figure 54	Expected signal contamination in VRS (left) and VRT (right) for the signal model with gluino pair production, where the gluinos decay to quarks and a neutralino, with the neutralino subsequently decaying to a Z boson and a 1GeV neutralino LSP.	87
Figure 55	Comparison of data and MC in a selection like SRZ, without the E_T^{miss} cut.	92

Figure 56	MC comparison of boson p_{T} in a selection of photon and $Z \rightarrow \ell\ell$ events with $H_{\text{T}} > 600$ GeV.	95
Figure 57	$E_{T,\parallel}^{\text{miss}}$ distributions in MC for $Z + \text{jets}$ and $\gamma + \text{jets}$ in an inclusive region with $H_{\text{T}} > 600$ GeV.	97
Figure 58	$E_{T,\parallel}^{\text{miss}}$ distributions in MC for $Z + \text{jets}$ and $\gamma + \text{jets}$ in an inclusive region with $H_{\text{T}} > 600$ GeV after the smearing procedure has been performed. These distributions have also been p_{T} reweighted, as described in Section 10.2.3.	98
Figure 59	Photon reweighting factors for the ee (left) and $\mu\mu$ (right) channels derived from data and MC	99
Figure 60	$E_{\text{T}}^{\text{miss}}$ distribution comparing MC distributions of photon and Z events before any smearing is applied (top), with only p_{T} reweighting applied (bottom left), and after p_{T} reweighting and smearing have both been applied (bottom right) in the ee channel of 2016 data.	100
Figure 61	$E_{\text{T}}^{\text{miss}}$ distribution comparing MC distributions of photon and Z events before any smearing is applied (top), with only p_{T} reweighting applied (bottom left), and after p_{T} reweighting and smearing have both been applied (bottom right) in the $\mu\mu$ channel of 2016 data.	101
Figure 62	$Z/\gamma^* + \text{jets}$ MC $m_{\ell\ell}$ distribution compared to the prediction from $\gamma + \text{jets}$ method performed on MC (left) and the prediction from $\gamma + \text{jets}$ method performed on data (right).	102
Figure 63	Comparison of data and MC in CR- γ without any H_{T} cut, including the contributions from various $V\gamma$ processes.	103
Figure 64	Total $\gamma + \text{jets}$ data prediction in SRZ (excluding the $E_{\text{T}}^{\text{miss}}$ cut) and the prediction after the $V\gamma$ subtraction.	104
Figure 65	$E_{\text{T}}^{\text{miss}}$ distribution in VRZ ee (left) and $\mu\mu$ (right) with total data yield compared to the sum of the prediction from the $\gamma + \text{jets}$ method, the prediction from the flavor symmetry method, the prediction from the fake background estimation (included under “other”), and the remaining backgrounds taken from MC	105

Figure 66	$\Delta\phi(\text{jet}, \mathbf{p}_T^{\text{miss}})$ distribution in for the leading jet (left) and the subleading jet (right). The comparison is performed in VRZ with the cut on $\Delta\phi(\text{jet}_{12}, \mathbf{p}_T^{\text{miss}})$ removed. The total data yield is compared to the sum of the prediction from the $\gamma + \text{jets}$ method, the prediction from the flavor symmetry method, the prediction from the fake background estimation (included under “other”), and the remaining backgrounds taken from MC.	105
Figure 67	Sub-leading lepton p_T for ee (left) and $\mu\mu$ (right) events in the tight-tight region used to measure the real-lepton efficiency for 2016.	106
Figure 68	Sub-leading lepton p_T for μe (left) and $\mu\mu$ (right) events in the tight-tight region used to measure the fake-lepton efficiency for 2016.	107
Figure 69	Same sign validation regions in the ee (top left), $\mu\mu$ (top right), $e\mu$ (bottom left) and μe (bottom right) channels combining 2015+2016 data. Uncertainty bands include both statistical and systematic uncertainties.	108
Figure 70	Distribtuions of data and MC in VR-WZ. Reconstructed transverse mass of the W (top) and mass of the Z (bottom).	109
Figure 71	Distribtuions of data and MC in VR-WZ. p_T of the W (top) and Z (bottom).	110
Figure 72	Distribtuions in VR-WZ. On the top, mass of the Z bosons in the event, and on the bottom, p_T of the Z bosons.	111
Figure 73	MC closure plots of VRS (top) and SRZ (bottom). The number of events from MC (black points) is compared to the number of events predicted from the flavor symmetry method (yellow histogram). The comparison is performed before the expanded $m_{\ell\ell}$ window is used to predict the on- Z bin, but because the shape is taken from the same MC, the result is identical.	114
Figure 74	Measurements of k , the ratio of electron to muon events, in bins of p_T and η . On the top is the measurements indexed by the leading lepton, while the measurements indexed by the sub-leading lepton are on the bottom. These efficiencies are for the 2016 dataset.	115

Figure 75	α , the trigger efficiency ratio, calculated as a function of E_T^{miss} from three different sources: data (blue), the usual skimmed $t\bar{t}$ MC (red), and an unskimmed $t\bar{t}$ MC (green).	117
Figure 76	Plots of the fraction of on-Z events with a VR-FS-like selection as a function of H_T . The top figure shows 2015 data and MC while the bottom figure shows the same for 2016.	118
Figure 77	E_T^{miss} distributions for $\gamma + \text{jets}$ predictions using different reweighting variables, as well as distributions with the nominal reweighting but with smearing functions taken from data and from MC in a ≥ 2 -jet region.	119
Figure 78	MC closure of the $\gamma + \text{jets}$ method as a function of E_T^{miss} comparing the MC prediction of the Z background with the $\gamma + \text{jets}$ method performed on $\gamma + \text{jets}$ MC. The uncertainty band includes both statistical and reweighting uncertainties.	120
Figure 79	Distributions of $m_T(\ell, E_T^{\text{miss}})$, the transverse mass of the lepton and the E_T^{miss} in a Validation Region (VR) designed to target $W\gamma$ processes. Top is the distribution with a E_T^{miss} cut at 100 GeV, and bottom is the same distribution with a E_T^{miss} cut of 200 GeV.	121

LIST OF TABLES

Table 1	Supermultiplets of the MSSM . Sfermions, on the first five rows, are all spin-0. Higgsinos and gauginos are all spin-1/2. Three sets of each fermion's supermultiplet exist, one for each generation. [69]	21
Table 2	Simulated background event samples used in this analysis with the corresponding matrix element and parton shower generators, cross-section order in α_s used to normalise the event yield, underlying-event tune and PDF set.	78
Table 3	Summary of the electron selection criteria. The signal selection requirements are applied on top of the baseline selection.	79
Table 4	Summary of the muon selection criteria. The signal selection requirements are applied on top of the baseline selection.	80
Table 5	Summary of the jet and b -jet selection criteria. The signal selection requirements are applied on top of the baseline requirements.	81
Table 6	Summary of the photon selection criteria.	82
Table 7	Overview of all signal, control and validation regions used in the on-shell Z search. More details are given in the text. The flavour combination of the dilepton pair is denoted as either "SF" for same-flavour or "DF" for different flavour. All regions require at least two leptons, unless otherwise indicated. In the case of CR γ , VR-WZ, VR-ZZ, and VR-3L the number of leptons, rather than a specific flavour configuration, is indicated. The main requirements that distinguish the control and validation regions from the signal region are indicated in bold. Most of the kinematic quantities used to define these regions are discussed in the text. The quantity $m_T(\ell_3, E_T^{\text{miss}})$ indicates the transverse mass formed by the E_T^{miss} and the lepton which is not assigned to either of the Z-decay leptons.	85
Table 8	Lepton trigger requirements used for the analysis in different regions of lepton- p_T phase space.	86

Table 9	Yields in signal and validation regions for the flavor symmetric background. Errors include statistical uncertainty, uncertainty from MC closure, uncertainty from the k and α factors, uncertainty due to deriving triggers efficiencies from a DAOD, and uncertainty on the MC shape used to correct for the $m_{\ell\ell}$ expansion.	91
Table 10	Background fit results from the sideband fit method. The $t\bar{t}$ MC's normalization is taken as a free parameter in the fit to data in CRT, then that normalization factor is applied in SRZ. The results are shown here both divided between the ee and $\mu\mu$ channels and summed together. All other backgrounds are taken from MC in CRT, while in SRZ, the Z/γ^* + jets contribution is taken from the γ + jets method. The uncertainties quoted include both statistical and systematic components.	93
Table 11	Summary of the $t\bar{t}$ normalization factors calculated by the sideband fit to CRT and VRT for the 2015+2016 data.	94
Table 12	Comparison of Flavor Symmetric (FS) background predictions from the nominal method, the flavor symmetry method, and the cross-check, the sideband fit method. Uncertainties include statistical and systematic uncertainties in both cases.	94
Table 13	List of triggers used to collect photon events in 2015 and 2016 data-taking.	97
Table 14	Control regions used to measure efficiencies of real and fake leptons. The flavour combination of the dilepton pair is denoted as either "SF" for same-flavour or "DF" for different flavour. The charge combination of the leading lepton pairs are given as "SS" for same-sign or "OS" for opposite-sign.	106
Table 15	Yields in validation regions. In VRS, data-driven background estimates are used for Z/γ^* + jets, fakes, and FS processes. All other backgrounds are taken from MC, including all backgrounds in the multi-lepton VRs. Uncertainties include statistical and systematic components.	108

Table 16	Uncertainties in the on-Z signal and validation regions. Nominal predictions are given with statistical uncertainty (including uncertainty from subtracted backgrounds), MC Closure uncertainty, uncertainty on the prediction from varying k and α by their statistical uncertainties, comparing the efficiencies from AODs to that of DAODs, and on the $m_{\ell\ell}$ widening, which includes MC statistics and a data/MC comparison in a loosened region.	113
Table 17	Uncertainty breakdown for the $\gamma + \text{jets}$ method in SRZ. Uncertainties considered are the impact of MC uncertainty on $V\gamma$ backgrounds, MC closure, uncertainty on $m_{\ell\ell}$ shape (also determined via MC closure), reweighting uncertainties, smearing uncertainties, and statistical uncertainty on the $\gamma + \text{jets}$ events used in the method.	122
Table 18	Systematic uncertainties on the fake-lepton background for on-Z regions for 2015+2016 yields. The nominal yield includes statistical uncertainty from the baseline selection in a given region. The following rows indicate the results of varying the real and fake lepton efficiencies up and down by their statistical uncertainty. Real cont. gives an uncertainty on the contamination of real leptons in the fake lepton efficiency. b -jet and no b -jet indicate the impact of requiring or vetoing b -tagged jets in the regions used to measure the fake efficiency.	122
Table 19	Fractional uncertainties of dibosons in signal and validation regions from Sherpa scale variations.	124
Table 20	Comparison of yields in on-Z and off-Z regions in Sherpa and Powheg diboson MC at 14.7 fb^{-1}	124
Table 21	Overview of the dominant sources of systematic uncertainty on the total background estimate in the signal regions. The values shown are relative to the total background estimate, shown in %.	125

LISTINGS

ACRONYMS

- IBL Insertable B-Layer
MS Muon Spectrometer
ID Inner Detector
SCT Silicon Microstrip Tracker
TRT Transition Radiation Tracker
NN Neural Network
CCA Connected Component Analysis
ToT Time Over Threshold
MDT Monitored Drift Tube
CSC Cathode-Strip Chamber
RPC Resistive Plate Chamber
TGC Thin Gap Chamber
L1 Level One
HLT High Level Trigger
L1Calo L1 Calorimeter Trigger
L1Topo L1 Topological Trigger
CTP Central Trigger Processor
TTC Trigger Timing and Control
ROB Read Out Board
RoI Region of Interest
LHC Large Hadron Collider
LEP Large Electron-Positron
SPS Super Proton Synchrotron
CMS Compact Muon Solenoid
ALICE A Large Ion Collider Experiment
LHCb Large Hadron Collider beauty

RF	Radiofrequency
PSB	Proton Synchrotron Booster
PS	Proton Synchrotron
OR	Overlap Removal
EM	Electromagnetic
LCW	Local Cluster Weighting
JES	Jet Energy Scale
JER	Jet Energy Resolution
JVT	Jet Vertex Tagger
JVF	Jet Vertex Fraction
MC	Monte Carlo simulation
SM	Standard Model
BSM	Beyond the Standard Model
SUSY	Supersymmetry
QCD	Quantum Chromodynamics
PDF	Parton Distribution Function
DM	Dark Matter
LO	Leading Order
NLO	Next to Leading Order
NLO+NLL	Next-to-Leading-Logarithmic Accuracy
SUSY	Supersymmetry
MSSM	Minimal Supersymmetric Standard Model
LSP	Lightest Supersymmetric Particle
AOD	Analysis Object Data
dAOD	derived AOD
SR	Signal Region
VR	Validation Region
CR	Control Region
FS	Flavor Symmetric

Part I

INTRODUCTION

The centerpiece of this thesis is a search for supersymmetric particles, but it also includes all the scaffolding and background necessary to understand the search. An overview of the [LHC](#) and the ATLAS Detector are presented along with the theory that motivates the search.

INTRODUCTION

The pages that follow detail the author’s work on the ATLAS experiment from 2011 through 2016, focusing on an analysis of 13TeV proton-proton collisions at the [LHC](#) looking for Supersymmetry with the ATLAS Detector.

[CHAPTER 2](#) outlines the Standard Model of Particle Physics and the benefits of extending it to include Supersymmetry, then continues to describe the motivation behind searching for this particular model.

[CHAPTER 3](#) describes the [LHC](#) and its operation.

[CHAPTER 4](#) contains descriptions of the many pieces of the ATLAS detector, and how they serve to detect particles coming from [LHC](#) collisions.

[CHAPTER 5](#) presents a neural network designed to improve tracking in the ATLAS Pixel Detector, and describes the benefits of its implementation.

Part II

THEORY AND MOTIVATION

This section describes the theoretical foundation for the analysis presented in [Part iv](#). It includes an overview of the Standard Model, including its phenomenology in a $p - p$ collider. The theory of Supersymmetry is explained, and the motivation for extending the Standard Model to include it is presented. In addition, this section includes an explanation of Monte Carlo generators and details about the specific form of Supersymmetry searched for in this analysis.

2

THEORY AND MOTIVATION

The Standard Model ([SM](#)) of particle physics represents all particles and interactions currently understood by the particle physics community. It is formulated using the principles of Quantum Field Theory, with the constraints of several symmetries and physical requirements to determine the rules for allowed interactions. [33] Developed in the 1960s and 70s, it has been immensely successful at predicting the existence of particles before their discovery, and has held up to many high-precision tests. Despite this success, it has several shortcomings which point to its incompleteness. Though the [SM](#) is likely correct at the energies thus far probed, it may be missing key components that become more important at higher energies. Models supplementing the [SM](#) with additional particles and interactions are referred to as Beyond the Standard Model ([BSM](#)) theories.

One possible extension of the [SM](#) is Supersymmetry ([SUSY](#)), a theory which postulates an additional symmetry between bosons and fermions to the [SM](#), creating a spectrum of [SUSY](#) particles (sparticles) which interact with the particles of the [SM](#). This theory motivates the search performed in [Part iv](#), and its theoretical appeals are discussed in this section, along with specific simplified models considered in the search.

2.1 THE STANDARD MODEL

The [SM](#) of particle physics describes the interactions of all of the particles currently known to exist, and consists of both matter particles and force carriers. This model has been unprecedentedly successful in predicting new particles and phenomena, including the prediction of the Higgs particle almost 50 years before its discovery in 2012, which completed the [SM](#). This section describes the components of the [SM](#) and how they interact, focusing on the environment of the [LHC](#).

The particles of the [SM](#) are divided into two categories: fermions and bosons. The fermions comprise all the matter described by the [SM](#), and are spin- $\frac{1}{2}$ particles. The bosons, integer-spin particles, are the force carriers. They provide a mechanism to explain three of the four forces known to particle physics, with gravity still lacking a quantum formulation. The Higgs boson, the only spin-0 particle in the [SM](#), provides a mechanism for giving mass to the other particles. The full [SM](#), with the addition of the hypothetical graviton, is presented in [Figure 1](#).

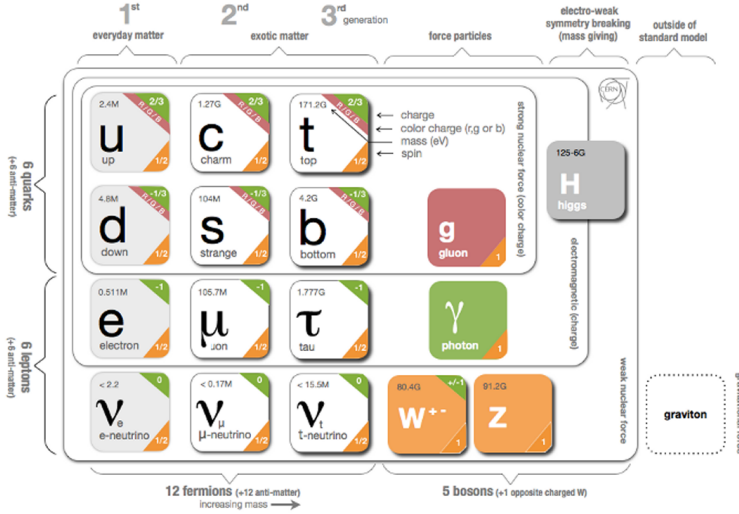


Figure 1: The Standard Model of particle physics, containing all known bosons and fermions, with the addition of the hypothetical graviton. [55]

2.1.1 Matter

The matter described by the SM is made up of fermions, spin- $\frac{1}{2}$ particles which can be broken into two groups, quarks and leptons. The leptons all interact weakly, while the quarks additionally interact strongly.

2.1.1.1 Leptons

Leptons, as seen in the bottom left of Figure 1, come in three generations, each labeled by a flavor: electron, muon, and tau. In the case of the massive leptons, these flavors are mass eigenstates, and the generations are placed in an order based on increasing mass. Each massive lepton is negatively electromagnetically charged and has a positively charged anti-particle.

The three neutrinos come in the same flavors as the massive leptons, but these flavor eigenstates do not correspond exactly to mass eigenstates. As a consequence, neutrinos oscillate between flavors as they propagate through space. These oscillations are the only evidence of neutrino mass, which is bound from below by the mass splittings determined from the oscillation and bound from above by cosmological limits on the universe's mass density [60]. Though it is still uncertain if the masses of the neutrinos follow the same hierarchy as the massive leptons, that expected ordering is slightly preferred over the inverted hierarchy [59].

Unlike the massive leptons, the neutrinos are uncharged, and it is not yet known whether each neutrino has a separate anti-particle, or if it is its own antiparticle. Because they are not electromagnetically

charged, they can only interact weakly, making them extremely difficult to detect. In the ATLAS detector, neutrinos pass through all layers undetected, and their presence can only be inferred from the non-conservation of momentum that results in the observed particles. As a consequence of their ability to evade detection, neutrinos are the least understood particles of the SM.

The SM conserves lepton number, L , which is defined as the number of leptons minus the number of anti-leptons in a state, and can also be defined for each lepton flavor. Though there are anomalies that appear in second order SM interactions which could provide very small violations of this conservation, it holds to great precision in experiment. $\mu \rightarrow e\gamma$ branching ratios, for example, have been constrained to 10^{-13} [47]. As a consequence of this conservation, the lightest massive lepton, the electron, is stable.

2.1.1.2 Quarks

Quarks, as seen in the top left of Figure 1, are also electromagnetically charged particles that interact weakly, but are differentiated from the leptons by their strong interactions. They are also organized in three generations ordered by mass, and come in pairs of *up*-type and *down*-type quarks, named after the lightest generation. Though the up quark is lighter than the down, that rule is reversed in the subsequent two generations. Up-type quarks are electromagnetically charged $+\frac{2}{3}$, while the down-type quarks are charged $-\frac{1}{3}$. Quarks are also charged under the strong interaction, whose three charges are often characterized by colors: red, green, and blue. Each quark has an anti-particle with the opposite charges.

These fractional charges and individual colors are never seen in nature because of the requirement (discussed further in Section 2.1.2.2) that stable particle states be color-neutral. To accomplish this, quarks can create two-particle bound states called *mesons* consisting of one quark and one anti-quark with the same color charge or three-particle bound states of quarks or anti-quarks with the three different color charges, which are called *baryons*. The lightest color neutral state containing only quarks, the proton (uud), is stable. Extremely unstable bound states consisting of higher numbers of quarks can also exist, such as the pentaquark discovered in 2015 at the LHC. [78] Collectively, these multi-quark bound states are called *hadrons*.

Like leptons, the number of quarks in a state is conserved, up to very small anomalies. However, because quarks cannot exist in an isolated state, that conservation is described in terms of baryon number (B) defined similarly to lepton number. Mesons, because they have one quark and one anti-quark, have $B = 0$.

2.1.2 Forces

The fermions in the previous section interact via the electromagnetic, weak, and strong forces. In a perturbative quantum field theory, interactions via these forces are represented by mediating bosons. These force carriers interact only with particles charged with their force's quantum numbers. The photon, for example, interacts only with electromagnetically charged particles. Gluons, mediators of the strong force, interact only with color charged particles, quarks and gluons. All fermions are weakly charged and interact with the weak force's mediators, the W and Z bosons.

The formulation for each of these forces is developed by requiring that the [SM](#) lagrangian be locally gauge invariant. [58] This can be accomplished by adding gauge fields to the lagrangian, whose behavior under gauge transformations cancels out the gauge dependence of the free lagrangian. However, adding a mass term for these fields reintroduces gauge dependence, so this mechanism only creates forces mediated by massless gauge bosons. The addition of the Higgs field provides mass terms for the weak gauge bosons (as well as other particles) without interfering with the gauge invariance.

The total gauged symmetry group for the [SM](#) is $SU_C(3) \times SU_L(2) \times U_Y(1)$, where C stands for color, the charge of the strong force, L stands for left, because the weak force is left-handed, and Y is the hypercharge quantum number, the charge of the unified electroweak force.

2.1.2.1 The Electromagnetic Force

Electromagnetism provides the simplest example of a requirement of local gauge invariance generating a lagrangian description of a force. Electromagnetism has one massless mediator, the photon, which interacts with all electromagnetically charged particles. What follows is a brief description of how enforcing this invariance generates a lagrangian of the same form as the classical electromagnetic lagrangian, which can be easily incorporated into the [SM](#).

The particles in [Section 2.1.1](#) are fermions, and so the lagrangian describing their free propagation are Dirac lagrangians and all follow the form

$$\mathcal{L} = i\bar{\psi}\gamma^\mu\partial_\mu\psi - m\bar{\psi}\psi. \quad (1)$$

Requiring that the free lagrangians for these particles be invariant under a $U(1)$ local gauge transformation, $e^{iq\lambda(x)}$, can be accomplished by adding a term to the lagrangian which cancels the derivative term arising from λ 's dependence on x :

$$\mathcal{L} = i\bar{\psi}\gamma^\mu\partial_\mu\psi - m\bar{\psi}\psi - (q\bar{\psi}\gamma^\mu\psi)A_\mu \quad (2)$$

where A_μ is a “gauge field” that transforms according to

$$A_\mu \rightarrow A_\mu + \partial_\mu \lambda. \quad (3)$$

This vector field must also come with a free term,

$$\mathcal{L} = -\frac{1}{16\pi} F^{\mu\nu} F_{\mu\nu} + \frac{1}{8\pi} m_A^2 A^\nu A_\nu. \quad (4)$$

The mass term for this field would not itself be invariant under the transformation, but the field can simply be made massless to avoid this problem. The final lagrangian, then, is

$$\mathcal{L} = i\bar{\psi}\gamma^\mu \partial_\mu \psi - m\bar{\psi}\psi - \frac{1}{16\pi} F^{\mu\nu} F_{\mu\nu} - (q\bar{\psi}\gamma^\mu \psi) A_\mu \quad (5)$$

which is precisely the original lagrangian with the addition of terms replicating the form of the Maxwell lagrangian. In a quantized interpretation, it describes a field that interacts with particles with non-zero electromagnetic charge q via interactions with a massless spin-1 boson, the photon.

For the purpose of succinct notation, this lagrangian is often rewritten in terms of the “covariant derivative”

$$D_\mu = \partial_\mu + iq\lambda A_\mu \quad (6)$$

which immediately cancels the gauge dependent term created by the transformation. This mechanism is mathematically simple in the $U(1)$ case, but can be replicated for more complicated gauge transformations with perturbative approximations.

2.1.2.2 The Strong Force

The strong force is generated by a similar process of requiring local gauge invariance, but in this case, for a $SU(3)$ transformation. The interactions of the strong force are described by the theory of quantum chromodynamics, which is given by the lagrangian

$$\mathcal{L}_{strong} = -\frac{1}{4} G_{\mu\nu}^\alpha G^{\alpha\mu\nu} - \frac{1}{2} \bar{Q}_m D Q_m \quad (7)$$

where the α index runs from 1 to 8 and represents the different generators of $SU(3)$, and m indexes the three quark generations. $G_{\mu\nu}^\alpha$ is the field strength tensor and is defined as

$$G_{\mu\nu}^\alpha = \partial_\mu G_\nu^\alpha - \partial_\nu G_\mu^\alpha + g_3 f_{\beta\gamma}^\alpha G_\mu^\beta G_\nu^\gamma \quad (8)$$

where g_3 is a function of the energy scale of the interaction μ , and is related to the strong coupling constant by

$$\alpha_s(\mu) = g_s(\mu)^2 / 4\pi. \quad (9)$$

This first term of the lagrangian gives the gluon self-coupling interactions, with terms involving 2, 3, and 4 gluon field terms. The 2-field portion is simply the field strength tensor, but the other terms give couplings that can be described by the feynman diagrams in [Figure 2](#).

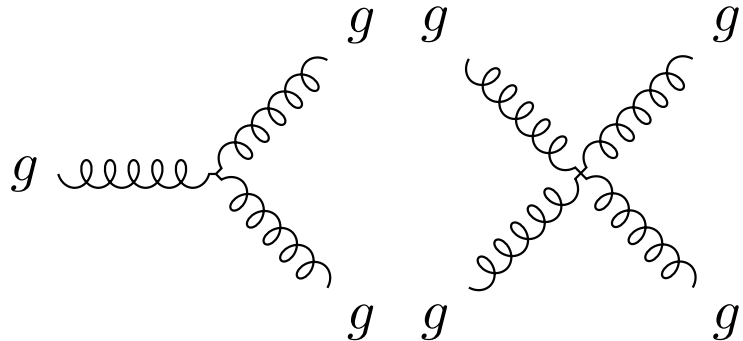


[Figure 2](#): Gluon self coupling Feynman diagrams involving 3- and 4-gluon interactions.

In the second term, DQ_m is the covariant derivative acting on the quark field. The quarks are in fact charged under all three forces, strong, electromagnetic, and weak, so the covariant derivative includes terms to make each of the force's lagrangians gauge invariant. Thus this term introduces quark-boson interactions of four types, seen in [Figure 3](#). The quarks' coupling to the gluon is the strongest, with the other couplings happening at lower rates. The couplings to the W and Z bosons are described in [Section 2.1.2.3](#).

The canceling required to make the lagrangian gauge invariant is only satisfied to a first order expansion of the transformation, guaranteeing its validity only for infinitesimally small perturbations from the ground state. However, the strong coupling constant, α , depends on the energy scale of the interaction, decreasing at higher energy scales and asymptotically increasing at low energies. [Figure 4](#) shows this effect translated to distance scales, demonstrating that QCD is weak and can be considered perturbatively at small distance scales, but at large distance scales this approximation breaks down, and the colorless hadrons introduce in [Section 2.1.1.2](#) must be used to describe interactions instead.

The boundary between these regimes is referred to as Λ_{QCD} and differentiates energies at which quarks can be considered free particles and the energies at which they must instead be described by their colorless bound states. The [LHC](#) is capable of producing individ-

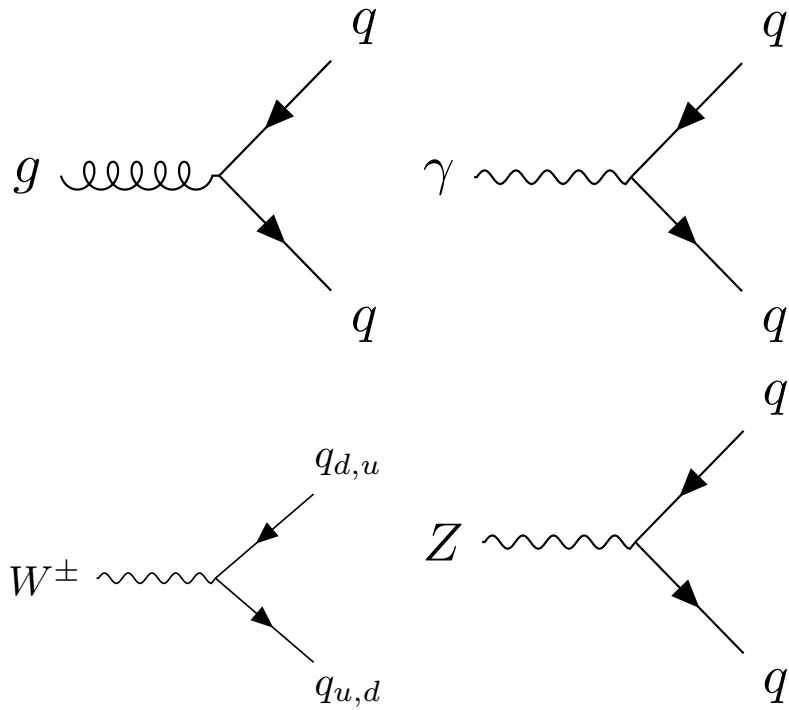


Figure 3: Quark couplings to the different types of gauge bosons. The $q_{u,d}$ labels represent any up- or down-type quarks.

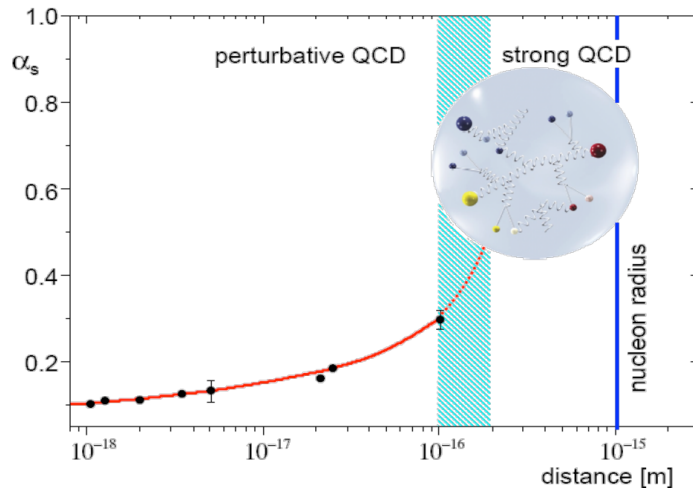


Figure 4: The running of the strong coupling constant, α_s . [70]

ual quarks, but they instantaneously hadronize, producing showers of particles referred to as *jets*.

2.1.2.3 The Electroweak Force

A similar process, using an $SU(2)$ gauge transformation, can produce a lagrangian that would suffice to describe the W and Z bosons of the **SM**, if only they were massless. However, they are not, so an alternate mechanism must be used to add masses to the lagrangian.

Before a mechanism for their masses was understood, and before they were discovered, the large masses of the W and Z bosons were proposed in order to unify the electromagnetic and weak forces into the electroweak force. The large masses were crucial to explain the discrepancy in the strength of the two forces.

This unified theory resulted in a triplet, \mathbf{W} , with coupling g_W , and a singlet field B , with coupling $g'/2$. However, this electroweak symmetry is broken, and mixing between these states occurs. Rewritten in their mass basis, the more familiar electroweak force carriers are produced: W^\pm , two states with identical coupling resulting from the first two states of the \mathbf{W} triplet, then Z^0 and the photon field A resulting from the mixing of the last \mathbf{W} state and B .

The electroweak lagrangian is much more complicated than the strong lagrangian, and can be divided into several terms:

$$\mathcal{L}_{\text{electroweak}} = \mathcal{L}_{\text{gauge}} + \mathcal{L}_{\text{fermions}} + \mathcal{L}_{\text{Higgs}} + \mathcal{L}_{\text{Yukawa}}. \quad (10)$$

The first term can be written as follows

$$\mathcal{L}_{\text{gauge}} = -\frac{1}{4} W^{a\mu\nu} W_{\mu\nu}^a - \frac{1}{4} B^{\mu\nu} B_{\mu\nu} \quad (11)$$

where the a indices are numbered 1 through 3 and indicate the generators of $SU(2)$ which are written

$$W_{\mu\nu}^a = \partial_\mu W_\nu^a - \partial_\nu W_\mu^a + g_2 \epsilon_{abc} W_\mu^b W_\nu^c \quad (12)$$

The gauge portion of the lagrangian then generates interaction terms of between the gauge fields, which when rewritten in terms of the mass-eigenstate basis, generates interactions between three gauge bosons, like the ones in [Figure 5](#), as well as interactions between four gauge bosons.

The fermion portion of the lagrangian is written as

$$\begin{aligned} \mathcal{L}_{\text{fermion}} = & -\frac{1}{2} \bar{L}_m \not{D} L_m - \frac{1}{2} \bar{Q}_m \not{D} Q_m \\ & - \frac{1}{2} \bar{U}_m \not{D} U_m - \frac{1}{2} \bar{D}_m \not{D} D_m \\ & - \frac{1}{2} \bar{E}_m \not{D} E_m \end{aligned} \quad (13)$$

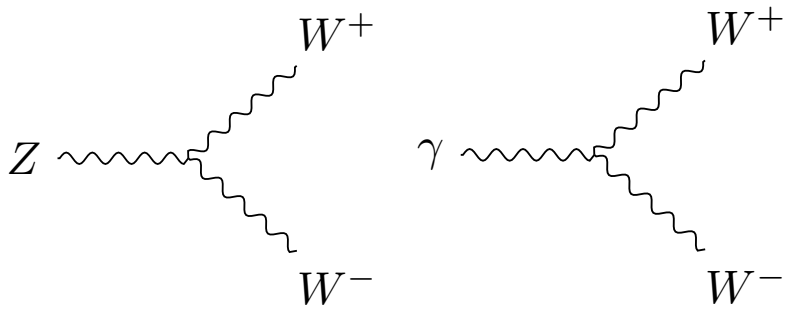


Figure 5: Trilinear gauge couplings in the SM.

where L is the left-handed lepton doublet, Q is the left-handed quark doublet, U is the right-handed singlet for up-type quarks, D is the same for down-type quarks, and E is the right-handed singlet for electrons, muons and taus. Each of these fields has an implicit index running from 1 to 3 to represent the three generations. The covariant derivative in each term includes terms including all the gauge fields the fermion is charged under. Unlike the other forces, the weak force treats left- and right-handed fermion fields differently; it only interacts with the left-handed fields, so only the first two terms' covariant derivatives include W terms. The first term in this lagrangian, for example, produces weak interactions depicted in Figure 6. The Z bosons, because they represent a mixing between the W and B fields, can interact with right-handed leptons and quarks, but do so at different rates than left-handed particles.

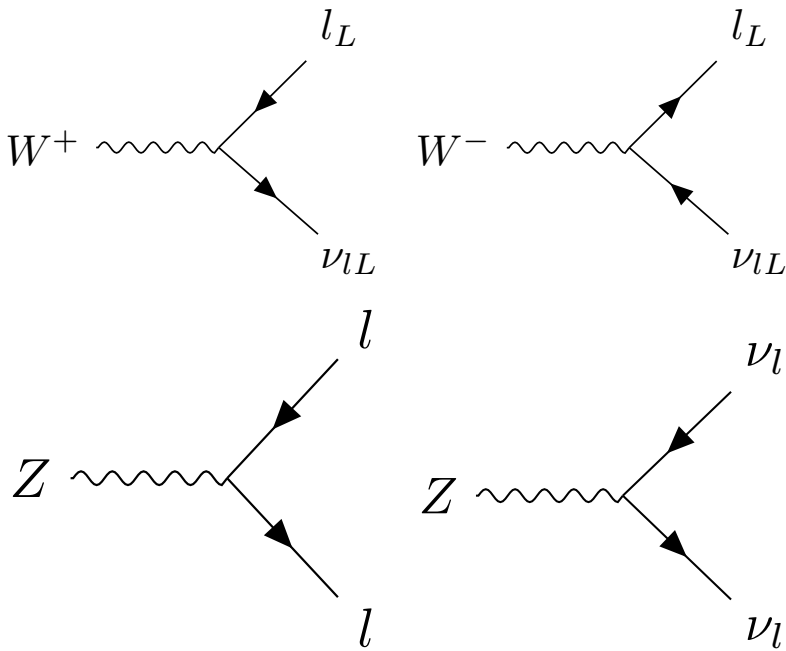


Figure 6: Weak couplings to leptons in the SM.

No right-handed term appears for the neutrino field, because only left-handed neutrinos and right-handed anti-neutrinos have been observed. However, because neutrinos have non-zero mass, their chirality can change with frame boosts, which complicates any claim that right-handed neutrinos do not exist. It is possible that neutrinos are their own antiparticle, making the right-handed anti-neutrino the solution to this problem. It's also possible that very massive right-handed neutrinos do exist, and simply haven't been discovered yet.

The remaining portions of the electroweak lagrangian are related to the Higgs field, which is the source of electroweak symmetry breaking.

2.1.2.4 The Higgs Mechanism

The Higgs mechanism presents an alternate way to generate a mass term for the electroweak gauge bosons, through an unexpected route. It is a scalar field, with a lagrangian

$$\mathcal{L}_{\text{Higgs}} = \frac{1}{2}(\partial_\mu \phi)^*(\partial^\mu \phi) + \frac{1}{2}\mu^2 \phi^* \phi - \frac{1}{4}\lambda^4 (\phi^* \phi)^2 \quad (14)$$

where ϕ is a complex scalar field, $\phi = \phi_1 + i\phi_2$. This looks very similar to a standard scalar field lagrangian, but the signs on the mass and interaction terms are reversed, implying an imaginary mass term. However, this isn't a good interpretation of the lagrangian, because differs from all previously considered lagrangians in one important way: its ground state does not occur at $\phi = 0$. Because quantum field theory is perturbative, its validity only holds when expanded around a ground state, which, when calculated for this Higgs lagrangian, must satisfy

$$\phi_1^2 + \phi_2^2 = -\frac{\mu}{\lambda}. \quad (15)$$

The original lagrangian can then be rewritten in terms of a field $v + H(x)$ centered around the ground state with energy v called the vacuum expectation value. This rewriting produces a lagrangian with a non-imaginary mass. However, in an effect called "spontaneous symmetry breaking", the original $SO(2)$ rotational symmetry of the lagrangian is lost, resulting only in a $U(1)$ rotational symmetry; the lagrangian is invariant under a phase transformation.

As in [Section 2.1.2.1](#), it is possible to make the lagrangian invariant under a local $U(1)$ transformation, $\phi \rightarrow e^{i\theta(x)\phi}$ by adding a massless gauge field A^μ and using the covariant derivative. Due to the many cross terms from the non-zero ground state, terms for the mass of one of the scalar bosons as well as the gauge field appear, leaving only one massless scalar boson. This massless boson, it turns out, can be completely removed from the theory via local $U(1)$ transformations,

ultimately producing a theory with one massive scalar (the Higgs) and a massive gauge field (W). The Higgs interaction with the weak gauge bosons also creates couplings between the particles, which can be seen in [Figure 7](#).

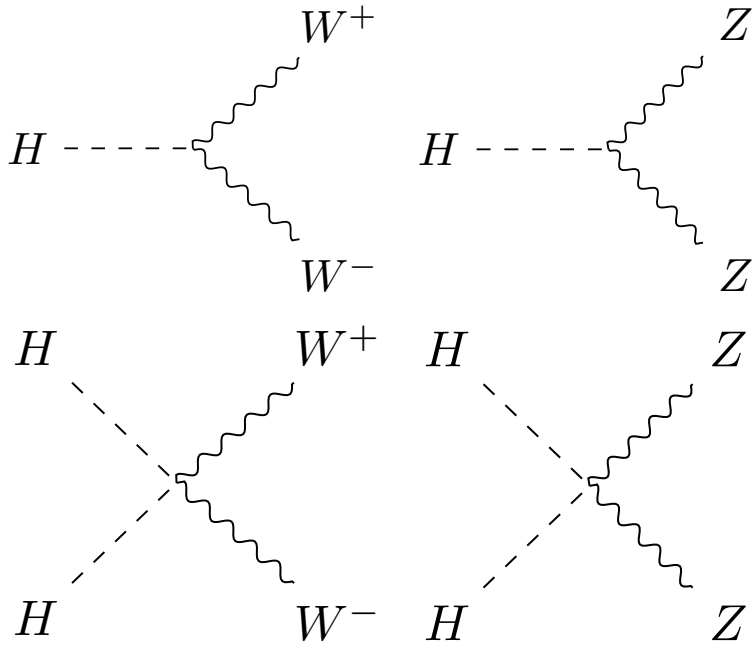


Figure 7: Higgs couplings to the weak gauge bosons in the [SM](#).

The remaining piece of the lagrangian, \mathcal{L}_{Yukawa} describes the Higgs field's interactions with the fermions of the [SM](#), and can be written as

$$\mathcal{L}_{Yukawa} = -\Gamma_{mn}^e \bar{L}_m \phi E_n - \Gamma_{mn}^u \bar{Q}_m \phi U_n - \Gamma_{mn}^d \bar{Q}_m \phi D_n + h.c. \quad (16)$$

where $h.c.$ is the hermitian conjugate term, and the Γ matrices are indexed by generation, and, when diagonalized, are proportional to the masses of the fermions. The Higgs field's vacuum expectation value produces terms that look like fermion mass terms. Additionally, terms that couple the fermions to the Higgs field are produced, with each fermion's coupling proportional to its mass. Feynman diagrams for lepton and quark terms can be seen in [Figure 8](#).

2.1.3 Phenomenology of Proton-Proton Collisions

As discussed in [Chapter 3](#), the [LHC](#) collides bunches of high-energy protons, and the interactions of these protons' constituent quarks produce the wide array of particles seen in the ATLAS detector. The [LHC](#) typically cites its energy in terms of \sqrt{S} , the center of mass energy of protons in the two colliding beams, which in Run 2 is 13 TeV. However, because the proton is not fundamental, this energy is divided among many particles that make up the proton.

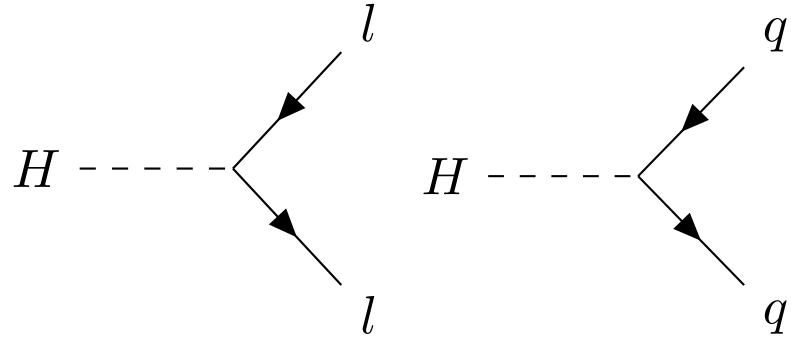


Figure 8: Higgs couplings to fermions in the SM.

To first order, a proton consists of three quarks: two up quarks and one down quark. However, a real quantum mechanical system is much more chaotic, with other quarks popping into and out of existence and gluons flying between them. These additional quarks are called *sea* quarks and can also carry fractions of the proton's energy.

The particles inside the proton can have a wide range of energies depending on the internal dynamics at the moment of the collision. These cannot be predicted exactly, but probabilistic models called Parton Distribution Functions (PDFs) describe the likelihood of any given configuration. These models are determined using data from hard scattering experiments and give probabilistic estimates for how often a given type of particle appears with a fraction x of the total proton energy, as seen in Figure 9.

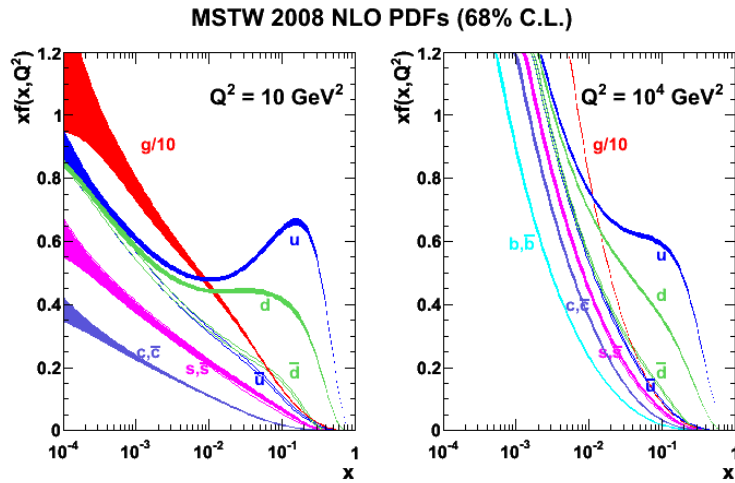


Figure 9: 2008 MSTW PDFs for various particle types given as a function of x and Q^2 , the square of the parton-parton momentum transfer. [68]

2.1.4 Problems in the Standard Model

Thought the **SM** is a self-consistent theory that describes to great accuracy all of the particles and forces it includes, it does have certain shortcomings. The most glaring is the omission of gravity. Though the force is well understood at large scales via the theory of General Relativity, no satisfying quantum description of gravity has been accepted, much less proven. The Planck scale, the energy scale at which gravitational interactions become large enough that no sound theory can ignore gravity, is at about 10^{28} eV, 16 orders of magnitude above the electroweak scale, so the exclusion of gravity from the **SM** is unlikely to directly affect **LHC** physics.

Another clear omission of the **SM** is Dark Matter (**DM**). This matter was first identified in 1933 through the observation of galactic rotation curves. [77] The speed of rotation indicated both that there was more mass in the system than could be accounted for by observations made directly of the galaxy, and that this additional matter was distributed in a halo, not a disk like the typical luminous matter. This effect can be seen in [Figure 10](#). Since then, the gravitational impact of **DM** has been observed in colliding clusters and many more rotational curves, but the particles that form **DM** have never been directly detected or seen at a particle accelerator. As a consequence, very few details are known about the nature of this matter, only its density throughout the universe and that it does not interact strongly or electromagnetically.

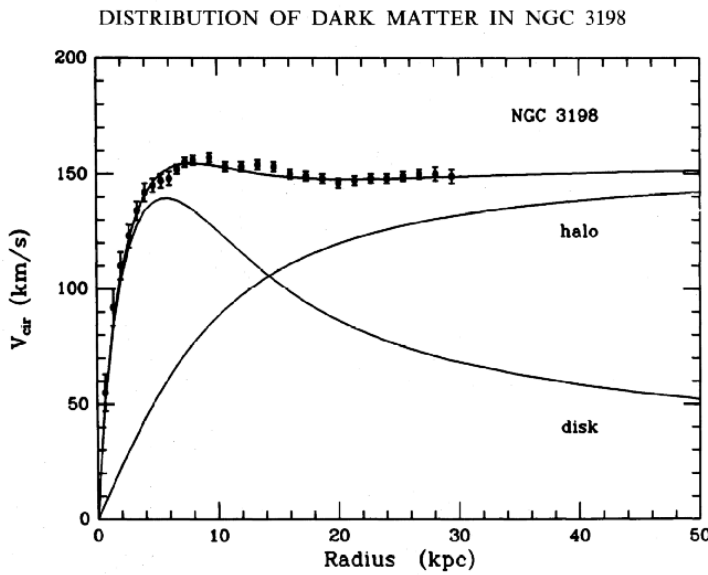


Figure 10: Galactic rotation curve showing that the discrepancy between the observed luminous matter and the total mass in the system can be described as a non-luminous halo of matter. [79]

Beyond the omissions of the [SM](#), there are several aesthetic problems - ones that could have no solution, but seem to suggest that the current [SM](#) are missing some pieces that could unify it and provide more order. The first is the sheer number of parameters in the [SM](#). There are 26 independent parameters determining the mass of the particles and all the couplings between them. Besides the rough grouping of fermions into generations, there seems to be no order to masses of particles, and no way to predict the masses or couplings. Each, it seems, is independently provided by nature.

In the past, large numbers of seemingly unrelated parameters have indicated that a theory has a more fundamental form at shorter distance scales. The large number of elements, it turned out, could be explained by different groupings of three particles, the proton, neutron and electron. Later, the menagerie of hadrons became so large that a similar reimagining of what was fundamental took place, and the theory of quarks gave an order to the many mesons and baryons. This pattern leaves physicists suspicious of any theory with too many particles and free parameters, suggesting that perhaps, at a higher energy, there is a simpler model that can unify many of the seemingly disparate elements of the [SM](#).

In addition, some of these seemingly independent parameters have suspicious symmetry. The Higgs mass, for example, has been measured to be 125 GeV. This mass is the sum of the bare mass, the one that appears in the lagrangian, and quantum corrections from interactions with other particles, which are proportional to the square of the particles' mass. Since new physics must exist at the Planck scale to account for gravity, these corrections could be up to 35 orders of magnitude larger than the Higgs mass. Though the bare mass could theoretically cancel out this massive correction, these parameters should be independent, and the odds that they would be precisely the same to 35 places are very, very small. This exact canceling is often called *fine-tuning*, an undesirable trait in a theory which suggests that some more fundamental symmetry has been missed. A *natural* solution, one free of this fine-tuning, is sought to resolve this [SM](#) problem.

2.2 SUPERSYMMETRY

Supersymmetry ([SUSY](#)) was proposed and developed in the 1970s to give solutions to many of these [SM](#) shortcomings. The theory works by introducing a fermionic symmetry to the [SM](#), in addition to the usual spacetime symmetries of translations, rotations, and changes of Lorentz frame. The combination of the usual spacetime with this fermionic dimension is called a *superspace*. Rotations in this dimension result in a particle's spin changing by $1/2$, turning a spin- $1/2$ fermion into a spin-0 particle, for example. As a consequence, this symmetry requires the existence of many new particles - a bosonic

Names	sparticles	particles	$SU(3)_C, SU(2)_L, U(1)_Y$
squarks, quarks	Q	$(\tilde{u}_L \tilde{d}_L)$	$(3, 2, \frac{1}{6})$
	\tilde{u}	\tilde{u}_R^*	$(\bar{3}, 1, -\frac{2}{3})$
	\tilde{d}	\tilde{d}_R^*	$(\bar{3}, 1, \frac{1}{3})$
sleptons, leptons	L	$(\tilde{\nu} \tilde{e}_L)$	$(1, 2, -\frac{1}{2})$
	\tilde{e}	\tilde{e}_R^*	$(1, 1, 1)$
Higgs, higgsinos	H_u	$(\tilde{H}_u^+ \tilde{H}_u^0)$	$(1, 2, \frac{1}{2})$
	H_d	$(\tilde{H}_d^0 \tilde{H}_d^-)$	$(1, 2, -\frac{1}{2})$
gluino, gluon	\tilde{g}	g	$(8, 1, 0)$
winos, W bosons	$\tilde{W}^\pm \tilde{W}^0$	$W^\pm W^0$	$(1, 3, 0)$
bino, B boson	\tilde{B}^0	B^0	$(1, 1, 0)$

Table 1: Supermultiplets of the [MSSM](#). Sfermions, on the first five rows, are all spin-0. Higgsinos and gauginos are all spin-1/2. Three sets of each fermion's supermultiplet exist, one for each generation. [69]

sfermion for each fermion of the [SM](#) and a fermionic *gaugino* for each of the gauge bosons. These superpartners of [SM](#) particles should have identical quantum numbers to the original particle, except for their spins. [Table 1](#) shows the [SM](#) particles and their superpartners.

If the theory is symmetric under these fermionic rotations, these particle-sparticle pairs can be described by a single *superfield*, which simultaneously describes the behavior of both [SM](#) and [SUSY](#) particles in the superspace. However, this completely symmetric behavior is untenable given basic observations of matter in the universe. For example, if there were a *selectron* (the superpartner of the electron, \tilde{e}), with identical mass to the electron, it would have been detected long ago. In fact, such a particle would fundamentally change atomic structure, with the bosonic selectrons capable of piling into the ground state of an atom, and removing all the interesting valence-shell interactions of electrons that determine molecular structure. Thus, if [SUSY](#) does exist, the symmetry must be broken, with much higher masses for the superpartners than the original [SM](#) particles.

2.2.1 The Minimal Supersymmetric Standard Model

The Minimal Supersymmetric Standard Model ([MSSM](#)) was designed to be the simplest supersymmetric extension of the [SM](#) that remains self consistent, and it results in the particles seen in [Table 1](#)[69]. The formulation of the [MSSM](#) begins by introducing a second Higgs doublet to account for the different masses of the sparticles. As with the [SM](#) Higgs, electroweak symmetry breaking results in the loss of degrees of freedom, and only five of the original eight states remain,

the lightest of which, h^0 , can be interpreted as the **SM** Higgs already discovered. There are two remaining neutral states, A^0 and H^0 , as well as two charged Higgses, H^\pm .

The neutral Higgs states mix with the neutral gauge bosons, while the charged Higgs states mix with the charged gauge bosons, producing a series of states labeled only by their charge and the order of their masses. The neutral states, collectively called the neutralinos, are identified from lightest to heaviest, $\tilde{\chi}_1^0, \tilde{\chi}_2^0, \tilde{\chi}_3^0$, and $\tilde{\chi}_4^0$. The charged states, referred to as charginos, are similarly called $\tilde{\chi}_1^\pm$ and $\tilde{\chi}_2^\pm$.

The **MSSM** introduces many new interactions between **SM** particles and sparticles. Though these don't represent all possible interactions, a general rule is that any **SM** vertex can have two interacting particles replaced with their sparticle equivalents, and this vertex will be part of the **MSSM**. Figure 11 gives two examples of such vertices.

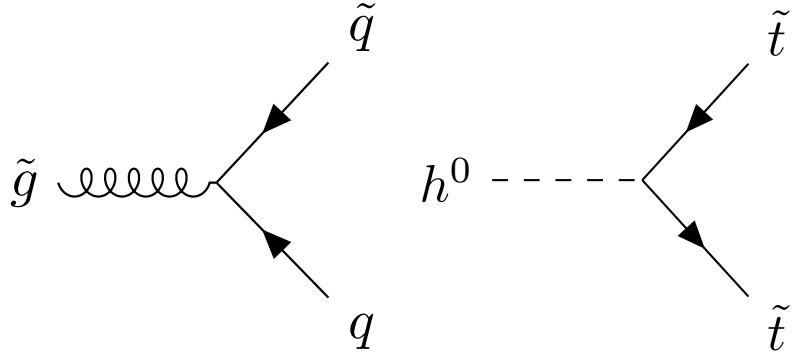


Figure 11: Two example vertices allowed by the **MSSM**.

In addition to these interactions, there are several terms that appear in the **MSSM** lagrangian that violate the B and L conservation observed in the **SM**. In fact, these terms violate $B - L$, which, unlike B and L conservation individually, does not have even small violations in the **SM**. These superpotential terms appear as follows

$$W_{\Delta L=1} = \frac{1}{2} \lambda^{ijk} L_i L_j \bar{e}_k + \lambda'^{ijk} L_i Q_j \bar{d}_k + \mu'^i L_i H_u \quad (17)$$

$$W_{\Delta B=1} = \frac{1}{2} \lambda''^{ijk} \bar{u}_i \bar{d}_j \bar{d}_k. \quad (18)$$

Because there are very strong limits on non-conservation of $B - L$ from proton decay experiments, these terms present a challenge for the **MSSM**. It would be possible, of course, to simply tune the λ parameters to be small enough to fit within experimental constraints, but these terms can also be eliminated by introducing a new conserved quantity, R -parity. It is defined by

$$P_R = -1^{3(B-L)+2s} \quad (19)$$

where s is the spin of the particle. Requiring that all terms in the lagrangian have a multiplicative P_R of 1 excludes the terms in [Equation 18](#), removing the problem of proton decay. All **SM** particles are R -parity even, while the sparticles are R -parity odd, so the conservation of R -parity can translate into a conservation of number of particles and sparticles. As a consequence, massive sparticles typically decay through a chain of lighter sparticles, emitting **SM** particles along the way.

2.2.2 Solutions to Standard Model Problems

Perhaps the most compelling consequence of **SUSY** comes from R -parity, which, through the formation of a new quantum number unique to sparticles, requires the Lightest Supersymmetric Particle (**LSP**) to be stable. This stable particle, if it is neutrally charged, provides an excellent candidate **DM** particle. The lightest neutralino, for example, is a viable **DM** candidate because interacts only via the weak force, a constraint required due to measurements of the relic density of **DM** in the universe. An interaction cross-section higher than what's expected for weak interactions would have led the **DM** particle and its anti-particle to annihilate at lower densities, leaving a much smaller amount of **DM** in the universe than what is observed today [48].

Many believe that a complete **SM** would include a unification of the three forces, as electromagnetism and the weak force have already been unified. This requires that at some higher energy, the coupling constants of all three forces merge. However, in the **SM**, the coupling constants come close to aligning, but don't perfectly cross. With the addition of the **MSSM**, the alignment is near perfect, as shown in [Figure 12](#). This may be a mathematical coincidence, but it's very compelling to those physicists who believe that "Grand Unified Theory" must exist.

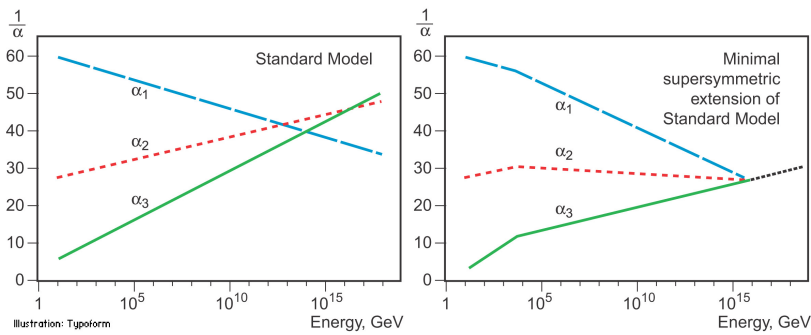


Figure 12: Running of the strong, weak, and electromagnetic coupling constants for the **SM** (left) and **MSSM** (right). [1]

SUSY also has the potential to solve the naturalness problem in the **SM**. In the **SM**, the massive amounts of fine tuning are required to cancel the quadratic corrections to the Higgs mass that result from

loops involving, most importantly, the top quark. In the [MSSM](#), an similar loop involving the stop quark (the vertex for which is depicted in [Figure 11](#)) contributes to the Higgs mass with the opposite sign, making it possible to naturally cancel the corrections without fine tuning. However, the larger the mass difference between the top quark and stop quark, the larger the remaining correction when the two terms cancel. Consequentially, to preserve a reasonable degree of naturalness (and here the definition of “reasonable” is subject to some debate), the stop quark should appear at masses not too much larger than the top’s, typically described as at the TeV scale.

This naturalness mass limit makes the argument for searching for [SUSY](#) at the [LHC](#) particularly compelling, as the [LHC](#) is the first collider capable of producing particles at the TeV scale. As new exclusions on [SUSY](#) are set, the remaining phase space becomes slightly less natural, but there is no shortage of unexcluded [SUSY](#) theories, which are continually proposed as new limits are created.

2.2.3 *Simplified Models of Supersymmetry*

There are many different theorized models of [SUSY](#), with different mechanisms for breaking the symmetry. Each of these theories typically contains on order hundreds of free parameters, with complex interactions that determine the mass hierarchy and interaction rates of the sparticles. From an experimental point of view, the details of these theories and the exact way the hierarchies are generated are often less relevant to a search than their outputs. Simplified models, which are typically inspired by more complete theories, are used to tune the observables of a model more directly.

In the analysis presented in [Part iv](#), a simplified model is used which produces the decay depicted in [Figure 13](#). This decay chain begins with the pair production of gluinos, which decay via a pair of quarks to the second lightest neutralino, which then decay via a Z boson to the lightest neutralino. In this simplified model, the lightest neutralino is the [LSP](#), and is stable.

Using this simplified model, the masses of the particles can be tuned directly. This is very helpful for the generation of [MC](#), discussed in [Section 2.3](#), because a “grid” of different mass points of the important sparticles involved in the decay can be generated, allowing analyzers to make predictions of likely signals, and to exclude the simplified models as a function of the mass of the sparticles in the case that no discrepancies between predictions and observations are seen.

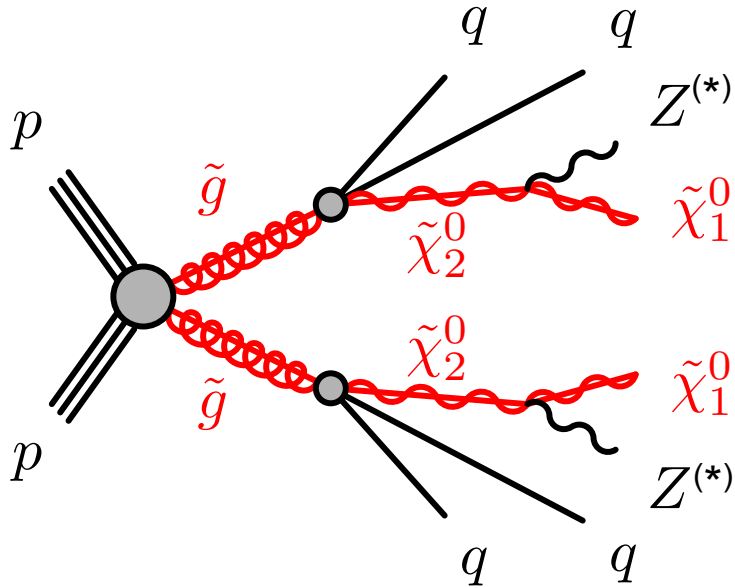


Figure 13: Feynman diagram of the decay considered in the simplified models used in the analysis presented in Part iv.

2.3 MONTE CARLO GENERATION

The complex events of the LHC are difficult to model, but modeling them is crucial to analyzers' understanding of SM backgrounds and potential signals. To simplify the modeling process, particle interactions are broken down into very small steps, each with associated probabilities of various outcomes. This modeling method is called Monte Carlo simulation (MC), and, at the LHC it is broken into several larger steps which are each handled by different software.

The first step, discussed in Section 2.1.3, is to determine the energies of the initial particles in a collision, which are provided by several different PDF sets. These distributions come from experimental measurements, though there is some variation between different sets. Three different sets are used in this analysis: NNPDF2.3LO [29] and NLO CT10 [66] for background and signal processes, and MSTW 2008 [68] for pile-up events, discussed more in Section 3.4.

With the initial states of the constituents of the protons described by these probabilistic models, the next step is to model the hard scattering process resulting from the interaction of two of these particles. This is accomplished by a generator, which calculates the cross-sections of the Feynman diagrams of a given process. In particular, these generators typically produce *matrix elements*, which describe the probability to go from an initial to final state via a hard scattering, including the kinematics of the output. Examples of generators include MG5_AMC@NLO [28], POWHEG [27, 54, 71], and SHERPA[57].

These hard scattering descriptions are then passed to the next step, where parton showering, final and initial state radiation, hadronization, and other processes can occur. Some generators, such as SHERPA, can perform this step on their own. POWHEG cannot, and is interfaced with PYTHIA [75] obtain these final state particles, as is MG5_AMC@NLO [76].

The calculation of these decays can become very complicated when more and more loops are allowed into the Feynman diagrams. The simplest calculations, which include diagrams without any loops, are referred to as Leading Order (LO), while calculations including diagrams with one loop are called Next to Leading Order (NLO), and additional Ns can be added to describe more complex calculations. In addition, the total cross-section for a given process can be calculated at a higher order and used to scale the overall number of events generated for the process.

These calculations can also be tuned, varying parameters in the generation to create outputs that most closely match experimental data. In some cases, this can mean that a tune might include values for certain physical quantities that are different from their measured values because this configuration ultimately produces a result more similar to data.

Once the final state particles of the hard interaction have been calculated, the pile-up of the LHC (described in Section 3.4) must be accounted for. Events called *minimum bias* are generated to match the overall production of the LHC collisions, with no preselection. These events are overlaid on the original hard scatter to produce a more realistic representation of the many simultaneous interactions observed in the ATLAS detector.

This collection of particles must then be translated into signals in the detector. Their trajectories in the magnetic fields of the detector, their interactions in each layer, and the way these interactions deposit charge in each subdetector are modeled in software called GEANT4 [26]. In this software, every piece of the ATLAS detector is modeled, including the magnetic field and the many different materials. Particles then follow trajectories through the simulated detector and interact with the different materials based on several preprogrammed options for each material. For example a photon traveling through a material could continue along its trajectory, convert into a positron-electron pair, or deposit energy. As it crosses into a new material, a new set of options opens up for interactions. The particle is tracked until all of its energy is lost or it exits the geometry of the simulation.

The model of the detector used for this process is iteratively perfected by comparing data to MC. Figure 14 shows an example of a discrepancy between the simulation and observed data in the number of secondary vertices in a pixel module, which should correspond

to the amount of material in the area. Observations of discrepancies like this can be used to correct the materials in the simulation.

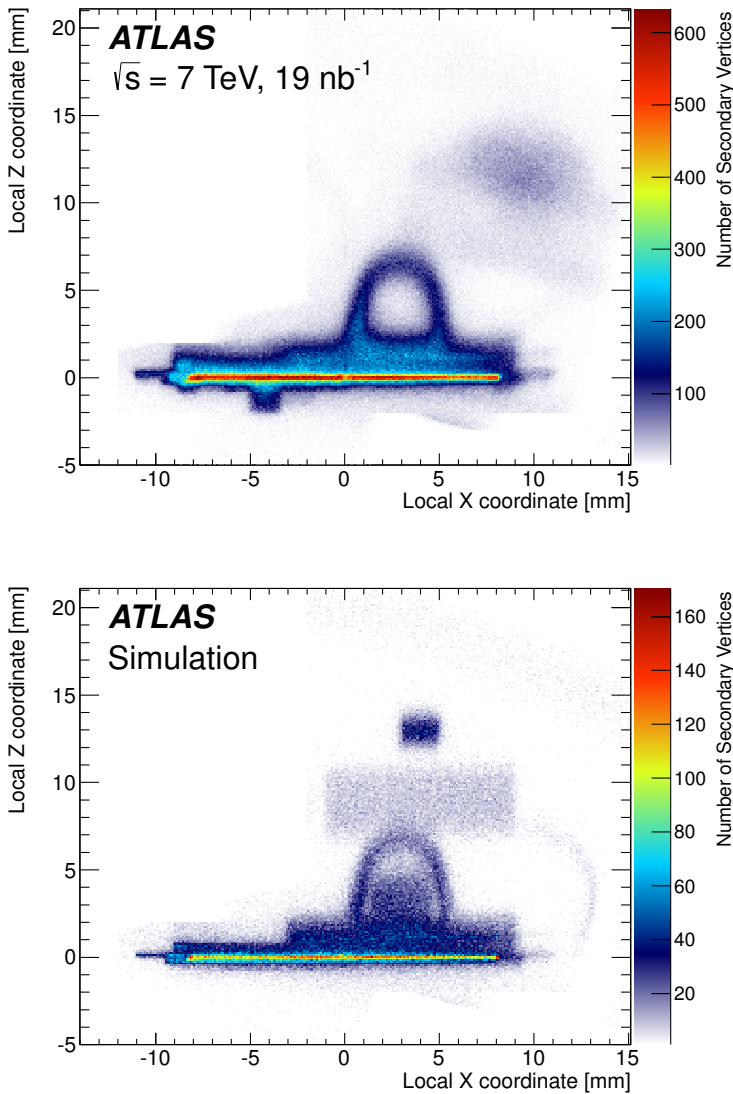


Figure 14: Number of secondary vertices in a module in the first layer of the pixel detector in data (top) and MC (bottom). There are more events in the data than the MC [25].

Custom ATLAS code converts the energy deposited in active sensors into signals that resemble the expected detector response. These responses are typically very complicated with many parameters, and are frequently iterated on to best match the data. Electronic noise must also be added to correctly approximate the operating conditions of the detector. Additional alterations to this signal translation, including dead sensors and misalignments of the detector, can also be added at this stage.

Once the simulated particles have been converted into detector signals, the same reconstruction software used on data can be used on the MC, converting the detector signals back into particle interpretations. This reconstruction process is described in [Chapter 5](#). The original information about the particles from the generator, referred to as *truth* information, is also kept, and can be compared to the reconstruction output to study its efficacy.

Part III

THE EXPERIMENT

This section describes the [LHC](#) and the ATLAS detector, which collectively provide the physical environment and the data collection for the analysis discussed in [Part iv](#).

3

THE LARGE HADRON COLLIDER

The LHC is unique in the world, producing proton-proton collisions at energies an order of magnitude higher than any accelerator before [53]. It provides unique environments at its collision points where massive, unstable particles can exist for an instant, then decay to the ordinary material of the universe. It is the goal of the ATLAS experiment to identify these short-lived particles, but LHC's work of producing them is equally complex.

The LHC sits in a 26.7 km circular tunnel that straddles the French-Swiss border outside of Geneva, originally built in 1989 for the Large Electron-Positron (LEP) collider [65]. In the LHC, two beams of protons are accelerated to 6.5 TeV, then focused and collided at four points around the ring, which can be seen in Figure 15. These points are each encased by particle detectors, which can examine the outputs of the collisions, and have different strengths and goals. The two multipurpose detectors are ATLAS and Compact Muon Solenoid (CMS), which have very complex detectors aimed and measuring as many SM particles as possible and discovering new processes [4, 45]. Large Hadron Collider beauty (LHCb) examines processes related to the b quark [46]. Meanwhile, A Large Ion Collider Experiment (ALICE) focuses on special runs of the LHC which collide lead ions instead of protons, and seeks to understand the high energy densities resulting from the collisions of such massive, complex particles [44].

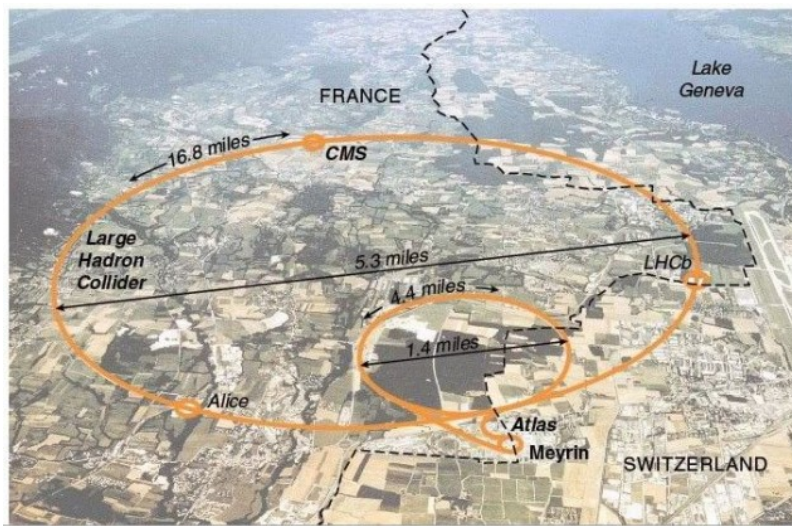


Figure 15: The LHC main collider ring and pre-accelerator SPS overlaid on a map of Switzerland and France, with the four main LHC experiments identified.

3.1 THE INJECTOR COMPLEX

The goal of the LHC is to provide high luminosity proton-proton collisions at 13 TeV. To achieve this, it must be capable of rapidly accelerating large numbers of protons and holding them at a constant energy, and organizing them into bunches which can be focused and collided at precise points and times. To do this, a complex system of pre-accelerators is required, as well as a precisely engineered system of magnets within the LHC. The full system of pre-accelerators is shown in Figure 16.

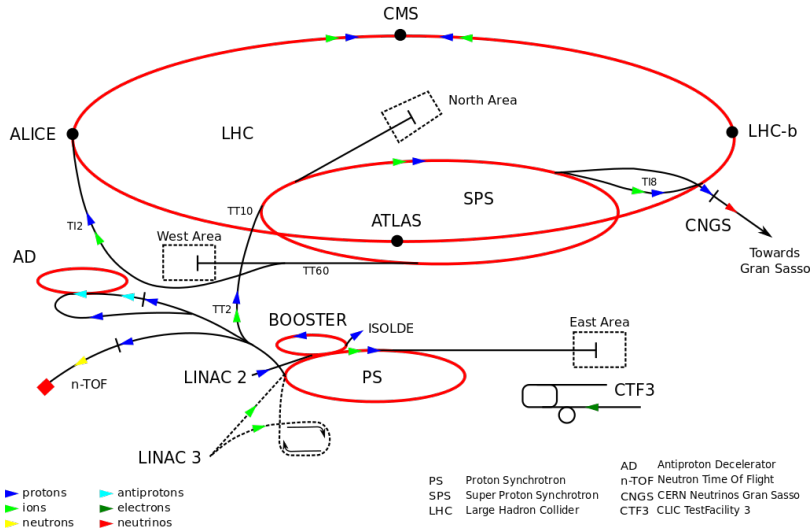


Figure 16: The pre-accelerators of the LHC.

The chain begins with when hydrogen gas is stripped of its electrons and injected in short pulses into Linac2, a linear accelerator which uses Radiofrequency (RF) cavities, which use alternating positive and negative electric fields to simultaneously push and pull particles forward through the accelerator. This RF behavoir keeps the bunches of protons resulting from the original pulses separated, beginning the formation of the bunch structure used for collisions. Quadrupole magnets along the accelerator keep the beam focused. By the end of the accelerator, protons have reached 50 MeV.

The proton beam is then injected into the Proton Synchrotron Booster (PSB), the first circular accelerator in the pre-accelerator chain. It increases its magnetic field as the protons increase in speed, ultimately accelerating them to 1.4 GeV.

At this point the proton moves on to the PS, a 600 m long circular accelerator that consists of 277 electromagnets that accelerate the protons up to 25 GeV, and 100 additional dipole magnets to bend the beam.

The last accelerator before injection into the LHC is the SPS, a 7 km long ring which, long before the LHC tunnel was built, was respon-

sible for the discover of the W and Z bosons. The [SPS](#) accelerates particles up to 450 GeV before they are launched into the [LHC](#).

Proton bunches are structured for ease of acceleration, with distinct features resulting from each of the pre-accelerators. The [PS](#) produces 72 bunches separated by 25 ns, which are injected into the [SPS](#), as seen in [Figure 17](#). However, as the magnetic field directing these protons out of the [PS](#) loop is turned on, there must be a gap in the bunch structure. Without this gap, called the injection kicker rise time, the changing magnetic field would direct particles out of the accelerator and produce high amounts of unsafe radiation around the [PS](#). A similar gap in bunch structure is required for the injection from the [SPS](#) to the [LHC](#). The injection process is repeated until the [LHC](#) is completely filled with around 2000 bunches, which takes about three minutes.

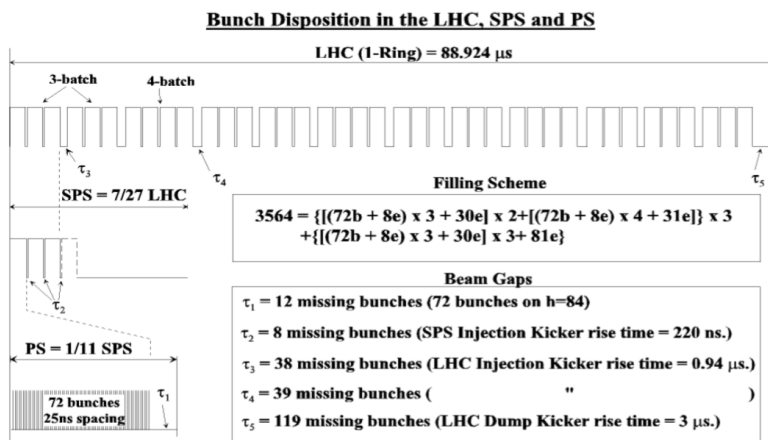


Figure 17: Bunch structure in the [PS](#), [SPS](#), and [LHC](#).

3.2 OPERATION OF THE LARGE HADRON COLLIDER

The [LHC](#) consists of eight straight sections each connected by an arc. In each straigh section, [RF](#) cavities accelerate protons, ultimately bringing them up to 6.5 GeV. Between these straight sections, 8.4 T dipole magnets bend the beams to maintain the approximately circular path. However, because the [LHC](#) is a proton-proton collider as opposed to a proton-antiproton collider, the two counter-rotating beams must be housed in separate rings and be accelerated separately. To achieve this, twin-bore superconducting magnets, one example of which can be seen in [Figure 18](#), surround the two rings and accelerate them both. Quadropole magnets are used at the four collision points to focus the beams, which cross at an interaction point at the center of a detector. In total there are 1232 main dipole magnets over 5000 additional magnets, which are all are superconducting and kept below their critical temperatures by liquid helium cooling.

LHC DIPOLE : STANDARD CROSS-SECTION

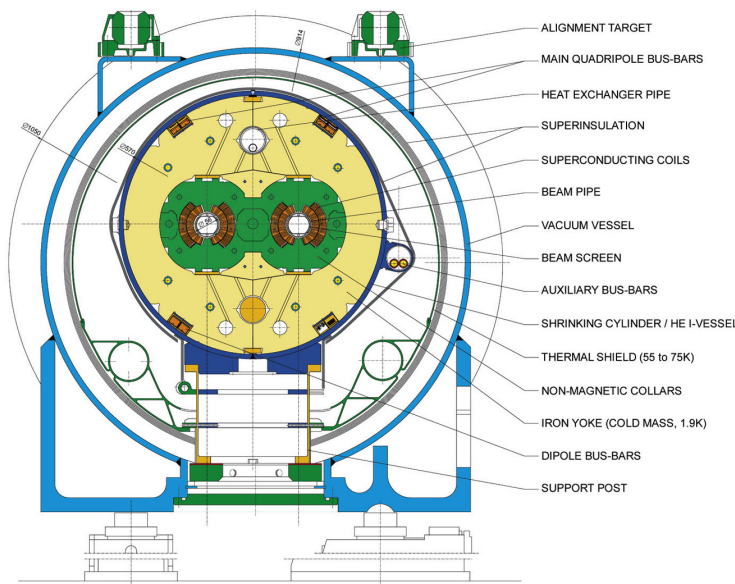


Figure 18: Cross-section of a cryodipole magnet in the LHC.

When first injected into the LHC, the protons must be accelerated over many turns through the machine, with the magnetic field from the dipoles increasing with each pass to apply more force with which to bend the beam. Once the protons have reached a maximum energy, a process called “squeezing” occurs, in which the total transverse area of the beam is reduced and bunches are elongated slightly. The shape produced by this process determines the “beam spot” for the ATLAS detector, the measurement of the area in which collisions occur within the detector. As shown in Figure 19, the collisions all occur very close together in the $x - y$ plane, but have a long spread in the z direction¹.

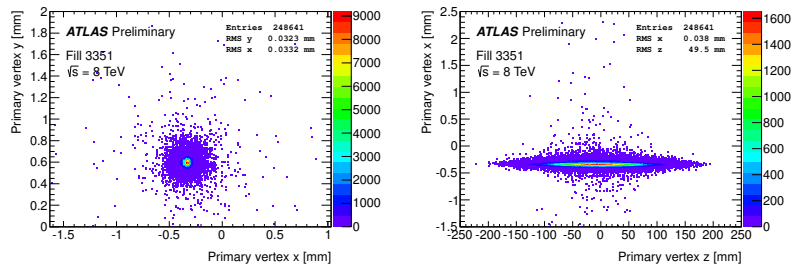


Figure 19: Beam spot in the ATLAS detector for one run in 2015. Distributions show only the highest p_T vertex per event. Left is the $x - y$ distribution of vertices, while the right plot shows the $x - z$ distribution.

Once the beams are at a stable energy and have been squeezed, the LHC indicates that it is physics-ready to the experiments around

¹ The coordinate system used here is discussed in Section 4.1.

the ring, and, after some additional checks by each experiment, data-taking can begin. As collisions occur, the beam is depleted, and when it is sufficiently depleted to require a new fill, or if any instability occurs, the beam is dumped into a cavern filled with steel and concrete, which absorbs the energy.

3.3 LUMINOSITY

The goal of the collisions provided by the [LHC](#) is to produce [SM](#) and [BSM](#) particles, which can be observed by the detectors. How frequently a given process could occur was a crucial consideration in its design. The number of events of a given type is given by

$$N_{event} = L\sigma_{event} \quad (20)$$

where L is the luminosity delivered by the [LHC](#) and σ_{event} is the cross-section of the process in question. These cross-sections vary over many orders of magnitude for different processes, as shown in [Figure 20](#), a plot of many different [SM](#) cross-sections. As a consequence, a very large amount of luminosity is required to produce the more rare events, and to have enough statistical power to differentiate them from other much more common events.

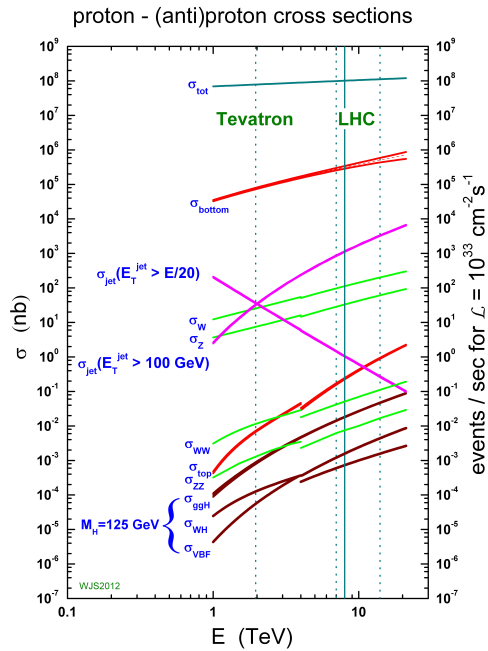


Figure 20: Cross-sections for many [SM](#) processes at the Tevatron and [LHC](#) [2].

The instantaneous luminosity at the LHC is given by

$$L = \frac{N_b^2 n_b f_{rev} \gamma_r}{4\pi \epsilon_n \beta^*} F \quad (21)$$

where N_b is the number of protons per bunch ($\sim 10^{11}$), n_b is the number of bunches in each beam ($\sim 10^3$), f_{rev} is the number of times per second that the beam travels around the ring, γ_r is the relativistic gamma factor, ϵ_n is the normalized transverse beam emittance, and β^* is the β -function at the collision point, which describes the transverse displacement of particles in the beam. F gives the reduction factor due to the geometry of the beam crossings, and is given by

$$F = (1 + (\frac{\theta_c \sigma_z}{2\sigma^*})^2)^{-1/2} \quad (22)$$

where θ_c is the crossing angle of the beams, σ_z is the RMS of the bunch length in the z direction, and σ^* is the same in the transverse direction.

As the proton beams circulate and collide, N_b decreases, producing a falling instantaneous luminosity, as seen in Run 1 example in Figure 21. In Run 2, peak instantaneous luminosity was brought up to $10^{34} \text{ cm}^{-2}\text{s}^{-1}$. This high instantaneous luminosity and consistent running resulted in much faster data collection than in Run 1, which is depicted in Figure 22.

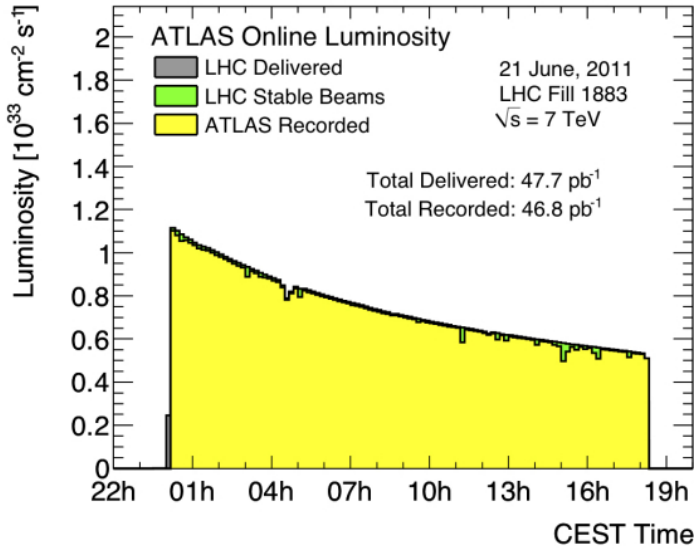


Figure 21: Instantaneous luminosity of one fill of 7 TeV data in 2011.

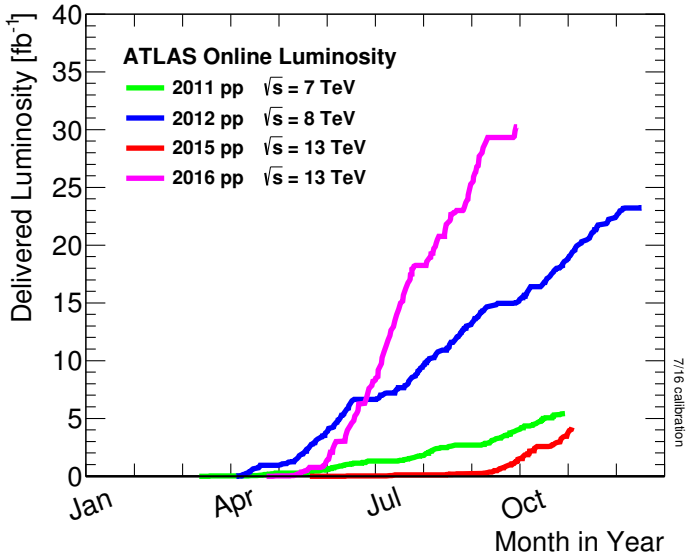


Figure 22: ATLAS luminosity for Run 1 and Run 2, as of September 2016.

3.4 PILE-UP IN PROTON-PROTON COLLISIONS

One consequence of the high instantaneous luminosity is “pile-up”, or multiple simultaneously interactions. Because each bunch has on order 100 billion protons, it is very likely that multiple protons will collide in the same bunch crossing. In fact, the average number of simultaneous interactions in 13 TeV data, shown in Figure 23, is about twenty.

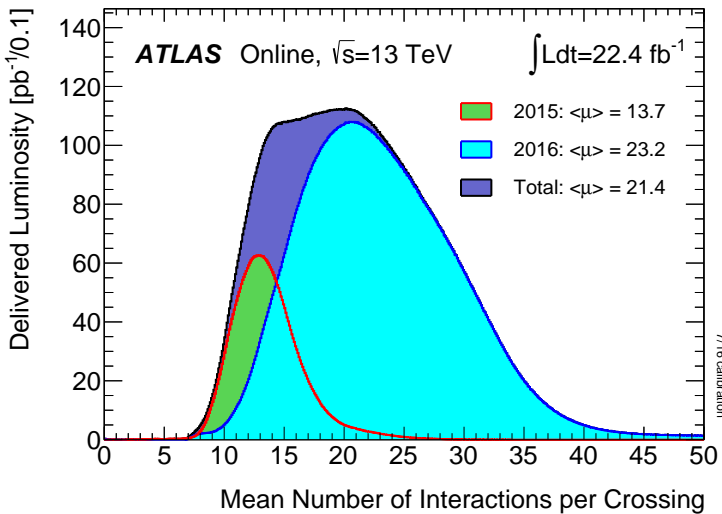


Figure 23: Average number of interactions per crossing shown for 2015 and 2016 separately, as well as the sum of the two years.

Pile-up can be a difficult challenge for the ATLAS collaboration because it typically results in additional jets in an event, and can in-

crease SM backgrounds for analyses seeking to identify events with jets. It can also add to the overall hadronic energy of an event, and that energy can be mis-assigned to other objects. Fortunately, it is typically possible to resolve the different vertices that each proton-proton collision makes, and so pile-up jets can be identified and rejected.

4

THE ATLAS DETECTOR

The ATLAS detector circumscribes the LHC’s beam pipe, enclosing the collision point with a series of particle detecting layers, aimed at making as many measurements of the particles leaving the collision point as possible. Its goal is to get a precise measurement of all the stable or semi-stable particles flying from proton-proton collisions at its center, allowing analyzers to fully reconstruct the kinematics of the underlying processes.

The ATLAS detector is the largest detector of its kind, measuring 44 m in length and 25 m in height, as seen in Figure 24. The size is mainly determined by the constraints of the MS, discussed in Section 4.4, which is the largest and outermost subsystem. The MS is submerged in a spatially varying magnetic field provided by three toroidal magnets, while the ID (Section 4.2) is encased by a superconducting solenoid, which provides a uniform 2 T field throughout its volume [4].

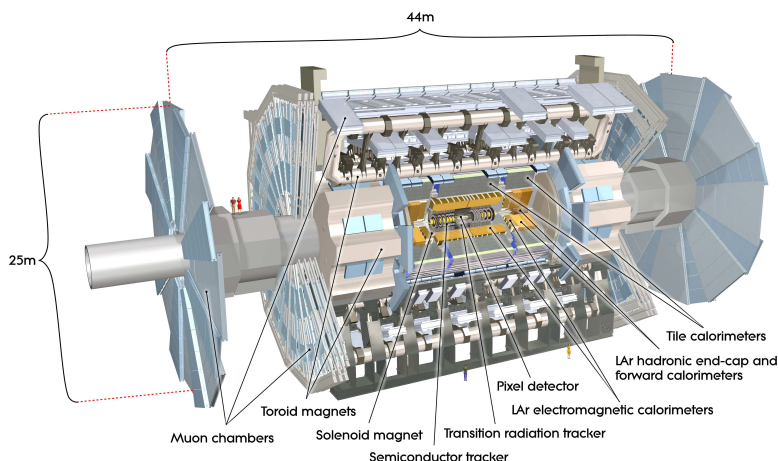


Figure 24: Diagram of the ATLAS detector, with subsystems and magnets identified.

4.1 COORDINATE SYSTEM USED IN THE ATLAS DETECTOR

The ATLAS detector is centered around the $p - p$ collision point, and is built radially out from the beam pipe, maintaining as much rotational symmetry around the beam pipe as possible. It is also symmetric in the forward-backward directions. A coordinate system using the collision point as the origin is used, with the beam line defining

the z -axis. The positive x direction is defined as pointing to the center of the LHC ring, while the positive y direction points upwards. For ease of reference, the side of the detector in the positive- z direction is referred to as the A side, and the other side is referred to as the C side.

Because of the cylindrical design of the detector, angular coordinates are often used. The azimuthal angle ϕ defines the angle around the beam pipe and the polar angle θ defines the angle from the beam axis (z). However, a transformation of the polar angle called pseudo-rapidity (η) is used more often, and is defined as

$$\eta = -\ln[\tan \frac{\theta}{2}]. \quad (23)$$

η is used because the particle distribution from LHC collisions is roughly uniform in this variable. Building on this definition, angular distance between objects is typically defined as

$$\Delta R = \sqrt{\Delta\eta^2 + \Delta\phi^2}. \quad (24)$$

Often variables are defined purely in the transverse plane, which is indicated by a subscripted T , as in p_T , which gives an object's transverse momentum.

4.2 THE INNER DETECTOR

The Inner Detector (ID) is responsible for the production of tracks, estimates of the paths charged particles take as they travel through the detector. Collisions in the detector can produce about 1000 particles, so identifying and differentiating all the tracks resulting from a collision is both a hardware and a computational challenge.

The ID consists of three separate subdetectors, each of which has multiple layers capable of producing an electrical signal, called a *hit*, when a charged particle travels through its active material. ATLAS tracking software considers all these hits and forms tracks, with the goal of minimizing fake tracks due to random noise and maximizing the efficiency of identifying a real particle. Some details of this process is discussed in Chapter 6. The full ID can be seen in Figure 25, while a schematic in Figure 26 shows more detail on the placement of each layer.

4.2.1 The Pixel Detector

The pixel detector lies closest to the beam pipe of the LHC, and has four layers comprising 92 million pixels. There are three standard layers, referred to as Layers 0-2 (L₀, L₁, L₂), and an additional layer added for the 2015 data-taking, called the Insertable B-Layer (IBL).

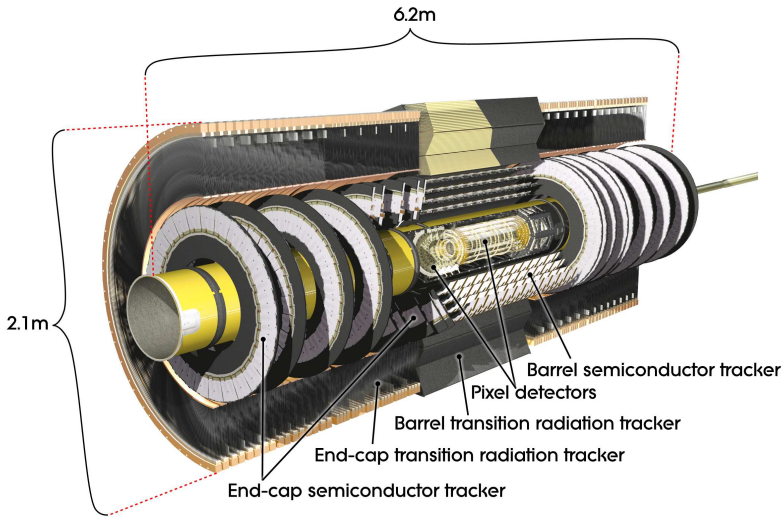


Figure 25: Diagram of the ATLAS Inner Detector, containing the Pixel, SCT, and TRT subsystems.

4.2.1.1 *The Original Pixel Detector*

The Pixel Detector consists of high-precision silicon chip pixel modules, with 1744 in total, and each module is made up of 16 sensors each with its own read-out system. Each sensor is identical, containing 47232 pixels, which are typically each $50 \times 400 \mu\text{m}^2$, though pixels at the edges of the sensors are slightly longer, at $50 \times 600 \mu\text{m}^2$.

As shown in Figure 26, the central η region (barrel) is covered by three concentric cylindrical layers of sensors, while the higher η region (end-cap) is covered by a series of three disks positioned in the $x - y$ plane. Together, they give complete coverage out to $|\eta| = 2.5$, and a particle coming from the collision point will typically produce hits in three layers.

The sensors are n-type silicon wafers with a voltage applied, and a passing charged particle produces thousands of electron-hole pairs inside the material, which drift in the electric field towards the mounted read-out system. A hit occurs when the resulting current becomes large enough to pass a threshold designed to suppress noise. A larger total charge deposit will result in the signal remaining over the threshold for a longer period of time. The initial timing of the hit, and the Time Over Threshold (ToT) are both recorded. This measurement is spatially accurate in the barrel (endcap) to $10 \mu\text{m}$ in the $R - \phi$ direction and $115 \mu\text{m}$ in the $z (R)$ direction.

4.2.1.2 *Addition of the IBL*

In 2014, the IBL was added to the pixel detector. This layer sits on top of the beam pipe, inside barrel Lo, providing a measurement of particles only about 3 cm away from the interaction point. Its addition provides greater precision for all track measurements, but it is

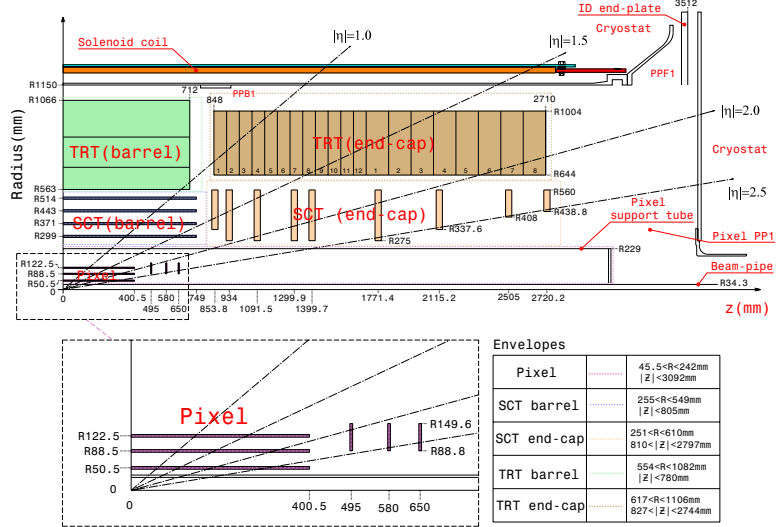


Figure 26: Diagram of one-quarter of the ATLAS Inner Detector in the $R - z$ plane, with lines drawn to indicate various η locations.

especially useful for the detection of B mesons, whose non-trivial lifetimes lead to secondary vertices in ATLAS events. The location of the IBL gives a measurement closer to these secondary vertices, and its increased pixel density increases the probability that these vertices can be resolved.

4.2.2 The Silicon Microstrip Tracker

The Silicon Microstrip Tracker (SCT) employs a similar technology to the Pixel Detector, with 15912 sensors and 6.3 million readout channels. Its difference from the Pixel Detector is in the readout, which is performed by a series of 12 cm long strips with a width of $80 \mu\text{m}$. These layers are paired, placed on top of one another at a small (40 mrad) angle to allow for position determination in both directions, giving 4 spatial measurements for each particle passing through the SCT. In the barrel, these strips run parallel to the beam pipe, while in the endcap, they are arranged radially. These strips have a resolution in the barrel (endcap) of $17 \mu\text{m}$ in the $R - \phi$ direction and $580 \mu\text{m}$ in the z (R) direction.

4.2.3 The Transition Radiation Tracker

The Transition Radiation Tracker (TRT) uses 4 mm diameter gas-filled tubes, each with a high voltage wire suspended along the center of the tube. The tubes run the length of the barrel, with a separate wire in the positive and negative z direction. In the endcap, the tubes are arranged radially. In total, there are about 351,000 readout channels in the TRT. This detector makes measurements only in the $R - \phi$ di-

rection, where the resolution of each measurement is $130\ \mu\text{m}$, and coverage extends to $|\eta| = 2.0$. Each particle typically creates about 36 hits as it passes through the [TRT](#).

Particles passing through the gas mixture of the [TRT](#) ionize the gas, producing electrons which drift towards the wire due to a potential difference applied between it and the straw. The [TRT](#) also responds to low-energy transition radiation photons, which produce a much larger signal than charged particles passing through the detector. Because of this strong difference in signals, hits from the [TRT](#) are used to help differentiate between electrons and photons in the detector.

4.3 THE CALORIMETERS

Unlike the tracking detectors, which aim to take measurements of a particle with minimal alterations of its trajectory, the calorimeters measure the energy of objects by stopping them entirely. The calorimeters, which can be seen in [Figure 27](#), provide coverage out to $|\eta| < 4.9$. High granularity electromagnetic measurements are made within $|\eta| < 2.5$ to complement the [ID](#)'s tracking capability. In this range, high p_{T} electrons and photons have nearly straight tracks, making momentum measurement through track curvature difficult, leaving the calorimeter as the primary energy measurement. The hadronic calorimeters, as well as the higher $|\eta|$ electromagnetic calorimeters, have a coarser granularity.

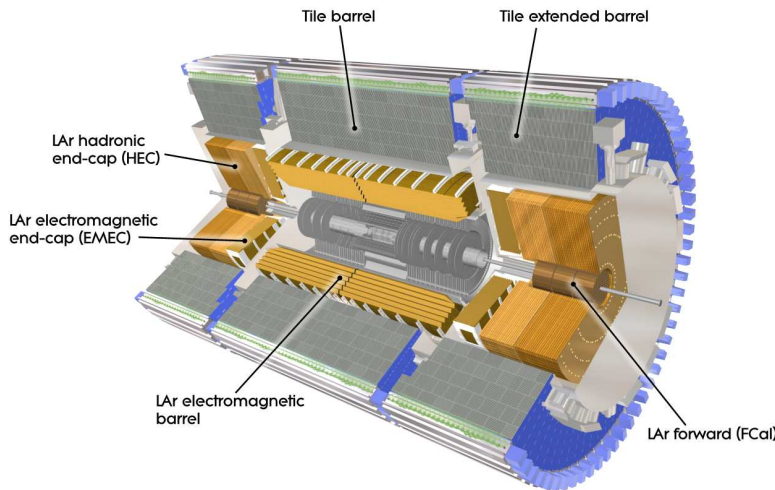


Figure 27: The calorimeter system of the ATLAS detector.

Besides measuring the energy of passing particles, another task of the calorimeter system is to limit punch-through to the [MS](#), described in [Section 4.4](#). All other particles must be fully stopped by the calorimeters to allow for clean signals from muons, and to mea-

sure the total energy of the particle. This requirement sets a minimum number of interaction lengths for each of the calorimeters.

THE LAR ELECTROMAGNETIC CALORIMETER uses liquid argon as its active detector medium alternating with layers of lead acting as the absorber. The layers are shaped like accordions, which allows for complete coverage with multiple layers of active material, three in central η ($0 < |\eta| < 2.5$) and two at higher η ($2.5 < |\eta| < 3.2$). At $|\eta| < 1.8$, an instrumented liquid argon presampler provides a measurement of energy lost prior to reaching the calorimeters. The total energy resolution for this detector is about 10%.

THE TILE CALORIMETER is a hadronic calorimeter which surrounds the LAr Calorimeter. It uses layers of steel as its absorber with scintillating tiles as the active material between them, which are read out by photomultiplier tubes. The Tile Calorimeter covers $|\eta| < 1.7$ with a typical energy resolution of about 50%.

THE LAR HADRONIC ENDCAP CALORIMETER covers the hadronic calorimetry for higher η . It uses liquid argon active material and copper plate absorbers, resulting in an energy resolution of approximately 50%. This calorimeter covers $1.5 < |\eta| < 3.2$, overlapping with the hadronic calorimeters in either direction of its η range.

THE FCAL or forward calorimeter provides electromagnetic and hadronic coverage at very high η ($3.1 < |\eta| < 4.9$). This calorimeter also uses liquid argon as its active material, and uses copper-tungsten as the absorber. Its energy resolution is about 100%.

4.4 THE MUON SPECTROMETER

The Muon Spectrometer ([MS](#)) measures charged particles that penetrate the calorimeter system. Because the calorimeters are designed to completely absorb electrons, photons, and hadrons, the [MS](#) mainly detects muons, which pass through the calorimeter with very little loss of energy. The goal of the [MS](#) is to give a high-precision measurement of these muons, and also to be able to quickly identify events with muons for the sake of triggering, discussed in [Section 4.6](#). The layout of the [MS](#) can be seen in Figures [28](#) and [29](#). Muons can be measured for all $|\eta| < 2.7$, and they can be triggered on for $|\eta| < 2.4$. The entire system is about 24 m tall and 40 m long.

To achieve these goals, the [MS](#) has several subsystems. The system responsible for precision measurement is called the Monitored Drift Tubes ([MDTs](#)). This subdetector consists of chambers of three to eight layers of tubes, with three layers of chambers covering both the barrel and end-cap regions. In the barrel, these chambers are arranged

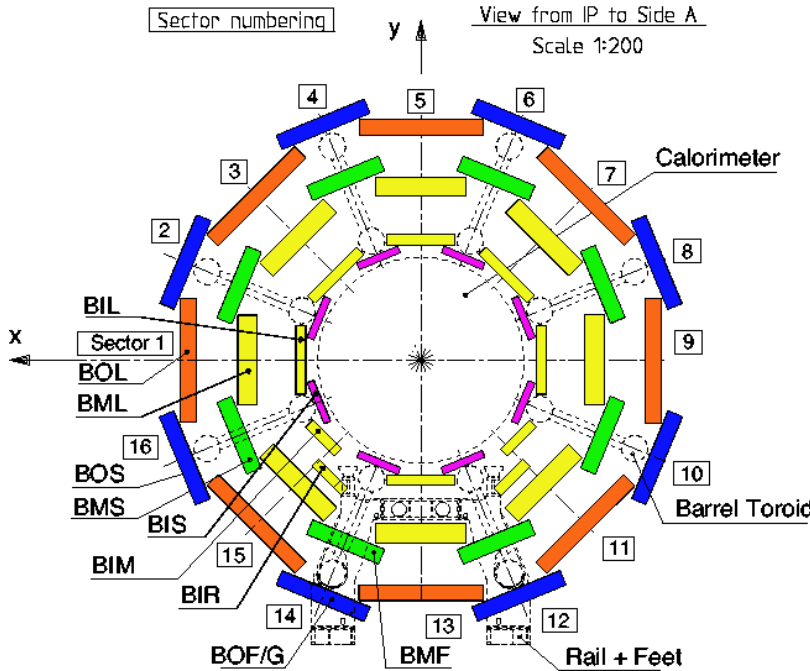


Figure 28: An x - y view of the [MS](#). In it, the three barrel layers are visible, as well as the overlapping, differently sized chambers. The outer layer of the [MS](#) is about 20m in diameter.

in layers concentric cylinders with small overlaps between adjacent chambers. The chambers are oriented such that the drift tubes are parallel to the beam line. In the endcap, the chambers form disks with drift tubes approximately aligned in the R direction.

The tubes each contain an Ar/CO₂ gas mixture and a single high voltage wire which runs at its center along its length. Charged particles excite the gas as they pass through it, producing electrons which drift towards the high voltage wire. The resulting electric signal is read out, and the magnitude and timing of the signals are both used to differentiate particle traces from noise.

Though very effective at giving a precise measurement, the [MDTs](#) have two shortcomings. The first is that the measurement is only precise in the direction perpendicular to the tubes; in the direction parallel to them, the resolution is not much better than the length of the drift tube, which are typically several meters long. The resolution in the perpendicular direction is about 35 μm with the combined measurement of all the tubes in a chamber. The second major shortcoming is that the [MDTs](#) are slow, with a maximum drift time of about 700 ns.

The slow drift time means that muons from sequential collisions can appear in the same event, and that the signals from the [MDTs](#) are received too late to be used for triggering. To solve the former problem, another detector called the Cathode-Strip Chambers ([CSCs](#)) is used in high-rate regions of the [MS](#). This detector consists of multi-wire proportional chambers which have cathode strips on either side

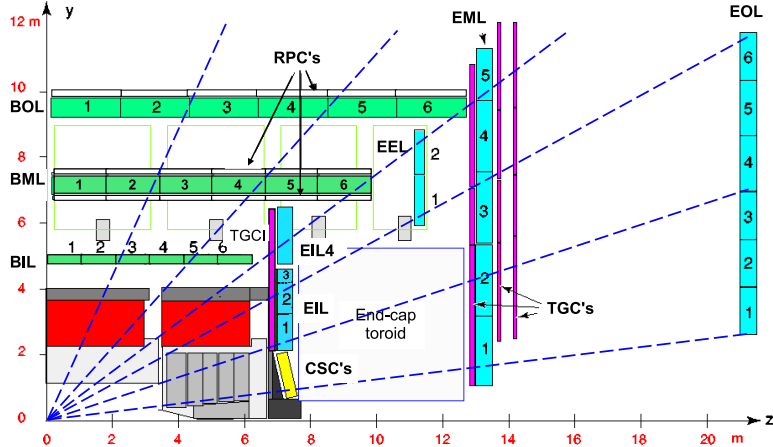


Figure 29: An r - z view of the [MS](#). The three layers of the barrel and end-cap [MS](#) are visible, and all muons at $|\eta|<2.7$ should traverse three detectors, assuming they propagate in an approximately straight line from the interaction point.

of the anode in orthogonal directions, providing a $40\ \mu\text{m}$ resolution in one direction and 5mm resolution in the other. Their drift times are much shorter than those of the [MDTs](#), at about $40\ \text{ns}$. They are placed in the forward region of the detector ($2<|\eta|<2.7$) where the incident particle rates are highest.

To achieve responses fast enough to be used for triggering, Resistive Plate Chambers ([RPCs](#)) and Thin Gap Chambers ([TGCs](#)) are used. These chambers both take less than $25\ \text{ns}$ to produce a signal. The [RPCs](#) are used in the barrel and are made up of two high-resistance plastic plates with a gas mixture under an electric field between them. Passing particles ionize this gas, and the resulting signal is read out via metallic strips mounted to the plastic plates. The [TGCs](#) used in the endcap are a form of multi-wire proportional chambers, like the [CSCs](#). Unlike the [CSCs](#), the cathode is placed extremely close to the wires, speeding up its operation.

The massive [MS](#) is subject to deformations due to gravity and the magnetic field. To achieve a high precision alignment, these deformations are constantly monitored in each [MDT](#) chamber with a set of four optical alignment rays, which give alignment information at the precision of $<30\ \mu\text{m}$. In addition, a sag-adjustment system can use this information to re-align any wires that droop under gravity's pull. Lastly, the [MS](#) can be aligned using the tracks made from hits it measures, discussed more in [Section 5.3](#).

4.5 THE MAGNET SYSTEM

The ATLAS magnet system consists of four superconducting magnets: an inner solenoid, a barrel toroid, and two endcap toroids. Collectively, they are 22m in diameter and 26m long, and their basic layout can be seen in [Figure 30](#).

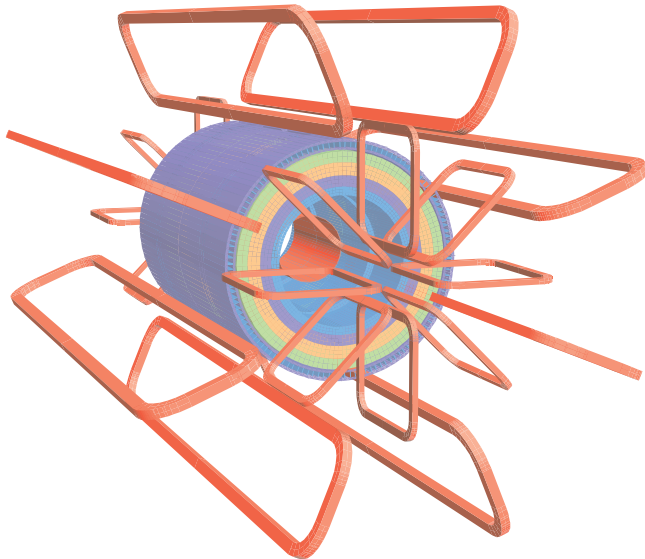


[Figure 30](#): The magnet system of the ATLAS detector. The inner cylinder shows the solenoid which gives a uniform magnetic field in the [ID](#). Outside of that are the barrel and endcap toroids, which provide a non-uniform magnetic field for the [MS](#).

The solenoid is inside the calorimeter volume and provides a uniform 2T magnetic field for particles traveling through the [ID](#). This axial field causes the trajectories of charged particles to bend in the $x - y$ plane, and measurements of the curvature of these trajectories give the most accurate p_T measurement for many particles according to the equation

$$p_T = qB\rho \quad (25)$$

where q is the charge of the particle, B is the magnetic field in the z direction, and ρ is the radius of curvature.

Because the solenoid is placed between the tracking system and the calorimeter, it is important that it interfere minimally with particles in order to allow the calorimeter to measure their full energies. The solenoid is placed inside the same vacuum chamber as the LAr calorimeter and is made of Al-stabilized NbTi superconductor with aluminum casing, giving it a total thickness of about 0.66 radiation lengths.

The barrel toroid is outside the calorimeters and provides the magnetic field for the barrel [MS](#), which varies from 0.2–2.5T. The endcap

toroids have a magnetic field range of 0.2-3.5T. All three toroid magnets are made with Al-stabilized Nb/Ti/Cu superconducting coils supported by Al-alloy struts.

The magnets are cooled with liquid helium, and take up to a month to be brought down to operating temperatures. All magnets have cold masses surrounding them to absorb heat in the event of a quench.

The B -field resulting from this magnet system can be seen in Figure 31. The plot on top demonstrates the relatively constant field rate within the barrel which drops steeply at $|z|=2$. The bottom plot shows the field integral in the MDTs as a function of $|\eta|$, demonstrating the good coverage out to $|\eta|<2.6$ excluding a transition region between the barrel and endcap, where the field changes rapidly, making precise p_T construction difficult.

4.6 THE TRIGGER SYSTEM AND DATA ACQUISITION

The LHC provides proton bunch crossings every 25 ns, and each of these events contains about one MB of data, corresponding to 40 TB/s, a completely unmanageable amount of data. In addition to this concern, many of ATLAS's subdetectors like the pixel detector and MDTs take much longer than 25 ns to read out, making keeping up with the bunch crossing rate impossible. To reduce the total data read out and allow for selective reading out of the slower detectors, a triggering system is used.

The trigger system uses fast detectors to get a coarse picture of an event's topology, which is then compared to a trigger menu, which lists the types of events that are interesting enough to keep. Overall, the trigger system reduces the 40 million events a second to about 1000 to be fully read out from the ATLAS detector.

This filtering of events is done in two steps: the L₁ trigger is implemented in hardware and reduces the initial 40MHz to 100kHz, while the HLT is implemented in software, further reducing the rate to 1kHz [18]. The L₁ trigger uses coarse granularity information from the fast read-out subdetectors: the calorimeters, the RPCs and TGCs.

The coarse grained calorimeter information used for the L₁ trigger decision is referred to as L₁ Calorimeter Trigger (L₁Calo) and uses information from all calorimeter systems. L₁Calo is responsible for all triggers excluding muons, meaning it must be capable of identifying a large number of different objects and event topologies, including high- p_T objects, E_T^{miss} , and large amounts of hadronic energy. The trigger can also identify isolated objects, objects with very few calorimeter deposits from other objects near them.

For muon triggers, the trigger algorithm looks for patterns of hits from the RPC and TGC that are consistent with high- p_T muons with origins at the interaction point.

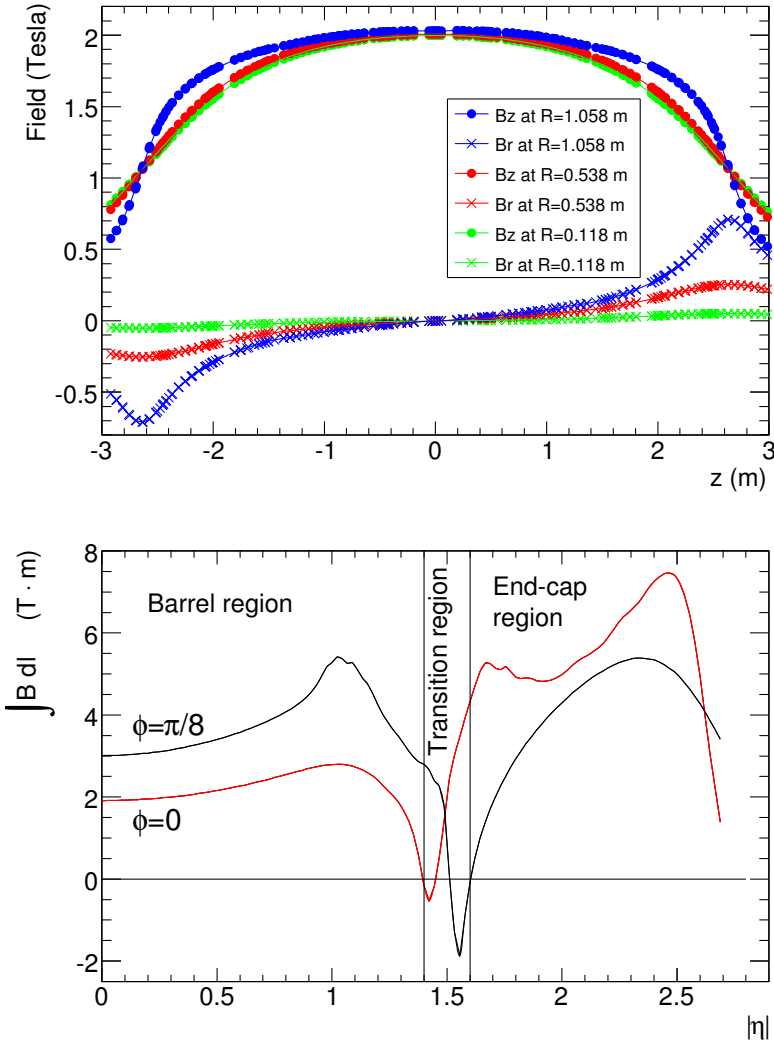


Figure 31: Plots of the magnetic field within the ATLAS detector. Top is the field (broken into its R and z components) as a function of z for several different values of R . Bottom is the field integral through the MDTs as a function of $|\eta|$ for two different ϕ values.

An example of the L_1 trigger rates for different types of events can be seen in Figure 32 for one run in July 2016. The common features to all rates are due to LHC luminosity changes, deadtimes due to detector inefficiency, and adjustment of prescales to optimize trigger bandwidth.

All of this information is analyzed by the Central Trigger Processor (CTP), which uses a trigger menu identifying all types of events to be kept to return a trigger decision. The event must be processed in about $2.5\ \mu s$ so that the remaining event information not yet read out is still available on the subdetectors when the trigger decision is made. This decision is passed to the Trigger Timing and Control (TTC), which communicates with all subdetectors. Upon receiving a L_1 trigger, the

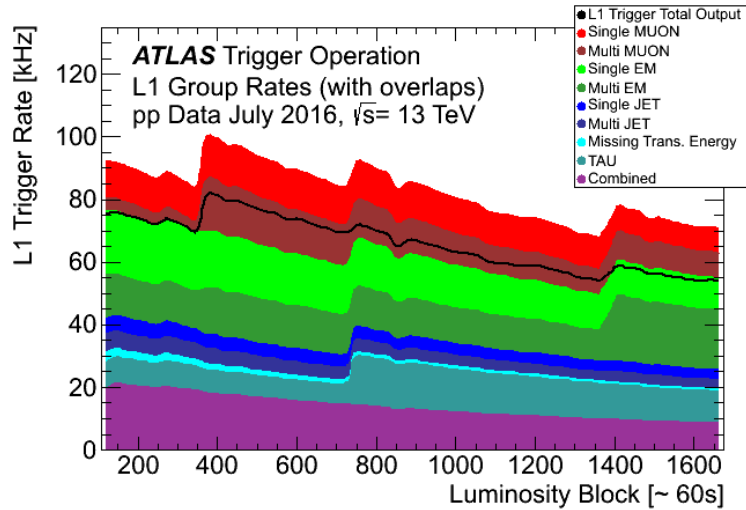


Figure 32: L_1 trigger rates for a run in July 2016 as a function of luminosity block, an approximately 60-second long period of data-taking. The total rate is lower than the combined stack because of overlapping triggers.

subdetectors read out all the information they've stored about the event and place it on their Read Out Boards (**ROBs**).

The **HLT** takes the data from particular Region of Interests (**RoIs**), areas containing interesting objects that caused the L_1 trigger, and analyzes this much more complete picture of the region to decide whether or not the event is still interesting enough to keep. This process has its own trigger menu with dedicated L_1 seeds for each item. **HLT** triggers typically have slightly higher thresholds than their corresponding L_1 triggers to ensure that events that would pass the **HLT** requirements are very likely to have passed the L_1 requirements. Figure 33 shows the **HLT** rates for the same run in July. In addition to the event types seen in Figure 32, the **HLT** can also identify events with b -jets, differentiate between electrons and photons, and identify events interesting for B-physics.

Events passing the **HLT** trigger are written to disk to be analyzed. An example of the total trigger efficiency for single electron triggers is shown in Figure 34. Trigger efficiencies can be taken directly from **MC**, and are measured in data via a method called tag-and-probe, the main principles of which are discussed in Section 10.3.

Events types that occur very frequently, such that it would require too much of the total trigger bandwidth to record all events passing a given threshold, are prescaled. Events passing these triggers are only recorded a fraction of the time, and these prescaling rates are used to adjust the final data to account for the limited rate. For example, the lowest unprescaled single electron trigger in 2016 data-taking required an electron with $60 \text{ GeV} p_T$. A trigger requiring electrons with

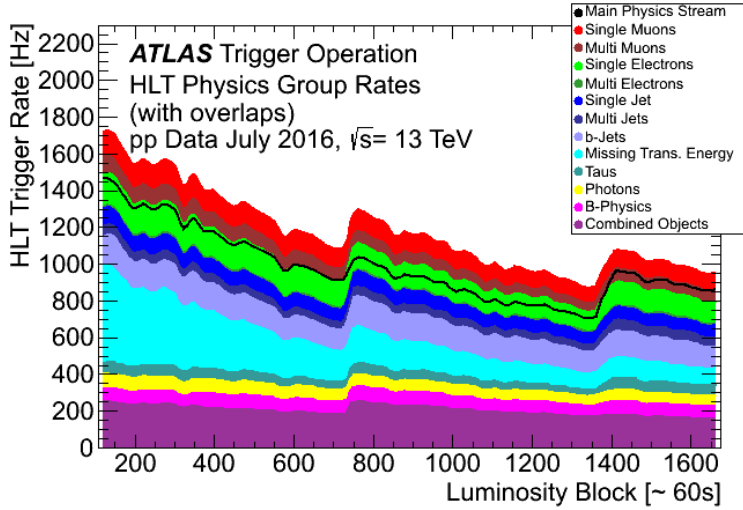


Figure 33: HLT trigger rates for July 2016 data at 13 TeV. The total rate starts around 1600 Hz and decreases to about 900 Hz by the end of the run. The plot includes a legend for various trigger categories: Main Physics Stream, Single Muons, Multi Muons, Single Electrons, Multi Electrons, Single Jet, Multi Jets, b-Jets, Missing Trans. Energy, Taus, Photons, B-Physics, and Combined Objects.

only 10 GeV p_T also exists, but is prescaled by approximately a factor of ten.

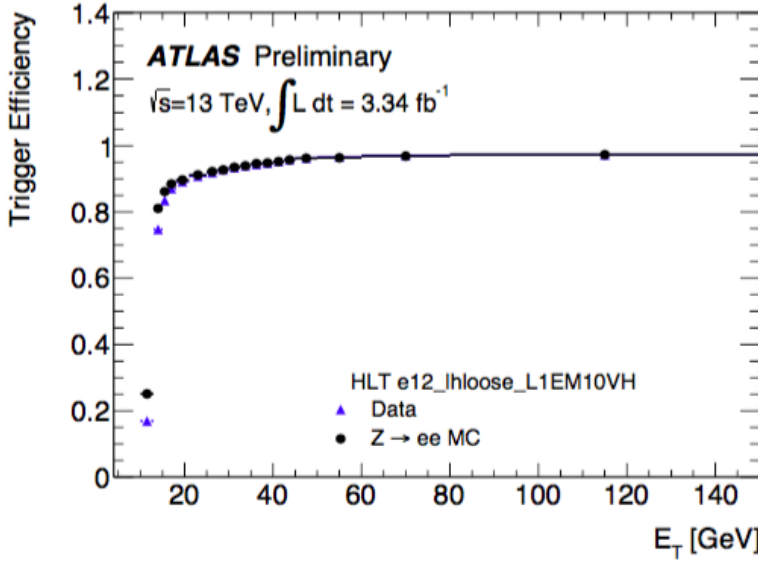


Figure 34: Trigger efficiencies as a function of E_T for data and MC. Efficiencies are given for offline selected loose electrons.

OBJECT RECONSTRUCTION IN THE ATLAS DETECTOR

Object reconstruction is the computation-intensive process of turning the signals from the approximately 100 million read-out channels of the ATLAS detector into a collection of particles and jets, the objects with which physics analysis can be performed. This process is complicated, and requires dedicated working groups in the ATLAS experiment that optimize the understanding of each type of object, which must all collaborate to provide a full picture of the events in the detector.

5.1 ELECTRONS

Electrons are identified through a combination of [ID](#) and calorimeter measurements. They travel through the tracking system, leaving charge deposits in each layer, then are absorbed by the electromagnetic calorimeter. These two measurements work in conjunction to deliver high resolution measurements of electron momentum from low- p_T , where track curvature gives the most reliable measure of the electron's energy, to high- p_T , where the tracks are almost perfectly straight, but the calorimeter can still provide a reliable measurement.

In the central region ($|\eta| < 2.47$) of the ATLAS detector, electron reconstruction begins with the identification of energy deposits in the electromagnetic calorimeter. The calorimeter clusters are seeded by sliding longitudinal windows, which are measured in units of 0.025 in η and ϕ . 3×5 unit windows are used, which require at least 2.5 GeV in the window to form a seed [52].

These clusters are matched to [ID](#) tracks by extrapolating the track to the middle layer of the calorimeter and identifying nearby clusters. If there are multiple tracks associated with a given cluster, tracks with silicon hits are preferentially chosen, and then the track with the smallest ΔR to the center of the cluster is selected. The track is used to determine the likely direction of bremsstrahlung radiation in the calorimeter, and maximum distance to match a track to a clusters expanded in the ϕ direction to account for this radiation.

The calorimeter clusters are then rebuilt in larger windows, 3×7 in the barrel and 5×5 in the end-caps. An estimate of the energy is made by summing the measured calorimeter energy with estimates of the energy lost before the electron reached the calorimeter, energy outside of the cluster window, and energy not fully deposited in the calorimeter. These estimates are made with parametrized functions

determined from a comparison of MC and measurements taken by the presampler.

The momentum is determined though a combination of the calorimeter and track measurements of the electron, while its η and ϕ are taken from the track at its vertex. The energy of the electron is taken from the calorimeter cluster.

In the forward region, where no tracking is available, electron energy is determined more roughly. Calorimeter cells are formed into variable-sized clusters in regions of significant energy deposition, and the center of the cluster is used to determine angular coordinates of the electron.

Electrons are identified using an algorithm that uses multivariate analysis to assign a likelihood that a candidate is a true electron based on input from just under twenty different variables. These include track quality, hadronic leakage, and cluster shape, incorporating information from as many subdetectors as possible in its determination of the candidate’s quality. Each variable is assigned a PDF for true electrons and background processes, and they are collectively used to provide a likelihood value which can be cut on.

Three levels of identification, LHLoose, LHMedium, and LHTight, are defined with different likelihood cuts, with tighter cuts always a subset of the looser cuts. Figure 35 gives the efficiencies at each of these working points both for true electrons and for hadrons, which can be misidentified as electrons. Tighter working points have worse efficiencies, but lower misidentification rates.

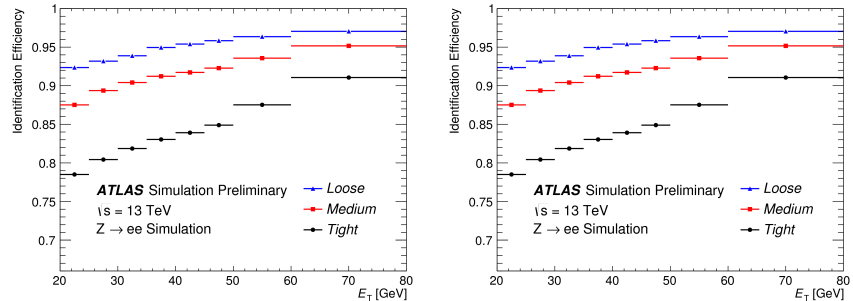


Figure 35: Identification efficiencies from MC samples for loose, medium, and tight working points. Left is the efficiency for identification of true electrons taken from $Z \rightarrow ee$ MC, and right is the efficiency for mis-identification of jets as electrons taken from dijet MC [51].

MC efficiencies can be compared to efficiencies measured in data using the tag-and-probe method, to obtain a *scalefactor*, a correction factor applied to MC to better emulate the rates at which electrons are reconstructed and identified. Figure 36 shows a comparison of the combined reconstruction and identification efficiencies in data and MC, with the resulting scalefactors also displayed as the ratio.

Electrons can also have *isolation* requirements, cuts on nearby calorimeter activity or tracks. Isolation variables are primarily used to reject

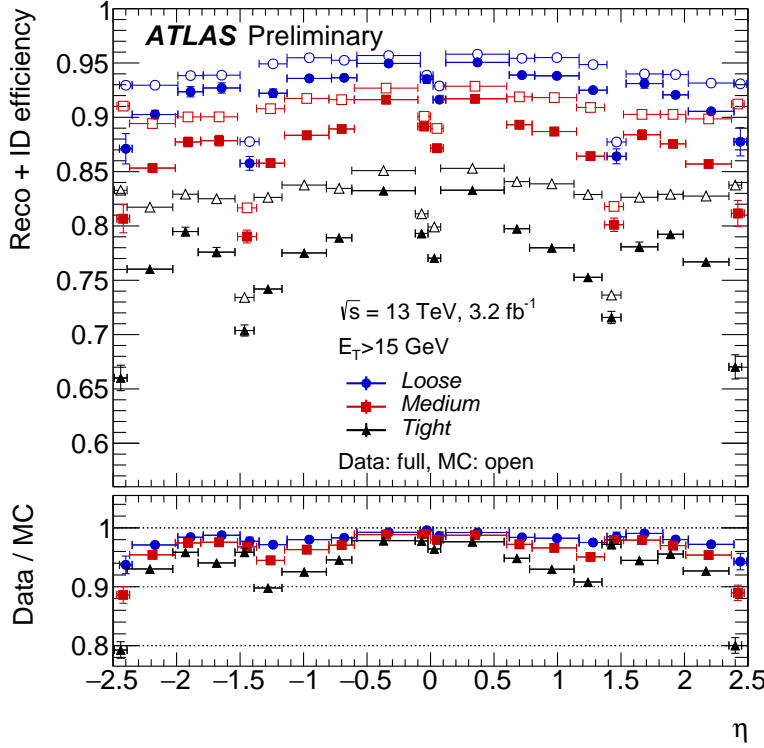


Figure 36: Combined electron reconstruction and identification efficiencies measured as a function of η for data (using the tag-and-probe method on $Z \rightarrow ee$ events) and $Z \rightarrow ee$ MC. Distributions include all electrons with $E_T > 15$ GeV. [51].

non-prompt leptons, which can be produced in heavy flavor hadron decays, converted photons, and misidentified hadrons. Cuts are made on the amount of nearby calorimetric energy and sum of the p_T of nearby tracks relative to the electron's energy, forming a series of working points. Fixed cut working points, which specify the relative fraction to cut on, can be used, but efficiency targeted working points are more popular. These include Tight and Loose working points, which operate at 95 and 98% efficiency respectively, and working points that target tighter efficiencies at higher electron p_T , Gradient and GradientLoose. These working points each have 99% efficiency for electrons with $p_T > 60$ GeV, but 90 and 95% efficiencies at 25 GeV.

5.2 PHOTONS

The reconstruction of photons is performed in parallel to electron reconstruction. Seed clustering is performed, and tracks are matched to these clusters, as in the case of the electron reconstruction described in Section 5.1.

Photons can be converted to electron-positron pairs in the ID, leaving a pair of tracks, or they can pass through without conversion,

leaving no tracks behind. As a consequence, calorimeter clusters resulting from photons can have no tracks associated with them, two tracks, or one track, in the case that one of the conversion tracks is not reconstructed. The reconstruction software attempts to identify all these scenarios and differentiate these processes from electron and hadron deposits [42].

Two-track clusters are required to consist of two oppositely charged tracks that emerge from a conversion vertex running parallel to one another. A likelihood that these are from electrons is determined using the high threshold hits in the TRT, and cuts on this likelihood are made for tracks with and without silicon hits, 10 and 80% respectively. The tracks are fit to produce the conversion vertex, and quality cuts are made, such as requiring that conversion vertices within the silicon volume correspond to tracks with silicon hits.

Single track clusters occur most often from conversions in the outermost layers of the ID, and are more difficult to reconstruct. Tracks are typically lost because the converted electron is too low p_T to be reconstructed, or because the two tracks are so close together that they're identified as a single track. The single track is required to have at least a 95% electron likelihood, and must not have a hit in the innermost layer of the pixel detector. The conversion vertex is defined as the first hit of the track.

These conversion vertices are extrapolated to the calorimeter and matched to clusters. If multiple vertices are matched to a single cluster, preference is given to vertices with double tracks, silicon hits, and finally to tracks closest to the interaction point.

Any cluster with neither a conversion vertex or a track reconstructed to it is identified as an unconverted photon. Clusters with conversion vertices are reconstructed as photons unless the cluster is also associated with an electron and the tracks associated with the cluster don't match the tracks associated with the conversion vertex. Single track clusters associated with electrons are instead identified as photons if the track has no silicon hits.

The photon's energy is determined in 3×5 (3×7) windows for unconverted (converted) photons in the barrel, where the window is expanded to compensate for the increased spread of energy from the conversion products. In the endcap, the 5×5 window is used in all cases. Like the electrons, the calibration of the photon's energy accounts for energy loss before the calorimeter, as well as energy deposited outside the cell and beyond the electromagnetic calorimeter.

Photon identification is performed in the range $|\eta| < 2.37$ using a series of cuts on the shape of the shower in the electromagnetic calorimeter, as well as the amount of additional energy deposited in the hadronic calorimeter. Photons in the the so called *crack* region of the calorimeter ($1.37 < |\eta| < 1.52$), where a discontinuity prevents accurate assessment of photon energy, are rejected. The iden-

tification has a Loose and a Tight working point. The Tight working point is used most often, and has an identification efficiency of 53–64%(47–61%) for unconverted (converted) photons with $E_T = 10$ GeV and 88–92% (96–98%) for photons with $E_T \geq 100$ GeV[74]. Efficiencies as a function of p_T measured in the 2016 data and compared to MC can be seen in Figure 37.

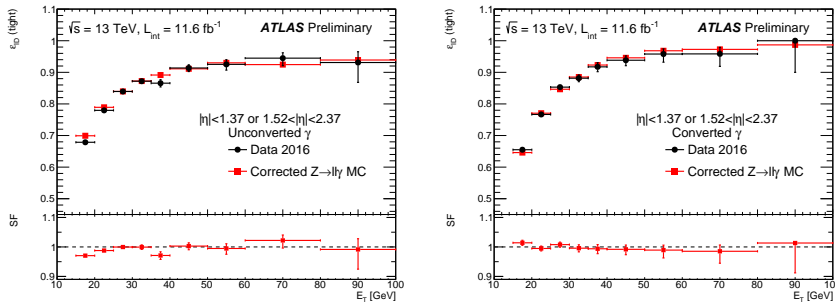


Figure 37: Comparison of tight identification efficiency measurements from data and $Z \rightarrow \ell\ell\gamma$ MC for unconverted (left) and converted (right) photons, with an inclusive η election. The bottom of each figure shows the ratio of data and MC efficiencies. [73].

Photon isolation, like electron isolation, can be determined as the combination of nearby calorimeter deposits and tracks. Fixed cuts on the isolation as a fraction of photon energy is typically used. A working point called `FixedCutTight` reconstructs the amount of calorimeter energy (excluding that of the photon) in a cone of $\Delta R = 0.4$ around the photon and the amount of energy from the sum of track p_T in a cone of $\Delta R = 0.2$. Defined relative to the photon's p_T , this working point includes photons with calorimetric isolation less than $0.022p_T + 2.45$ GeV and track isolation less than $0.05p_T$ [72].

5.3 MUONS

Muon reconstruction is performed independently in the ID and the MS, then the two measurements are combined when possible [43]. The ID reconstruction is performed using the tracking mechanism over the $|\eta| < 2.5$ range. As with electrons, hits in the layers of the ID are fit to tracks, a process described in more detail in Chapter 6.

The MS track reconstruction begins with a search in each muon chamber for patterns of hits consistent with a track, called *segments*. The MDT chamber hits are fit to a straight line, and nearby RPC and TGC chambers provide the coordinate orthogonal to the magnetic curvature for these hits. The CSC segments are required to be loosely consistent with a track originating from the interaction point.

These segments are then fit together, starting from the middle layers of the MS, with track quality requirements on the resulting combinations based on the χ^2 of the fits. Tracks must have at least two seg-

ments, except in the transition region between the barrel and endcap, where a single high quality segment can qualify as a track. Shared segments are allowed in the initial reconstruction, but after the combination, tracks with shared segments and low quality fits are removed.

These **MS** tracks are then combined with measurements from other parts of the ATLAS detector. The best quality muons are combined muons, which have **ID** and **MS** tracks associated to them, the hits of which are re-fit to form a combined track. **MS** hits can be added or removed at this stage based on their consistency with the new track. Other types of muons exist, including extrapolated muons, which have only **MS** tracks that are consistent with the interaction point, calorimeter-tagged muons, which combine an **ID** track with a calorimeter deposit consistent with a muon, and segment-tagged muons, which combine an **ID** track with a segment in the **MS**. Muons with shared **ID** tracks are not allowed, with preference given to combined muons, then calorimeter-tagged muons, and lastly segment-tagged muons.

There are four muon identification working points for muons: **Loose**, **Medium**, **Tight**, and **High- p_T** . These working points all have different efficiencies for the identification of muons, balanced against the misidentification of hadrons. One of the key variables for their discrimination is q/p significance, which quantifies the consistency between the **ID** and **MS** measurements of momentum. The χ^2 of the combined fit is also an important discriminator.

The **Loose**, **Medium**, and **Tight** efficiencies are inclusive, with all **Tight** muons passing the **Medium** requirements, for example. The **Loose** requirement includes all types of muons, but allows muons without **MS** tracks only in the $\eta < 0.1$ range where coverage of the **MS** is incomplete. The **Medium** working point includes only combined and extrapolated muons, and is the default for most ATLAS analyses. Extrapolated muons are allowed only in the η range outside the **ID** tracking system, a region often excluded by analyses because of the decreased quality. For the combined muons, at least three hits in at least two **MDT** layers are required (except in the $\eta < 0.1$ region) and a q/p significance cut is made to reduce backgrounds. Even with the reduced requirements at low η , there is a drop in efficiency in this region, as shown in [Figure 38](#). The **Tight** working point additionally cuts on χ^2 and p' , another variable that quantifies the discrepancy between **ID** and **MS** p_T measurements.

The **High- p_T** working point is designed to maximize efficiency for high- p_T muons, at the cost of lower efficiencies for low- p_T muons. Muons must have at least three **MDT** hits in three layers, which decreases efficiency but gives greatly improved p_T resolution. In addition, some regions of the **MS** with low-performing chambers are vetoed to cut down on mismeasurement. Compared to the default working point these muons have much lower efficiency: 78% (90%) for

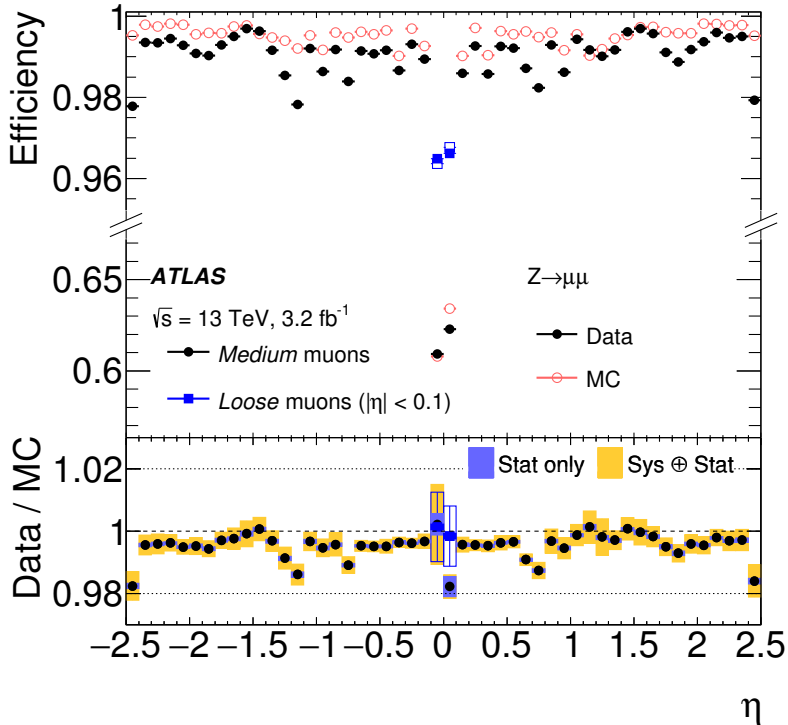


Figure 38: Muon reconstruction efficiency for the Medium working point measured with $Z \rightarrow \mu\mu$ events in data using the tag-and-probe method and in MC as a function of η . The ratio between the two is shown at the bottom. [43]

High- p_T muons compared to 96% (96%) for Medium in the p_T range of 4-20 GeV (20-100 GeV). The efficiency as a function of η for this working point can be seen in Figure 39, where the efficiency loss due to the vetoing of some chambers is especially apparent.

The most common isolation selection for muons is designed in the same way as the electron isolation, and also called GradientLoose. It is constructed such that muons with p_T of 25 GeV have an efficiency of 95%, and muons with p_T of 60 GeV have an efficiency of 99%.

5.4 JETS

Jets are the most complicated objects to reconstruct in the ATLAS detector because each jet is an assembly of many hadronic particles. In contrast to a lepton, whose reconstructed energy can easily be compared to its true energy from simulation, even a jet's true energy is ambiguous, and is dependent on the choice of the jet's definition. The standard jet reconstruction algorithm used in the ATLAS experiment is called anti- k_t [36].

This algorithm begins with calorimeter clusters defined by topologically connected cells with energy deposits significantly higher than

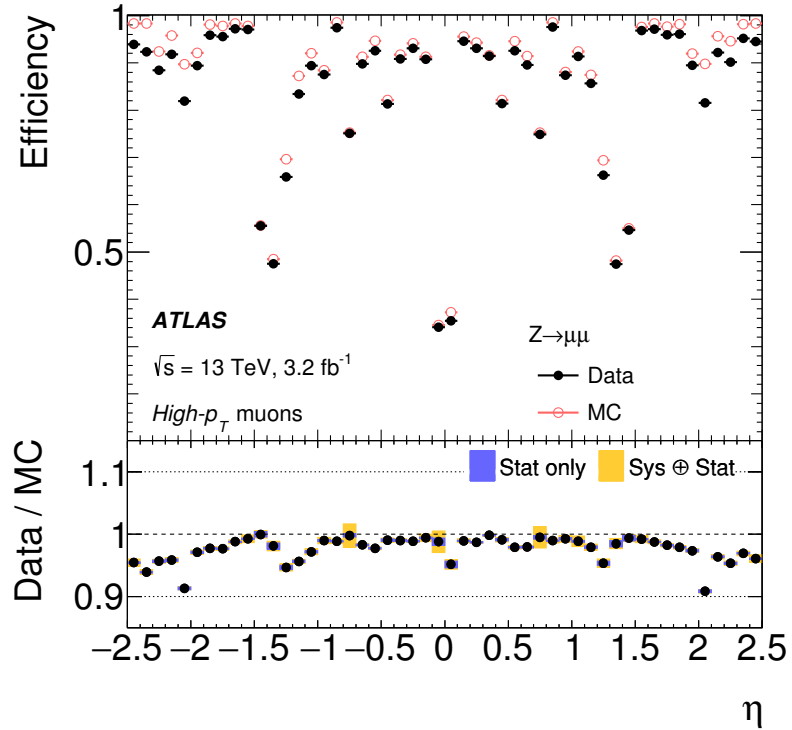


Figure 39: Muon reconstruction efficiency for the High- p_T working point measured with $Z \rightarrow \mu\mu$ events in data using the tag-and-probe method and in MC as a function of η . The ratio between the two is shown at the bottom. [43]

the noise background. In fact, there are two collections of these clusters, one with cluster energies calibrated for electromagnetic showers (**EM**), and another calibrated to hadronic showers. The second uses a method called Local Cluster Weighting (**LCW**), which first classifies a cluster as electromagnetic or hadronic based on the energy density and the shower depth, then applies a calibration according to the classification for each cluster.

The anti- k_t algorithm is then applied to these clusters, which begins with the highest energy cluster and groups it with nearby clusters according to the distance measure

$$d_{ij} = \min(k_{ti}^{-2}, k_{tj}^{-2}) \frac{\Delta_{ij}^2}{R^2} \quad (26)$$

where R is the algorithm's radius parameter, typically set to 0.4, Δ gives the angular separation of the two clusters, and k_t is the transverse momentum associated with the cluster. Clusters are added to the jet within the cone radius, then the axis of the jet is reassessed. This process is repeated until a stable jet is produced. The inverse dependence on the k_t of the cluster produces jets with energetic cores and softer edges, which matches the expectation from a hadronic

shower. In addition it is infrared and collinear safe, with neither soft emission or collinear tracks altering the reconstruction of the jet.

A series of calibrations are then applied to these jets. The first is to correct for additional hadronic energy due to pile-up, shown in Figure 40. To do this, a correction taken from MC and parametrized in terms p_T and η , as well as the number of primary vertices in the event as well as the average number of vertices, which makes correction for out-of-time pile-up possible. Next, jets are corrected to have their origin at the primary vertex instead of the center of the ATLAS detector. After that, the jets are corrected based on jet energy and η dependent Jet Energy Scale (JES) factors derived from MC. Figure 41 shows the energy response, the inverse of these factors, for EM jets. Lastly, some regions of the detector have been shown to have a bias in η measurement of jets, and this is accounted for.

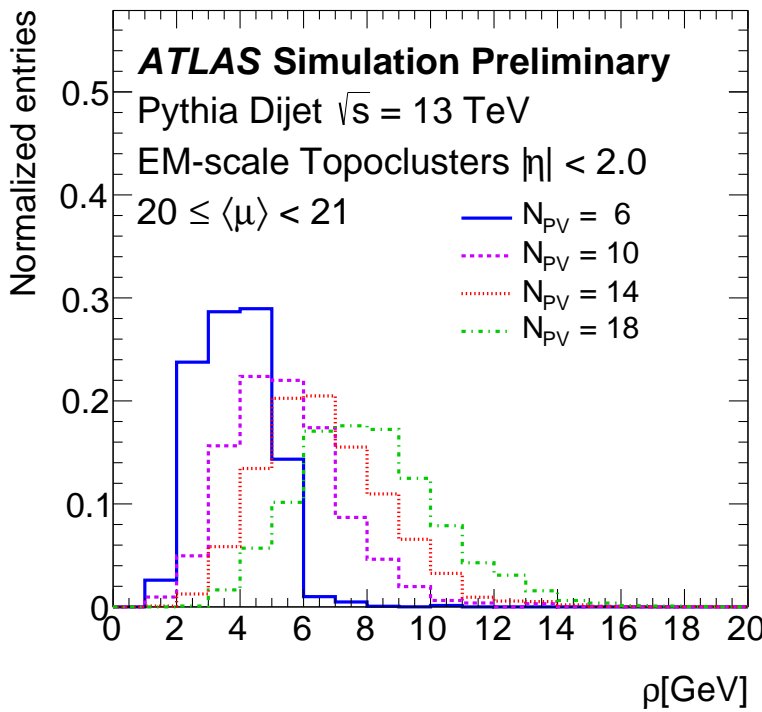


Figure 40: Distribution of event p_T density, ρ , taken from MC dijets for different numbers of primary vertices. [13]

In addition to correcting for additional energy due to pile-up, it is necessary to reject reconstructed jets that come from pile-up vertices. To accomplish this, a multivariate algorithm called **JVT** was created which builds upon an older method, **JVF** [10]. The original method vetoed jets by summing the total p_T of associated tracks and assessing the fraction of that p_T that came from tracks associated with the event's primary vertex. This fraction decreases with higher pile-up, making the construction of an explicit cut difficult in pile-up varying conditions. **JVT** improved on the method by producing a pile-up cor-

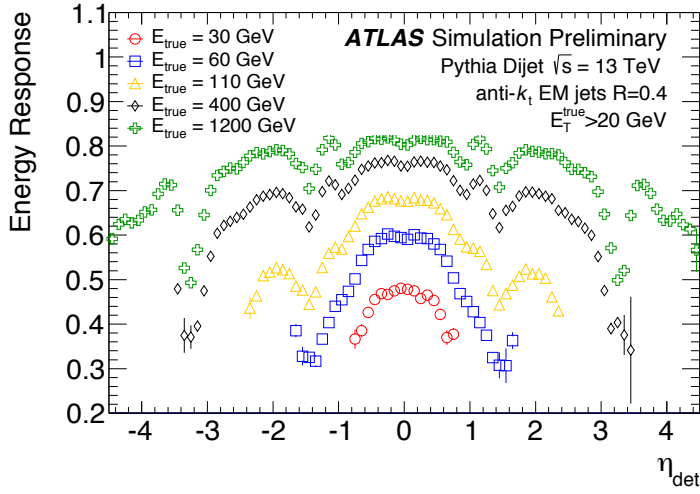


Figure 41: Energy response as a function of energy and η for EM jets in dijet MC. [13]

rected JVF variable and including it in the inputs of the tagger with other variables including a similar variable, where the sum of track p_T is replaced with the calibrated jet p_T . Figure 42 shows the efficiency and fake rate for the two methods, demonstrating JVT’s superior ability to reject pile-up jets even in events with many pile-up vertices.

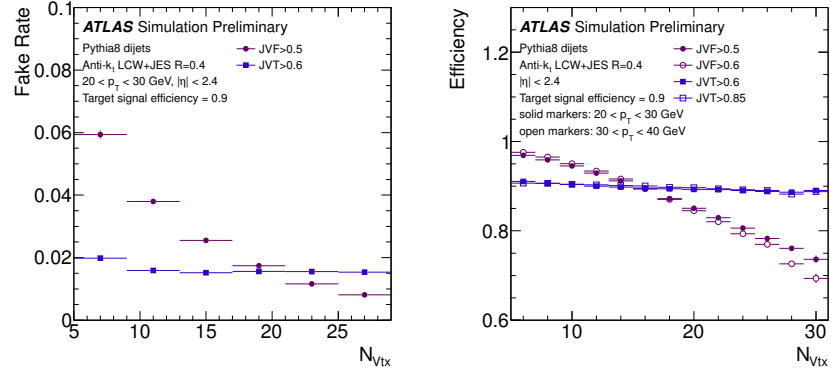


Figure 42: Dijet MC distributions of the number of pile-up jets passing the JVT and JVF cuts (left) and the efficiency for jets from the primary vertex (right) as a function of number of primary vertices in the event [10].

It is possible to differentiate jets resulting from b -hadron decays from other jets due to the non-negligible lifetimes of the hadrons. Many BSM processes preferentially produce b quarks, as does any process involving top quarks, so this identification can be very useful for targeting specific decays in many analyses. Multivariate tech-

niques are used to identify secondary vertices using the ID[12]. In ATLAS, separate algorithms are used to identify jets with tracks with significantly non-zero impact parameters, tracks that reconstruct a secondary vertex, and tracks that can be identified with a chain of vertices beginning with the primary vertex. This information is fed into a boosted decision tree called MV2c20, which outputs a discriminant shown in ???. Using this discriminant, a working point is chosen such that b -jets can be identified with a 70% efficiency, with mis-identification rates at around 12% for c -jets and 0.2% for light-flavor jets.

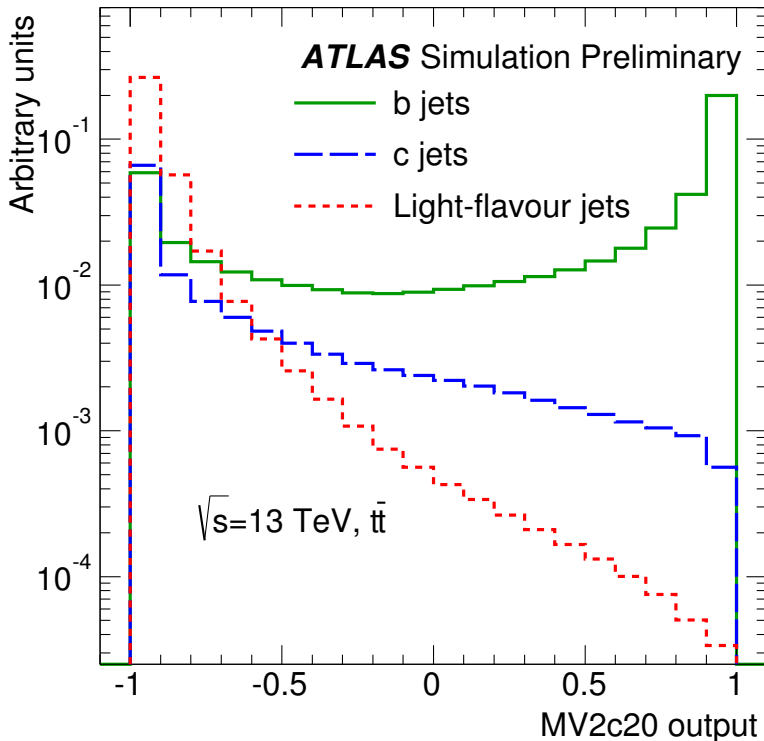


Figure 43: Distribution of MV2c20 output for b -jets, c -jets, and light-flavor jets [12].

5.5 OVERLAP REMOVAL

5.6 MISSING TRANSVERSE ENERGY

Another common usage is E_T^{miss} , which gives the negative vectorial sum of the energy in an event.

APPLICATION OF A NEURAL NETWORK TO PIXEL CLUSTERING

6.1 CLUSTERING IN THE PIXEL DETECTOR

Creating tracks from individual hits in the Inner Detector is one of most computationally challenging parts of the reconstruction of ATLAS events. Each event typically contains thousands of hits in the pixel detector alone, which must be combined into one coherent picture of which particles traversed the detector, and how they moved and lost energy as they traveled. A typical particle deposits charge in several pixels per layer, forming a series of clusters which can be connected together to form a track. This track can in turn be used to measure the charge, momentum, and trajectory of the particle.

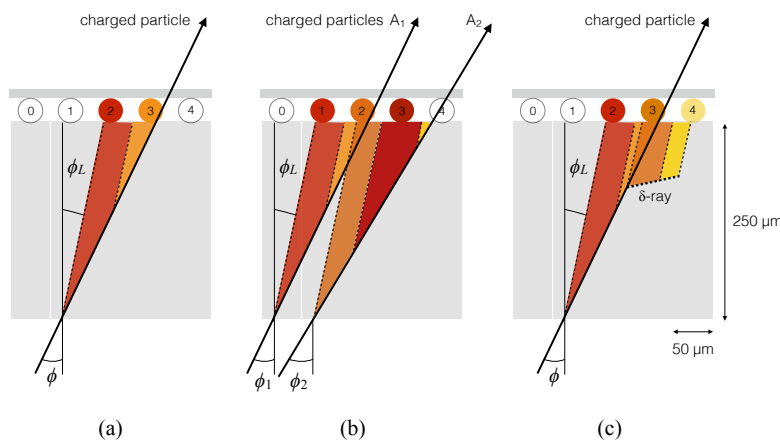


Figure 44: A few possible types of clusters in the Pixel Detector. (a) shows a single particle passing through a layer of the detector, (b) shows two particles passing through the detector, creating a single merged cluster, and (c) shows a single particle emitting a δ -ray as it passes through the detector.

The process of going from clusters to track is relatively simple in an isolated environment in which one particle travels cleanly through all the layers, but can be complicated by multiple close-by tracks and by a single particle's emission of low energy particles, called δ -rays. In these cases, it can be hard to tell how many particles were involved in creating a cluster, and where exactly each of those particles passed through the layer. A few examples of particle interactions with the pixel sensor can be seen in Figure 43 . The process of determining which pixels with charge deposits belong to a single particle is called

clustering, and it has recently been updated from a charge interpolation method to a method using a [NN](#).

6.1.1 Charge Interpolation Method

A typical cluster contains a few pixel hits spanning in the x and y directions, each with its own measurement of charge deposition, or [ToT](#). The extent of the cluster is defined by grouping together any pixels with a shared edge or corner. In the charge interpolation method, also called the [CCA](#) clustering algorithm, these individual hits are combined to make one estimation of the position a single particle which passed through them, using the following equation:

$$x_{cluster} = x_{center} + \Delta_x(\phi, N_{row}) \cdot \left[\Omega_x - \frac{1}{2} \right] \quad (27)$$

$$x_{cluster} = x_{center} + \Delta_x(\phi, N_{row}) \cdot \left[\Omega_x - \frac{1}{2} \right] \quad (28)$$

where $\Omega_{x(y)}$ is defined by

$$\Omega_{x(y)} = \frac{q_{last\ row(col)}}{q_{first\ row(col)} + q_{last\ row(col)}} \quad (29)$$

and q represents the [ToT](#) of a given pixel, and $\Delta_{x(y)}$ is a function derived from either data or [MC](#) and produces an output related to the projected length of the particles track on the pixel sensor and is measured as a function of ϕ , the incident angle of a particle on the sensor, and $N_{row(col)}$, the number of pixels in the x and y direction.

In a simple case, such as (a) of [Figure 43](#), this method works quite effectively. However, in cases like (b), it has no ability distinguish two-particle from one-particle clusters, and can only assign a cluster center between the two particles' locations, despite that intermediate pixel having the lowest [ToT](#). Furthermore, because this method can't differentiate two-particle clusters, the tracking software can't use that information to preferentially allow multiple tracks to be fit to the cluster. In cases like (c), the δ -ray will bias the measurement of the particle's position in whichever direction it is emitted.

6.1.2 Improving Measurement with Neural Networks

To address these problems, a series of [NNs](#) were created [8]. The first estimates the number of particles in a given cluster, the second predicts their positions within the cluster, and the third assesses the uncertainty of the position measurement. They are referred to, respectively, as the "Number", "Position", and "Error" [NNs](#).

These [NNs](#) are all trained with:

- a 7×7 grid of cluster **ToT** information¹
- a 7-element vector containing the y -size of the pixels in the grid²
- the layer of the pixel detector that the cluster was observed in
- a variable indicating whether the cluster is located in the barrel or endcap
- θ and ϕ variables projecting the incident angles of the particle on the sensor, assuming it comes from the nominal interaction point
- the pixel module's η index, a label assigned to each module that is roughly proportional to its η position

After the Number **NN** predicts a number of particles associated with the cluster, required to be between 1 and 3, the same inputs are fed to one of three Position **NNs** based on the determined number of particles, which then outputs the x and y positions of each of the particles. Then, the same inputs combined with the output of the Position **NN** are fed into one of three Error **NNs** (also distinguished by number of particles), which outputs an uncertainty for each of the position predictions made. An example of the output of this process can be seen in [Figure 44](#), where the improved position resolution from the ability to identify a multi-particle cluster is evident.

The particle location predictions from the **NNs** are then handed to the tracking software, which now can use these multiple particle position predictions as independent hits to be fit. As a result, tracks in dense environments have fewer clusters shared between multiple tracks, and their trajectories are known to a greater degree of precision.

6.2 IMPACT OF THE NEURAL NETWORK

The **NN** was first applied to 7 TeV data, where it improved position resolution for particles in small and large clusters. [Figure 45](#) shows the improvement from the addition of the **NN** in x resolution in different cluster sizes. The improvement from **CCA** clustering is particularly evident in the 4-pixel case, where the double peaked structure of the interpolation method has been completely removed with the **NN**.

¹ Clusters spanning more than seven pixels in either direction are split into multiple clusters.

² The pixel detector contains some long pixels at the edges of modules, and this is intended to help the **NN** identify these cases.

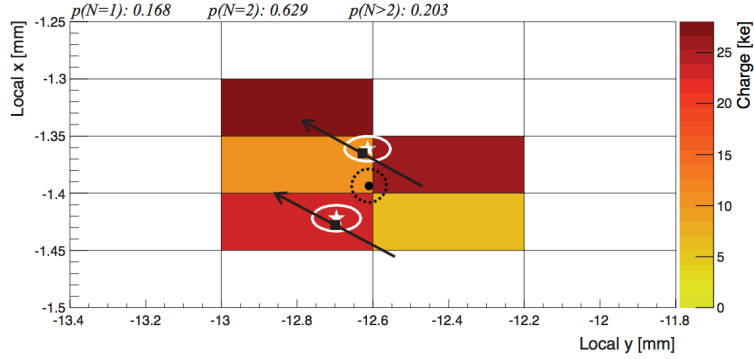


Figure 45: One example of a two-particle cluster and its truth information compared with the output of the NNs. The boxes represent pixels, with a color scale indicating ToT. At top, the $p(N = i)$ values give the output of the Number NN, the probabilities that the cluster contains 1, 2, and 3 particles. Given the highest probability is for $N = 2$, the other NNs predict the position and errors of the two particles (in white). The black arrows and squares represent the truth information from the cluster, and the black dot and dotted line show the position measurement for the un-split cluster.

6.2.1 The Neural Network in 13 TeV Data

In Run 2, the tracking algorithm is first run on the CCA clusters, where it constructs loose tracks that allow shared clusters, clusters to which multiple tracks are fit [14]. The NN is then used to identify which clusters are likely to have had multiple particles pass through them, and to identify the positions of those particles. In the case that the cluster is determined to have resulted only from one particle, tracks that share that cluster are penalized by decreasing its “track score”, a measure of the quality of the track.

With this configuration, studies were done to determine how accurately MC could model the NN’s response to data. Figure 46 shows a comparison of how often the NN identifies different types of clusters in data and MC. Very good agreement was seen between the two samples.

With this confirmation that studies performed in MC would be good indicators for performance on data, the robustness of the NN was investigated with 13 TeVMC [15]. The goal of these studies was to determine which variables the NN’s predictions were most sensitive to, and whether it was likely that these variables could be mismodeled enough to produce unexpected results in data. One example of a sensitive variable is the overall charge scale, which is tested by scaling the ToT of all pixels in a cluster up and down. The impact of its scaling can be seen in Figure 47. In this case, the likelihood to misidentify multi-particle clusters and single particle clusters depended significantly on this scaling. Overall, it was found that variations on the

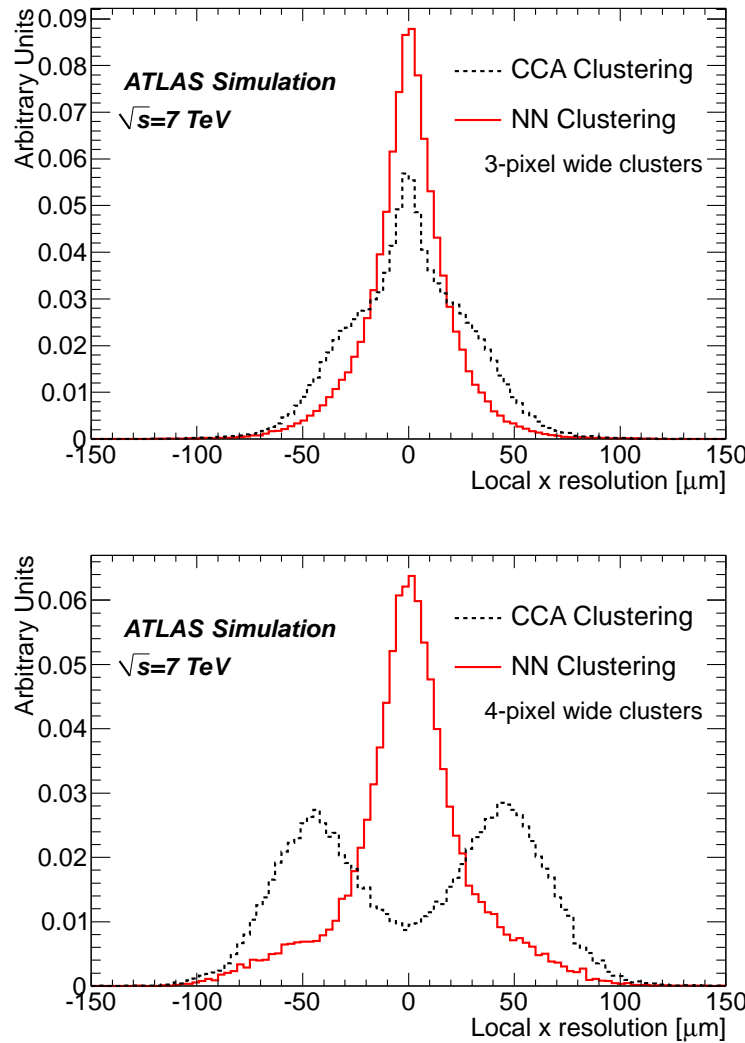


Figure 46: x resolutions for clusters with 3 (top) and 4 (bottom) pixels in the x direction in 7 TeV data for CCA and NN clustering taken from MC.

cluster charge produced a significant impact on predictions, while all other variations, such as incidence angle variation and spatial smearing of charge, had a minimal effect.

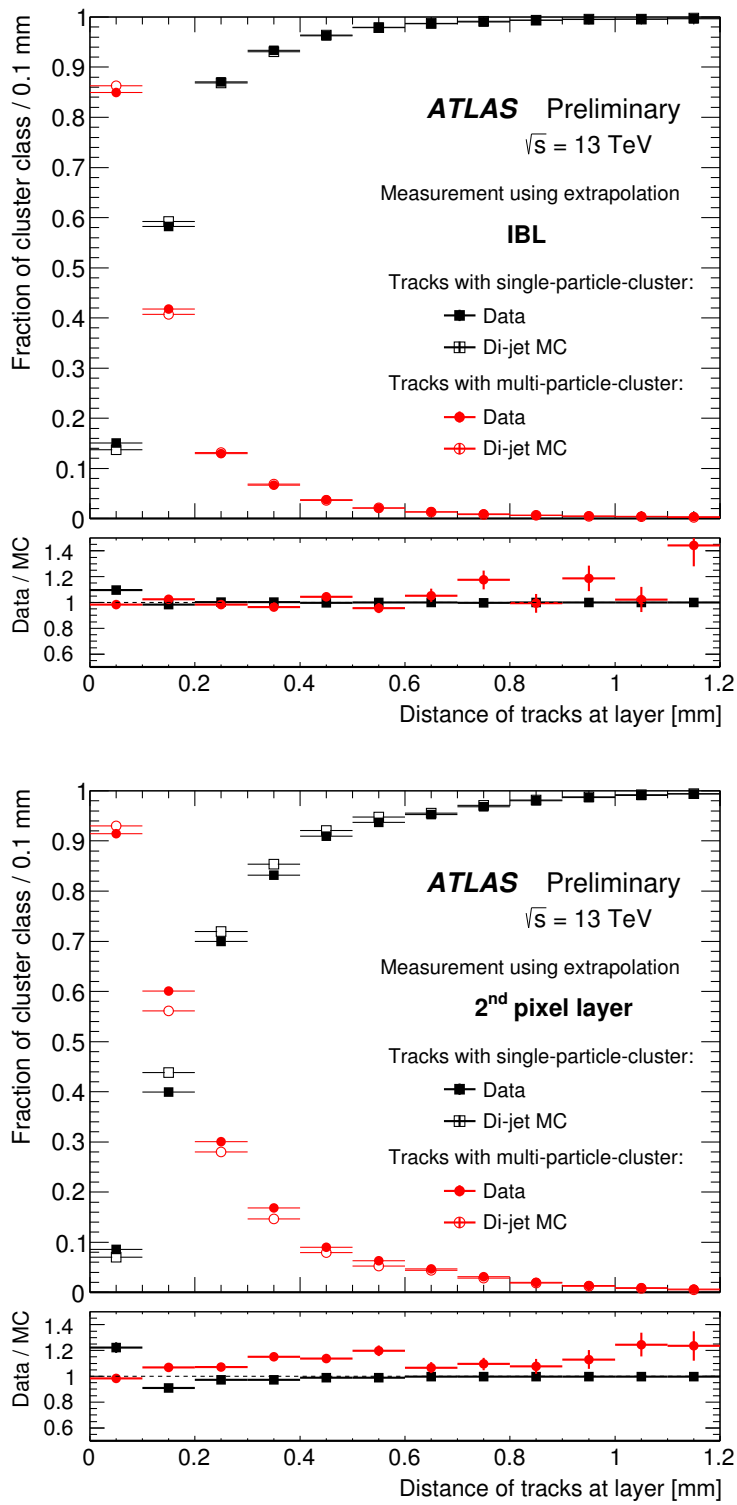


Figure 47: Fraction of cluster classes as a function of the distance between tracks for IBL (top) and 2nd pixel layer (bottom).

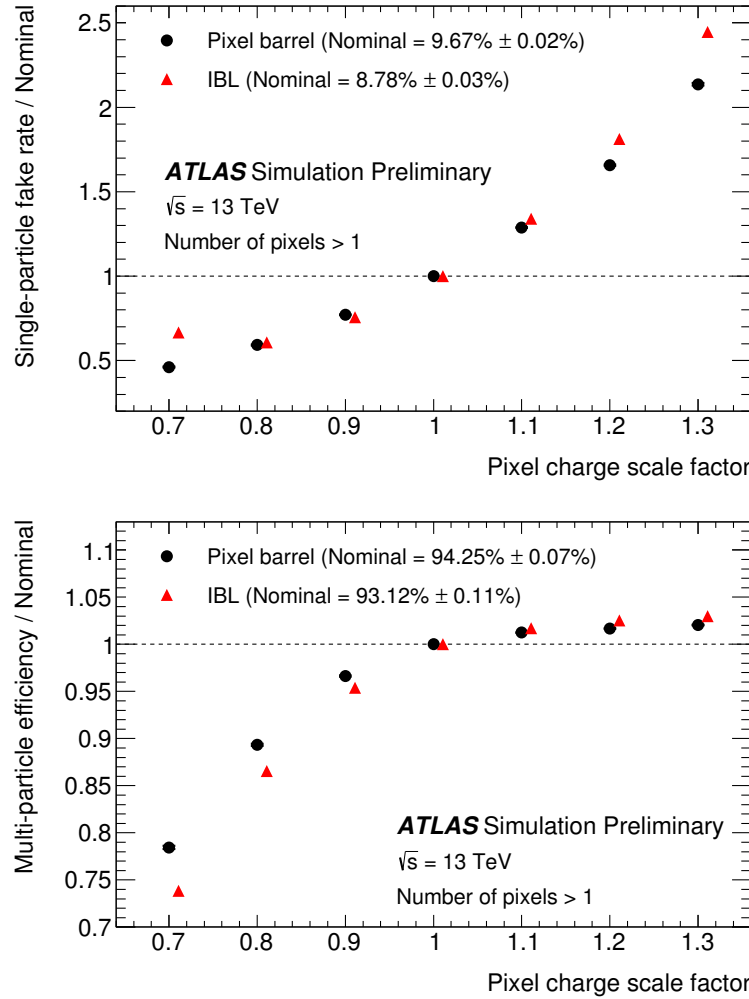


Figure 48: Performance of the pixel neural network used to identify clusters created by multiple charged particles, as a function of constant coherent scaling of the charge in each pixel in the cluster. The top figure shows the rate at which the neural network wrongly identifies clusters with one generated particle as clusters with multiple particles. The bottom figure shows the rate at which the neural network correctly identifies clusters generated by multiple particles as such.

Part IV

SEARCHING FOR SUPERSYMMETRY

This section describes an analysis of the ATLAS data carried out by the author and her analysis team. The analysis was performed on events from $p - p$ collisions provided by the LHC at $\sqrt{s}=13$ TeV. It searches for events like those described in [Section 2.2.3](#), which contain a Z boson decaying to leptons, jets, and missing transverse energy. The selection of a signal region in which to search for these events, background estimates, systematic uncertainty estimates, results, and interpretations are all discussed.

BACKGROUND PROCESSES

This analysis is fundamentally a search for Supersymmetry ([SUSY](#)) in events with two leptons whose invariant mass is consistent with a Z boson. Additional event selections are made to reduce Standard Model ([SM](#)) processes relative to potential [SUSY](#) processes, defined by simplified models discussed in [Section 2.2.3](#). [SUSY](#) events typically have large amounts of E_T^{miss} , H_T (the scalar sum of the p_T of objects in the event), and many jets. All of these features can help isolate these events from backgrounds. To understand what cuts would optimize the sensitivity of the search, it is essential to first understand what these [SM](#) backgrounds are.

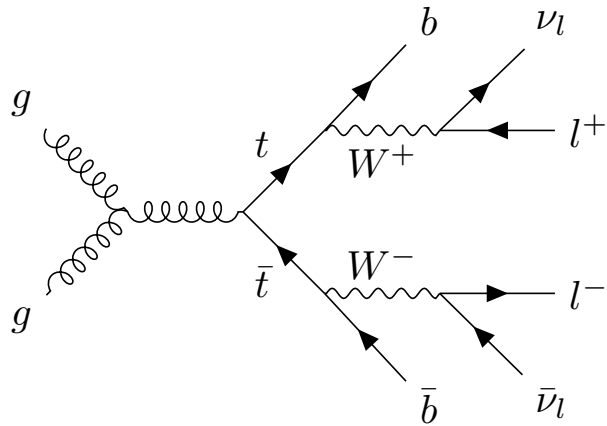


Figure 49: An example Feynman diagram of $t\bar{t}$ production and decay.

TOP-ANTITOP ($t\bar{t}$) production is the largest background for this search. [Figure 48](#) shows an example of this process, which results in many jets, leptons, and neutrinos, which are seen in the detector as E_T^{miss} . Thus, $t\bar{t}$ events naturally have high E_T^{miss} and H_T , jets, and leptons from two different W boson decays, which may coincidentally form an invariant mass consistent with a Z boson. These events are very difficult to separate from potential signals, though keeping the mass window small and increasing E_T^{miss} and H_T above the typical values for $t\bar{t}$ events helps reduce this background.

DIBOSON (VV) production is the next leading background. These events can contain real Z bosons and will peak on-Z like a signal. In addition, in events like [Figure 49](#), an additional W boson can decay to another lepton and a neutrino, providing E_T^{miss} . The pictured process can occur with associated jets, but at reduced rates, so adding a jet

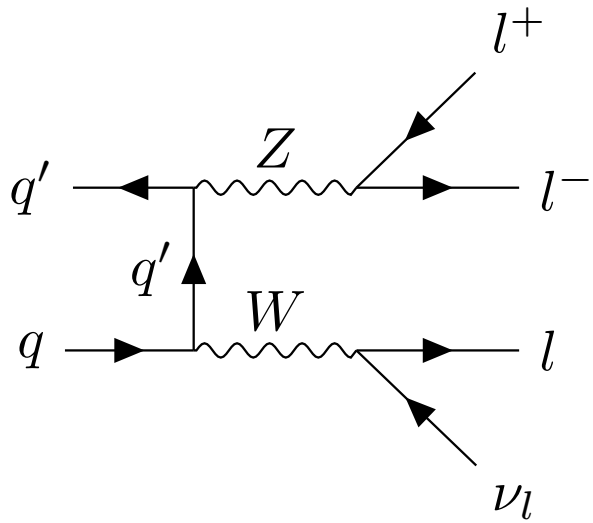


Figure 50: An example Feynman diagram of the production and decay of a WZ event.

requirement to the signal region helps reduce these events. If the W boson in this diagram instead decayed to two jets, there would be no true E_T^{miss} from a neutrino, so a E_T^{miss} cut in conjunction with a jet cut is very effective in reducing the total diboson background. A veto on a third lepton could also be used to reduce this background, but, depending on the signal model considered, this veto can also decrease signal acceptance, so it is not used in this analysis.

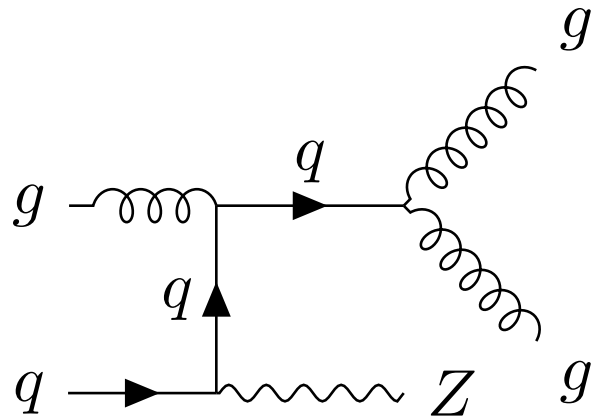


Figure 51: An example Feynman diagram of the production and decay of a $Z/\gamma^* + \text{jets}$ event.

$Z/\gamma^* + \text{jets}$ processes are very common but, as shown in Figure 50, don't produce any true E_T^{miss} or a very large number of jets. A high H_T cut helps reduce this background, but this process often occurs with associated jets, producing many events with large amounts

of hadronic activity. E_T^{miss} is the most powerful variable to reduce this background, because though events with mismeasured jets or leptons can fake E_T^{miss} , but these mismeasurements drastic enough to produce hundreds of GeV of E_T^{miss} are rare.

Other processes can contribute to the Standard Model background at lower rates. Processes similar to $Z/\gamma^* + \text{jets}$ but with a W boson instead of a Z have real E_T^{miss} from leptonic W decays, but only one lepton. However, a fake or non-prompt lepton can cause these events to look very similar to simulated signals. Additionally, there are rare processes such as $t\bar{t}$ production in association with bosons that will also be difficult to separate from signal processes.

7.1 DATA AND MONTE CARLO SAMPLES

This analysis uses data collected by the ATLAS detector from $p - p$ collisions at a center-of-mass energy of 13 TeV in 2015 and 2016, corresponding to a total luminosity of 14.7 fb^{-1} . The data collected using a combination of unprescaled single and dilepton triggers, discussed in greater detail in [Chapter 9](#). In addition, photon events are collected for use in a control region using both prescaled and unprescaled triggers, with the lowest trigger threshold at 20 GeV.

[MC](#) samples are generated for each background process that appears in the signal and validation regions. [Table 2](#) details the method used to produce each sample, and more information can be found in [Section 2.3](#). These simulated background events, in conjunction with the simulated signal discussed in [Section 2.2.3](#), are used to determine approximate sensitivities of the search and optimize signal regions and amount of data used. The background [MC](#) also provides a valuable cross-check for many of the data-driven background estimates discussed in [Chapter 11](#), and in some cases, provides the primary estimate of the background.

Table 2: Simulated background event samples used in this analysis with the corresponding matrix element and parton shower generators, cross-section order in α_s used to normalise the event yield, underlying-event tune and PDF set.

Physics process	Generator	Parton	Cross section	Tune	PDF set
		Shower			
$t\bar{t} + W$ and $t\bar{t} + Z$ [20, 56]	MG5_AMC@NLO	Pythia 8.186	NLO [38, 67]	A14	NNPDF23LO
$t\bar{t} + WW$ [20]	MG5_AMC@NLO	Pythia 8.186	LO [28]	A14	NNPDF23LO
$t\bar{t}$ [24]	POWHEG Box v2 r3026	Pythia 6.428	NNLO+NNLL [49, 50]	PERUGIA2012	NLO CT10
Single-top (Wt) [24]	POWHEG Box v2 r2856	Pythia 6.428	Approx. NNLO [61]	PERUGIA2012	NLO CT10
WW , WZ and ZZ [22]	SHERPA 2.1.1	SHERPA 2.1.1	NLO [37, 39]	SHERPA default	NLO CT10
$Z/\gamma^*(\rightarrow \ell\ell) + \text{jets}$ [21]	SHERPA 2.1.1	SHERPA 2.1.1	NNLO [40, 41]	SHERPA default	NLO CT10
$\gamma + \text{jets}$	SHERPA 2.1.1	SHERPA 2.1.1	LO [57]	SHERPA default	NLO CT10
$V(=W, Z)\gamma$ signal	SHERPA 2.1.1	LO [57]	SHERPA default	NLO CT10	
	MG5_AMC@NLO	Pythia 8.186	A14	NNPDF23LO	

8

OBJECT IDENTIFICATION AND SELECTION

This section describes the identification and selection of objects in the events of this analysis. Objects are first required to pass *baseline* selections, which are used for Overlap Removal ([OR](#)) and the calculation of E_T^{miss} , then have tighter *signal* selections applied, which define the objects considered in the final analysis of events. Definitions are presented for electrons, muons, and jets, which are all required in the Signal Region ([SR](#)) of the analysis, as well as photons, which are used in background estimation. This section refers to quality definitions described in [Chapter 5](#).

8.1 ELECTRONS

Electrons are reconstructed using the Egamma algorithm discussed in [Section 5.1](#). All electrons are required to be within $|\eta| < 2.47$, to ensure that all tracks are consistently within the tracking capability of the [ID](#). Baseline leptons are required to have $p_T > 10 \text{ GeV}$ and pass the [LHLoose](#) quality standard. Signal leptons are further required to be of [LHMedium](#) quality with [GradientLoose](#) isolation, and must have $p_T > 25 \text{ GeV}$. Additional cuts on impact parameter are made for electrons with the goal of identifying only electrons coming from the primary vertex of the event, the vertex with the highest associated p_T . These requirements, and all the other requirements made on the electrons can be seen in [Table 3](#).

Cut	Value/description
Baseline Electron	
Acceptance	$p_T > 10 \text{ GeV}, \eta^{\text{clust}} < 2.47$
Quality	LHLoose
Signal Electron	
Acceptance	$p_T > 25 \text{ GeV}, \eta^{\text{clust}} < 2.47$
Quality	LHMedium
Isolation	GradientLoose
Impact parameter	$ z_0 \sin \theta < 0.5 \text{ mm}$ $ d_0 / \sigma_{d_0} < 5$

Table 3: Summary of the electron selection criteria. The signal selection requirements are applied on top of the baseline selection.

With these requirements, the ATLAS detector is 95% efficient at identifying electrons with $p_T > 25$ GeV, which rises to 99% at $p_T > 60$ GeV[9]. Scale factors are applied to correct MC to match data efficiencies. These efficiencies are measured as a function of p_T and η , and include both electron identification efficiencies and trigger efficiencies.

8.2 MUONS

Muons are reconstructed according to the process discussed in Section 5.3. Baseline muons are required to have $p_T > 10$ GeV and $|\eta| < 2.5$, including muons that can be tracked both by the ID and the MS, and must pass a Medium quality cut. Signal muons are additionally required to have $p_T > 25$ GeV, and to have GradientLoose isolation. As with the electrons, quality cuts are made to ensure that the muon is consistent with coming from a decay from the event's primary vertex. Additionally, the muon must not be flagged isBadMuon, which reduces the number of events with very inconsistent ID and MS tracks. The full set of requirements can be seen in Table 4.

Cut	Value/description
Baseline Muon	
Acceptance	$p_T > 10$ GeV, $ \eta < 2.5$
Quality	Medium
Signal Muon	
Acceptance	$p_T > 25$ GeV, $ \eta < 2.5$
Quality	Medium
Isolation	GradientLoose
Impact parameter	$ z_0 \sin \theta < 0.5$ mm $ d_0 / \sigma_{d_0} < 3$
isBadMuon	MCP isBadMuon Flag

Table 4: Summary of the muon selection criteria. The signal selection requirements are applied on top of the baseline selection.

Muons with $p_T > 25$ GeV are identified with a 95% efficiency, which rises to 99% for muons with $p_T > 80$ GeV[23]. Including trigger and isolation requirements, these efficiencies drop to about 80% for muons with $p_T > 25$ GeV and 90% for muons with $p_T > 200$ GeV. This drop is largely the consequence of incomplete η coverage of the RPCs, discussed in Section 5.3. Scalefactors to correct the MC identification efficiencies according to data are used.

8.3 JETS

Jets are reconstructed according to [Section 5.4](#), with baseline jets using the AntiKt4EMTopo algorithm, with a minimum p_T of 20 GeV and $|\eta| < 2.8$. Signal jets increase this p_T requirement to 40 GeV and decrease their acceptance to $|\eta| < 2.5$. [JVT](#) requirements are enforced to reduce the number of jets from pile-up. The full set of requirements can be seen in [Table 5](#).

Cut	Value/description
Baseline jet	
Collection	AntiKt4EMTopo
Acceptance	$p_T > 20 \text{ GeV}, \eta < 2.8$
Signal jet	
Acceptance	$p_T > 30 \text{ GeV}, \eta < 2.5$
JVT	$ \text{JVT} > 0.59$ for jets with $p_T < 60 \text{ GeV}$ and $ \eta < 2.4$
Signal b -jet	
b -tagger Algorithm	MV2c20
Efficiency	77 %
Acceptance	$p_T > 30 \text{ GeV}, \eta < 2.5$
JVT	$ \text{JVT} > 0.59$ for jets with $p_T < 60 \text{ GeV}$ and $ \eta < 2.4$

Table 5: Summary of the jet and b -jet selection criteria. The signal selection requirements are applied on top of the baseline requirements.

Though no b -jets are required in the [SR](#) of this analysis, some Control Regions ([CRs](#)) use b -enhanced and b -vetoed regions to determine the impact of heavy flavor. These b -jets are identified using the MV2c20 algorithm at a 77% efficient working point, and are only identified for $|\eta| < 2.5$.

8.4 PHOTONS

For the nominal samples in this analysis, photon reconstruction isn't run, and photons will be identified either as jets or electrons based on their properties. As such, there is no concept of a baseline photon, because these objects are not used in either [OR](#) or E_T^{miss} calculation.

However, there is a background estimate that requires events with photons, and for this method, samples are made with photons fully reconstructed according to [Section 5.2](#). These signal photons must pass a tight selection with [FixedCutTight](#) isolation and have $p_T >$

25 GeV as well as $|\eta| < 2.37$. Photons with $1.37 < |\eta| < 1.6$ are rejected due to an discontinuity in the calorimeter which results in very large energy resolutions in this region. The full selection requirements can be seen in [Table 6](#).

Cut	Value/description
Signal Photon	
Acceptance	$p_T > 25 \text{ GeV}, \eta < 2.37$ rejecting $1.37 < \eta < 1.6$
Quality	tight
Isolation	FixedCutTight

Table 6: Summary of the photon selection criteria.

EVENT SELECTION

The goal of this analysis is to identify events resembling [Figure 13](#) in collisions in the ATLAS detector. In order to do this, a Signal Region ([SR](#)) is defined with the goal of maximizing the identification efficiency of signal-like events while minimizing [SM](#) backgrounds. However, because this analysis reinvestigates an excess of events seen in Run 1 with the ATLAS detector, the signal region was frozen and could not be reoptimized for the new, higher energy data in Run 2. The [SR](#), called [SRZ](#), was predetermined, including events with two opposite-sign, same-flavor leptons that could reconstruct a mass, $m_{\ell\ell}$, close to that of the Z boson, with the additional requirement of two jets, $E_T^{\text{miss}} > 225 \text{ GeV}$, and H_T , the scalar sum of the p_T of all jets and the leading two leptons in an event, of at least 600 GeV. Additionally, a cut on $\Delta\phi(\text{jet}_{12}, p_T^{\text{miss}})$ was made in order to reduce the number of events with high E_T^{miss} due to mismeasurement of jets.

Though this [SR](#) was fixed, the methods used to estimate its expected [SM](#) backgrounds were not. A series of Control Regions ([CRs](#)) and Validation Regions ([VRs](#)) were chosen to make these estimations possible. [CRs](#) are regions in which the collected data can be used to make an estimate of an expected background in the [SR](#), while [VRs](#) are used to confirm the efficacy of these methods. Both [CRs](#) and [VRs](#) are designed to minimize contamination from any potential [BSM](#) processes to ensure that background estimates relying on these regions don't include any potential signal.

The strategy for estimating the [FS](#) backgrounds, for example, depends on a series of [CRs](#) and [VRs](#) depicted in [Figure 51](#). One estimate, the flavor symmetry method, takes data from [CR-FS](#), a different-flavor region with slightly wider $m_{\ell\ell}$ bounds than the [SR](#), and uses these events to predict the contribution of flavor symmetric processes to [SRZ](#). An independent method called a sideband fit uses a control region [CRT](#) to measure the flavor symmetric events outside of the Z mass window, and uses [MC](#) to extrapolate inside the Z mass window to [SRZ](#). Then, both methods are validated at lower E_T^{miss} with an otherwise identical series of regions, with [VRS](#) corresponding to [SRZ](#), [VRT](#) corresponding to [CRT](#), and [VR-FS](#) corresponding to [CR-FS](#).

Each background estimation requires its own set of these regions, and the full list of regions used in this analysis can be seen in [Table 7](#). In addition to the Flavor Symmetric ([FS](#)) regions described above, there is one more [CR](#), [CR- \$\gamma\$](#) , which is a photon region used to predict the number of $Z/\gamma^* + \text{jets}$ events, a process described in [Section 10.2](#). Additional [VRs](#), [VR-ZZ](#), [VR-WZ](#), and [VR-3L](#), are intro-

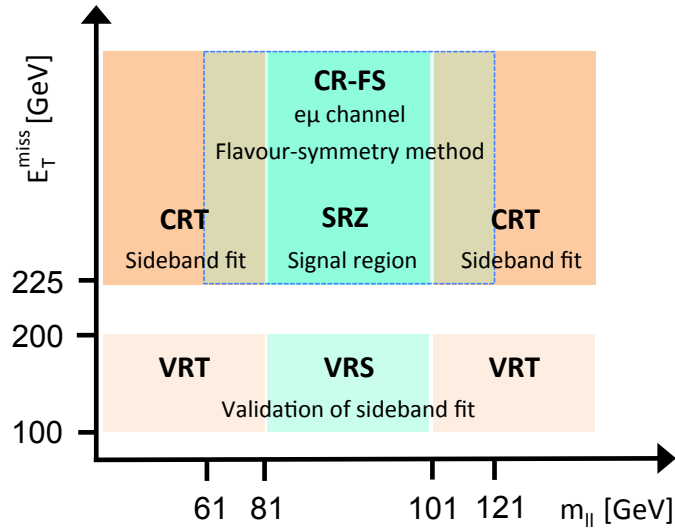


Figure 52: Schematic diagrams of the control, validation and signal regions for the on-shell Z (top) and edge (bottom) searches. For the on-shell Z search the various regions are shown in the $m_{\ell\ell} - E_T^{\text{miss}}$ plane, whereas in the case of the edge search the signal and validation regions are depicted in the $H_T - E_T^{\text{miss}}$ plane.

duced in order to validate the backgrounds taken directly from MC. There are several additional regions used, for example, in the estimation of the fakes and $Z/\gamma^* + \text{jets}$ backgrounds, that are defined in their respective sections.

9.1 TRIGGER STRATEGY

In order to collect data for the analysis, triggers must be chosen that provide good efficiency in each of the SR, VR, and CRs. This analysis primarily depends on triggers on leptons, which are required in nearly every region. To simplify the application of trigger scalefactors, which correct MC yields for a given trigger to match the data efficiencies, events are broken down into a series of kinematic ranges, each with a designated trigger. These regions can be seen in Table 8.

In kinematic regions where single lepton triggers are fully efficient, they are preferentially used. In lower- p_T ranges, dilepton triggers are used, targeting either ee , $\mu\mu$, or $e\mu$ events. Electron triggers are selected over muon triggers when possible because they have higher efficiencies in most cases.

In CR- γ , there are no leptons, so an alternate trigger strategy must be used. Section 10.2.1 describes this triggering scheme, which includes a combination of prescaled and unprescaled photon triggers to allow for the collection of low- p_T $\gamma + \text{jets}$ events.

Table 7: Overview of all signal, control and validation regions used in the on-shell Z search. More details are given in the text. The flavour combination of the dilepton pair is denoted as either “SF” for same-flavour or “DF” for different flavour. All regions require at least two leptons, unless otherwise indicated. In the case of CR γ , VR-WZ, VR-ZZ, and VR-3L the number of leptons, rather than a specific flavour configuration, is indicated. The main requirements that distinguish the control and validation regions from the signal region are indicated in bold. Most of the kinematic quantities used to define these regions are discussed in the text. The quantity $m_T(\ell_3, E_T^{\text{miss}})$ indicates the transverse mass formed by the E_T^{miss} and the lepton which is not assigned to either of the Z-decay leptons.

On-shell Z regions	E_T^{miss} [GeV]	H_T [GeV]	n_{jets}	$m_{\ell\ell}$ [GeV]	SF/DF	$\Delta\phi(\text{jet}_{12}, p_T^{\text{miss}})$	$m_T(\ell_3, E_T^{\text{miss}})$ [GeV]	$n_{\text{b-jets}}$
Signal region								
SRZ	> 225	> 600	≥ 2	$81 < m_{\ell\ell} < 101$	SF	> 0.4	—	—
Control regions								
CRZ	< 60	> 600	≥ 2	$81 < m_{\ell\ell} < 101$	SF	> 0.4	—	—
CR-FS	> 225	> 600	≥ 2	61 < $m_{\ell\ell}$ < 121	DF	> 0.4	—	—
CRT	> 225	> 600	≥ 2	> 40 , $m_{\ell\ell} \notin [81, 101]$	SF	> 0.4	—	—
CR γ	—	> 600	≥ 2	—	$0\ell, 1\gamma$	—	—	—
Validation regions								
VRZ	< 225	> 600	≥ 2	$81 < m_{\ell\ell} < 101$	SF	> 0.4	—	—
VRT	100–200	> 600	≥ 2	> 40 , $m_{\ell\ell} \notin [81, 101]$	SF	> 0.4	—	—
VRS	100–200	> 600	≥ 2	$81 < m_{\ell\ell} < 101$	SF	> 0.4	—	—
VR-FS	100–200	> 600	≥ 2	61 < $m_{\ell\ell}$ < 121	DF	> 0.4	—	—
VR-WZ	100–200	—	—	—	3ℓ	—	< 100	0
VR-ZZ	< 100	—	—	—	4ℓ	—	—	0
VR-3L	60–100	> 200	≥ 2	$81 < m_{\ell\ell} < 101$	3ℓ	> 0.4	—	—

Lepton p_T	Trigger in 2015	Trigger in 2016
Di-electron channel		
$p_T(e_1) > 65 \text{ GeV}$	HLT_e60_lhmedium	HLT_e60_lhmedium_nod0
$p_T(e_1) \leq 65 \text{ GeV}$	HLT_2e17_lhloose	HLT_2e17_lhvloose_nod0
Di-muon channel		
$p_T(\mu_1) > 52.5 \text{ GeV}$	HLT_mu50	HLT_mu50
$p_T(\mu_1) \leq 52.5 \text{ GeV}$	HLT_mu24_mu8noL1	HLT_2mu14_nomucomb
Electron-muon channel		
$p_T(e) > 65 \text{ GeV}$	HLT_e60_lhmedium	HLT_e60_lhmedium_nod0
$p_T(e) \leq 65 \text{ GeV}$ and $p_T(\mu) > 52.5 \text{ GeV}$	HLT_mu50	HLT_mu50
$p_T(e) \leq 65 \text{ GeV}$ and $p_T(\mu) \leq 52.5 \text{ GeV}$ and $p_T(e) < p_T(\mu)$	HLT_e7_lhmedium_mu24	HLT_e7_lhmedium_nod0_mu24
$p_T(e) \leq 65 \text{ GeV}$ and $p_T(\mu) \leq 52.5 \text{ GeV}$ and $p_T(\mu) < p_T(e)$	HLT_e17_lhloose_mu14	HLT_e17_lhloose_nod0_mu14

Table 8: Lepton trigger requirements used for the analysis in different regions of lepton- p_T phase space.

9.2 SIGNAL EFFICIENCY AND CONTAMINATION

Using the simplified models discussed in Section 2.2.3, the contributions of potential signals in these regions can be studied. In the SR, the goal is to include as much of the potential signal as possible, while excluding as much SM background as possible. Figure 52 shows the acceptance and efficiency for the simplified models at different mass points. Acceptance is defined as the fraction of signal events that produce signatures that kinematically match the SR, while the efficiency is the fraction of these events expected to be correctly identified by the ATLAS detector.

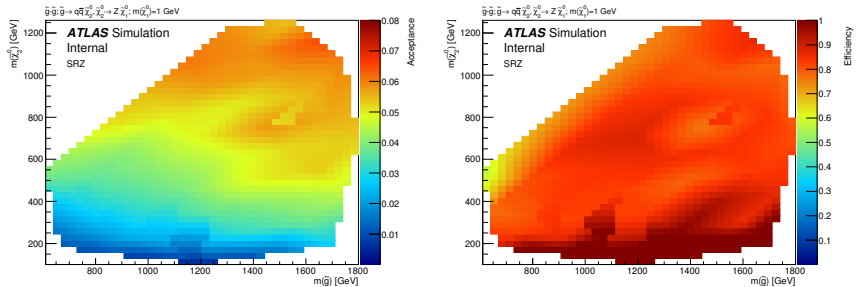


Figure 53: Signal region acceptance (left) and efficiency (right) in SRZ for the simplified model with gluino pair production with $\tilde{\chi}_2^0$ decays to $\tilde{\chi}_1^0$ and an on-shell Z boson with 1GeV neutralino LSP. Acceptance is calculated by applying the signal-region kinematic requirements to truth objects in MC, which do not suffer from identification inefficiencies or measurement resolutions.

A similar test is done for the main CRs and VRs which estimates their susceptibility to signal contamination. Figures 53 and 54 show the fraction of events in these regions expected to come from signal

for different points on the simplified model's mass grid. Contamination is highest in VRS, but only rises above 10% for grid points that have already been excluded by past analyses, and so are not important targets for this search.

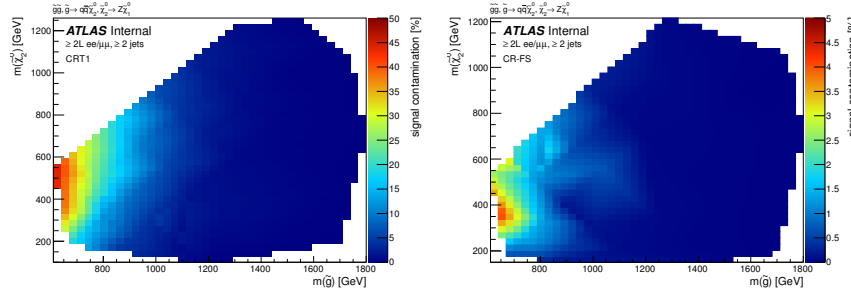


Figure 54: Expected signal contamination in CRT (left) and CR-FS (right) for the signal model with gluino pair production, where the gluinos decay to quarks and a neutralino, with the neutralino subsequently decaying to a Z boson and a 1GeV neutralino LSP.

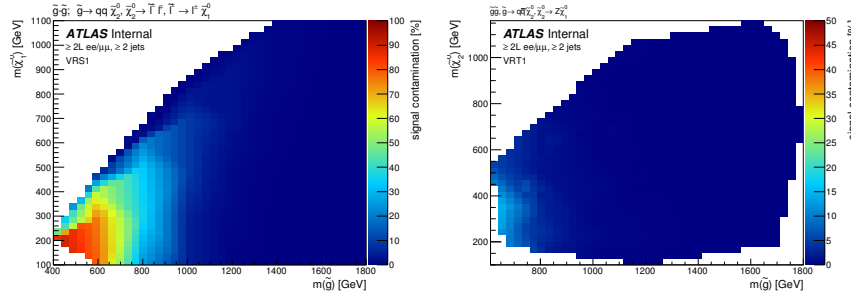


Figure 55: Expected signal contamination in VRS (left) and VRT (right) for the signal model with gluino pair production, where the gluinos decay to quarks and a neutralino, with the neutralino subsequently decaying to a Z boson and a 1GeV neutralino LSP.

BACKGROUND ESTIMATION

This analysis requires two leptons that reconstruct to a Z mass, jets, E_T^{miss} , and H_T . Any standard model processes that produce this signature will appear as a background to the search. The most important task of the analysis is to identify and estimate these backgrounds, so that any excess of events appearing on top of the standard model background can be identified. The main backgrounds for this analysis are described in [Chapter 7](#). The largest background is from flavor symmetric processes, with smaller contributions coming from diboson processes, $Z/\gamma^* + \text{jets}$, rare top processes, and fake and non-prompt leptons.

10.1 FLAVOR SYMMETRIC PROCESSES

Flavor Symmetric ([FS](#)) backgrounds include any processes that produce pairs of leptons with uncorrelated flavor in the final state. In this analysis, the largest contribution comes from $t\bar{t}$, with additional events from processes like WW and $Z \rightarrow \tau\tau$. In these processes, each lepton comes from a different decay. Unlike a $Z \rightarrow \ell\ell$ decay then, these leptons' flavors are completely independent.

10.1.1 Flavor Symmetry Method

As a consequence of the independence of the lepton flavors, any [FS](#) process should produce ee , $\mu\mu$, and $e\mu$ events in a 1:1:2 ratio. This ratio is taken advantage of in the flavor symmetry method by measuring $e\mu$ events in data and using them to predict the contribution of these processes in the ee and $\mu\mu$ channels. [17]

To estimate the number of events in SRZ, a control region called CR-FS is used. Both regions are defined in [Table 7](#). CR-FS is very similar to SRZ with two changes: it requires different-flavor leptons instead of the same-flavor leptons required by SRZ, and the $m_{\ell\ell}$ range it covers has been expanded by a factor of three, now ranging from 61 to 121 GeV. The expansion of the $m_{\ell\ell}$ window is done to increase the number of events in the control region, thus lowering the statistical uncertainty of the prediction¹.

¹ Though this statistical uncertainty is no longer dominant for the analysis, the method was developed for a smaller dataset for which this expansion dramatically decreased the total uncertainty on the background prediction. [6] Because of previous excesses seen, the signal region was not reoptimized for the larger dataset used in this search,

This control region is expected to be about 95% pure in **FS** processes, with most of the remaining events coming from fake or non-prompt leptons. The **FS** portion is made up primarily of $t\bar{t}$ ($\sim 80\%$), with additional contributions from Wt ($\sim 10\%$), WW ($\sim 10\%$), and $< 1\% Z \rightarrow \tau\tau$.

After the number of data events are measured in CR-FS, correction factors are applied to account for trigger efficiencies, selection efficiencies, the $m_{\ell\ell}$ expansion, and the purity of the control region. Combining these factors, the estimate for number of events in the ee and $\mu\mu$ channels is as follows:

$$N_{ee}^{\text{est}} = \frac{1}{2} \cdot f_{\text{FS}} \cdot f_{Z\text{-mass}} \cdot \sum_{\substack{N_{e\mu}^{\text{data}} \\ k_e(p_T, \eta) \cdot \alpha(p_T^{\ell_1}, \eta^{\ell_1})}} N_{e\mu}^{\text{data}}, \quad (30)$$

$$N_{\mu\mu}^{\text{est}} = \frac{1}{2} \cdot f_{\text{FS}} \cdot f_{Z\text{-mass}} \cdot \sum_{\substack{N_{e\mu}^{\text{data}} \\ k_\mu(p_T, \eta) \cdot \alpha(p_T^{\ell_1}, \eta^{\ell_1})}} N_{e\mu}^{\text{data}}, \quad (31)$$

where $N_{e\mu}^{\text{data}}$ is the number of data events observed in CR-FS, f_{FS} is the **FS** purity in CR-FS, $f_{Z\text{-mass}}$ is the fraction of events in the widened $m_{\ell\ell}$ range expected to be in the on-Z range (taken from $t\bar{t}$ **MC**), $k_e(p_T, \eta)$ and $k_\mu(p_T, \eta)$ are relative selection efficiencies for electrons and muons, calculated in bins of p_T and η of the lepton to be replaced, and $\alpha(p_T, \eta)$ accounts for the different trigger efficiencies for events in each channel, binned based on the kinematics of the leading lepton. These k and α factors are calculated from data in an inclusive on-Z selection ($81 < m_{\ell\ell}/\text{GeV} < 101$, ≥ 2 jets), according to:

$$k_e(p_T, \eta) = \sqrt{\frac{N_{ee}^{\text{meas}}}{N_{\mu\mu}^{\text{meas}}}} \quad (32)$$

$$k_\mu(p_T, \eta) = \sqrt{\frac{N_{\mu\mu}^{\text{meas}}}{N_{ee}^{\text{meas}}}} \quad (33)$$

$$\alpha(p_T, \eta) = \frac{\sqrt{\epsilon_{ee}^{\text{trig}}(p_T, \eta) \times \epsilon_{\mu\mu}^{\text{trig}}(p_T, \eta)}}{\epsilon_{e\mu}^{\text{trig}}(p_T, \eta)} \quad (34)$$

where $\epsilon_{ee/\mu\mu}^{\text{trig}}$ is the trigger efficiency² and $N_{ee/\mu\mu}^{\text{meas}}$ is the number of $ee/\mu\mu$ events in the inclusive on-Z region described above. Here $k_e(p_T, \eta)$

but in future iterations of this analysis, the signal region will likely have tighter cuts, making this decreased statistical uncertainty significant once again.

² This efficiency is defined by taking all events in the inclusive on-Z selection mentioned above and determining the fraction that passes the relevant trigger requirement defined by [Table 8](#). Because the offline selection made on these events already has some trigger dependence, this calculation of efficiency could be slightly biased. This effect is considered in [Section 11.1.1](#), and the uncertainty applied to the estimate as a result is described.

Region	ee prediction	$\mu\mu$ prediction	combined prediction
SRZ	16.50 ± 2.11	16.67 ± 2.04	33.16 ± 3.94
VRS	49.70 ± 4.61	49.60 ± 4.56	99.31 ± 8.47

Table 9: Yields in signal and validation regions for the flavor symmetric background. Errors include statistical uncertainty, uncertainty from MC closure, uncertainty from the k and α factors, uncertainty due to deriving triggers efficiencies from a DAOD, and uncertainty on the MC shape used to correct for the $m_{\ell\ell}$ expansion.

$= 1/k_\mu(p_T, \eta)$, and this k factor is calculated separately for leading and sub-leading leptons, and the appropriate k value is selected based on which of the leptons is to be replaced.

Electron, muon, and trigger efficiencies are all quite close to one, and as a consequence, these correction factors are typically within 10% of unity, except in the region $|\eta| < 0.1$ where, because of the lack of coverage of the muon spectrometer, they are up to 50% from unity.

The estimate is corrected for contamination of non-[FS](#) backgrounds in CR-[FS](#). A scaling factor is determined by subtracting these backgrounds from the number of $e\mu$ events measured in CR-[FS](#), then determining the fraction of the original data events that this pure-[FS](#) number represents. The estimate for the non-[FS](#) backgrounds is taken from [MC](#) for all processes except fakes, which are predicted from data using the matrix method described in [Section 10.3](#).

A prediction is made both for the signal region, SRZ, and the lower- E_T^{miss} validation region, VRS. This process is performed separately for the two data taking periods, 2015 and 2016, because of the changing triggers and conditions. The results are then summed together, as shown in [Table 9](#). The uncertainties in this table are discussed in [Section 11.1.1](#).

10.1.2 Sideband Fit Method

As a crosscheck to the flavor symmetry method, a [MC](#)-based method is used. This method is called a *sideband fit*, and it begins with a [MC](#) estimate of the signal region across an $m_{\ell\ell}$ range that includes all values above 40 GeV. This region, excluding the on-Z range that makes up the [SR](#), is used as a control region, defined as CRT in [Table 7](#).

The total data yield is measured in CRT, and the [MC](#) is fit to match this yield with one normalization factor which scales the overall $t\bar{t}$ background. As mentioned in the previous section, $t\bar{t}$ is the dominant [FS](#) background, making up about 80% of the total events. All other backgrounds contributing to this control region are constrained by their uncertainties, which are used as nuisance parameters in the fit. The normalization factor from this fit is then applied to the $t\bar{t}$ [MC](#)

yield in the **SR**, and combined with the **MC** predictions of the other **FS** processes in the **SR** to give a final estimate of this background. The results of the fit can be seen in [Table 10](#).

The method is repeated in VRS to validate the method. The normalization factors, listed in [Table 11](#), are significantly different for the two regions. This is expected because there is a known problem in which the $t\bar{t}$ **MC** over-predicts the high- E_T^{miss} tail. This effect can be seen in a data-**MC** comparison in [Figure 55](#). This is likely due to a mismodeling of the top quark p_T distribution, which does not match the spectrum seen in data [19, 35]. However, this method corrects for this mismodeling by performing fits in regions very kinematically similar to the signal region.

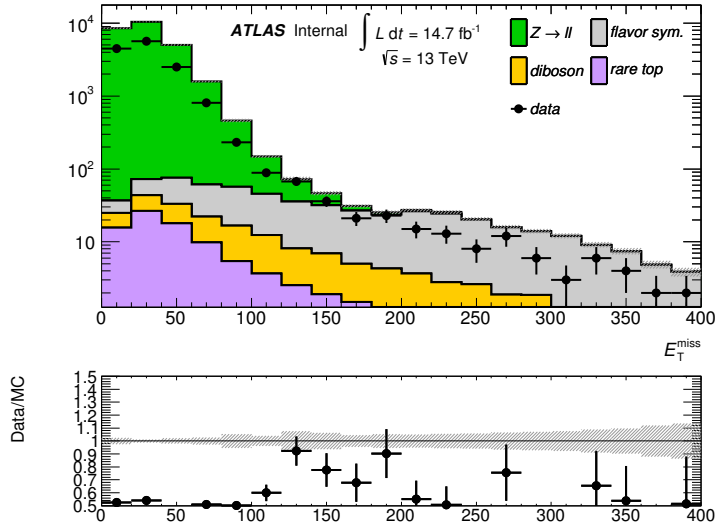


[Figure 56](#): Comparison of data and **MC** in a selection like SRZ, without the E_T^{miss} cut.

This method is extremely effective as a crosscheck because it uses a completely independent dataset from the flavor symmetry method, and the two methods have very little overlap in dependence on **MC**. They produce consistent results in both SRZ and VRS, as shown in [Table 12](#).

10.2 $Z / \gamma^* + \text{jets}$ BACKGROUND

The $Z / \gamma^* + \text{jets}$ background is mainly produced by a process called Drell-Yan in which annihilating quark/anti-quark pairs produce a Z boson or a virtual photon. These bosons then decay to two leptons, which, in the case of the Z boson, naturally appear in the Z -mass window. The boson typically recoils off a hadronic system, which can satisfy the jet and H_T requirement in SRZ. However, this process rarely produces real E_T^{miss} (though occasionally neutrinos do appear in its hadronic decays), so most events with large amounts of E_T^{miss} are

channel	$ee/\mu\mu$ CRT	$ee/\mu\mu$ SRZ	$ee/\mu\mu$ SRZ	$ee/\mu\mu$ SRZ
Observed events	273	60	35	25
Fitted bkg events	272.76 ± 16.88	49.33 ± 8.04	27.09 ± 4.73	22.70 ± 3.80
Fitted flavour symmetry events	236.96 ± 21.66	28.96 ± 7.47	16.41 ± 4.33	12.55 ± 3.29
Fitted WZ/ZZ events	4.03 ± 1.13	14.27 ± 4.45	7.81 ± 2.45	6.46 ± 2.07
Fitted SHERPA Z/γ^* + jets events	1.95 ± 0.14	0.00 ± 0.00	0.00 ± 0.00	0.00 ± 0.00
Data-driven Z/γ^* + jets (γ + jets) events	0.00 ± 0.00	3.10 ± 2.25	$1.02^{+1.25}_{-1.02}$	2.08 ± 1.38
Fitted rare top events	4.04 ± 1.04	2.90 ± 0.76	1.39 ± 0.38	1.50 ± 0.40
Data-driven fake lepton events	25.78 ± 14.26	$0.10^{+0.18}_{-0.10}$	0.46 ± 0.45	0.10 ± 0.01
MC exp. SM events	366.71	61.01	33.73	27.74
MC exp. flavour symmetry events	331.32	40.72	23.09	17.63
MC exp. WZ/ZZ events	4.02	14.20	7.77	6.43
MC exp. SHERPA Z/γ^* + jets events	1.94	0.00	0.00	0.00
Data-driven exp. Z/γ^* + jets (γ + jets) events	0.00	3.10	1.02	2.08
MC exp. rare top events	4.04	2.89	1.39	1.50
Data-driven exp. fake lepton events	25.39	0.10	0.46	0.10

Table 10: Background fit results from the sideband fit method. The $t\bar{t}$ MC's normalization is taken as a free parameter in the fit to data in CRT, then that normalization factor is applied in SRZ. The results are shown here both divided between the ee and $\mu\mu$ channels and summed together. All other backgrounds are taken from MC in CRT, while in SRZ, the Z/γ^* + jets contribution is taken from the γ + jets method. The uncertainties quoted include both statistical and systematic components.

Fit region	$t\bar{t}$ normalization
CRT	0.64 ± 0.18
VRT	0.80 ± 0.09

Table 11: Summary of the $t\bar{t}$ normalization factors calculated by the sideband fit to CRT and VRT for the 2015+2016 data.

Region	Flavour-symmetry	Sideband fit
SRZ	33 ± 4	29 ± 7
VR-S	99 ± 8	92 ± 25

Table 12: Comparison of [FS](#) background predictions from the nominal method, the flavor symmetry method, and the cross-check, the sideband fit method. Uncertainties include statistical and systematic uncertainties in both cases.

the result of extreme mismeasurement. Because SRZ cuts on the very high E_T^{miss} tails of a Z distribution, a small change in the assumptions about jet resolution or energy scale in [MC](#) can drastically change the prediction, and a low $Z/\gamma^* + \text{jets}$ prediction can result in a signal-like peak appearing in the final result.

Because of this volatility in the [MC](#) prediction in these high E_T^{miss} tails, a data-driven method is used to estimate this background. The method uses $\gamma + \text{jets}$ events which, like the $Z/\gamma^* + \text{jets}$ events, contain one boson recoiling against a hadronic system. These $\gamma + \text{jets}$ events are then corrected for the kinematic differences between γ and Zs [5, 34]. The sample of $\gamma + \text{jets}$ events is taken from CR- γ , defined in [Table 7](#). This region is similar to the SRZ selection without the E_T^{miss} requirement, but it vetoes events with leptons and requires at least one photon. Additionally, the $\Delta\phi(\text{jet}_{12}, p_T^{\text{miss}})$ cut in SRZ, which is designed to reduce the background from mismeasured jets, is removed for this region because of its unpredictability at very low values of E_T^{miss} , when the angle of the E_T^{miss} is much less meaningful.

Despite their similarities, there are many theoretical differences between γ and Z events. The massive Z boson recoils differently against a jet system than the massless photon. Another consequence of its masslessness is that photons cannot appear in decays with no jets because such a decay would always violate conservation of energy in some frame. As a consequence, many kinematic variables have different shapes between the two samples. [Figure 56](#) shows a [MC](#) comparison of boson p_T between γ and Z events, demonstrating the shape differences between the two processes.

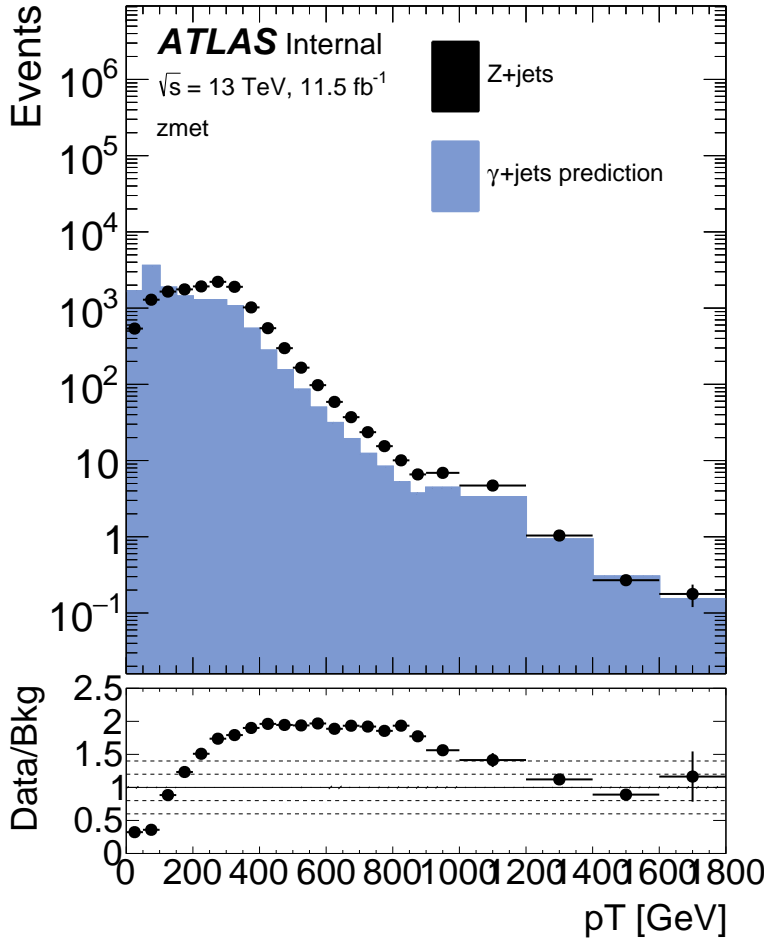


Figure 57: MC comparison of boson p_T in a selection of photon and $Z \rightarrow \ell\ell$ events with $H_T > 600$ GeV.

The most significant experimental difference between Z and γ events is that Z bosons rapidly decay, in the case of this analysis, to two leptons, which are then observed by the ATLAS detector. In contrast, the photon is stable, and can be directly detected by ATLAS. This means that the reconstructed Z boson and the directly observed photon have very different energy resolutions, which can result in different amounts of E_T^{miss} in the two events.

Ultimately, the goal of this method is to predict the E_T^{miss} distribution of the $Z+\text{jets}$ background. These differences between $Z+\text{jet}$ and $\gamma+\text{jet}$ events can be broken down into two categories: differences which affect the jet energy and measurement, and differences which affect the boson energy and measurement. The differences in the hadronic system are simpler, and mostly consist of different numbers and energies of jets between the two samples, which can be accounted for via reweighting in a variable that's representative of the total energy scale of the event. The differences in the bosons are more complex, and require the application of smearing functions based on the

different observed objects. Together these corrections allow for complete modeling of the $Z/\gamma^* + \text{jets } E_T^{\text{miss}}$ spectrum with $\gamma+\text{jet}$ events.

10.2.1 Photon and Z Event Selection

The baseline photon events come from an inclusive CR with no E_T^{miss} cut, a lepton veto, and the requirement of at least one photon, which is called CR- γ and defined in Table 7. This selection is very pure in $\gamma+\text{jet}$ events, but some $V\gamma$ events are also included, which can include real E_T^{miss} . These backgrounds are subtracted off at the end off the estimation procedure.

The triggering scheme for these events is more complicated than in other regions because the lowest unprescaled photon trigger requires a photon p_T of at least 120 (140) GeV in 2015 (2016) datataking, but the method requires events with much lower p_T to predict the full Z -boson p_T spectrum. To accomplish this, the lower- p_T photons are broken down into small p_T ranges with a different prescaled trigger required in each range, listed in Table 13. The events in each selection are then weighted by the prescale value of the trigger used to reconstruct a smooth p_T spectrum.

These γ events can then be compared to baseline $Z \rightarrow \ell\ell$ events with a similar selection. These events have the same dilepton requirements as SRZ, without the $m_{\ell\ell}$ cut. They also have no E_T^{miss} cut, but like the photons, are required to have $H_T > 600$ GeV as in SRZ.

10.2.2 Smearing of Photon Events

While $Z+\text{jet}$ events are measured as a pair of leptons recoiling against a hadronic system, $\gamma+\text{jet}$ events are measured only as one object recoiling against jets. In addition, detector resolution is different for electrons, muons, and photons. The impact of these differences must be corrected for in $\gamma+\text{jet}$ events in order for them to accurately predict the E_T^{miss} distribution of the Z s. Luckily, in most cases, the resolution of the photon's p_T is better the Z boson's, so the photon events can be smeared to emulate the Z s.

To isolate mismeasurement of boson p_T , this method uses $E_{T,\parallel}^{\text{miss}}$, the E_T^{miss} projection on an axis defined by the momentum of the boson. Figure 57 shows the $E_{T,\parallel}^{\text{miss}}$ distribution in MC for the two samples, and demonstrates the discrepancies between them. The core of the photon distribution somewhat similar to the $Z \rightarrow ee$ distribution because, in the high- p_T limit, measurements of both photons and electrons are primarily taken from the electromagnetic calorimeter and should have similar resolutions. For muons, which rely only on tracks to determine p_T , the resolution becomes very large at high p_T values where the tracks are nearly straight. As a consequence, the resolutions for photon and $Z \rightarrow \mu\mu$ events are very different.

p_T Range [GeV]	Trigger Name
2015 Data-Taking	
$37 < p_T < 45$	HLT_g35_loose_L1EM15
$45 < p_T < 50$	HLT_g40_loose_L1EM15
$50 < p_T < 55$	HLT_g45_loose_L1EM15
$55 < p_T < 125$	HLT_g50_loose_L1EM15
$p_T > 125$	HLT_g120_loose_L1EM15
2016 Data-Taking	
$25 < p_T < 30$	HLT_g20_loose_L1EM12
$30 < p_T < 40$	HLT_g25_loose_L1EM12
$40 < p_T < 45$	HLT_g35_loose_L1EM12
$45 < p_T < 50$	HLT_g40_loose_L1EM12
$50 < p_T < 55$	HLT_g45_loose_L1EM12
$55 < p_T < 65$	HLT_g50_loose_L1EM12
$65 < p_T < 75$	HLT_g60_loose_L1EM12
$75 < p_T < 85$	HLT_g70_loose_L1EM12
$85 < p_T < 105$	HLT_g80_loose_L1EM12
$105 < p_T < 145$	HLT_g100_loose_L1EM12
$p_T > 145$	HLT_g140_loose_L1EM12

Table 13: List of triggers used to collect photon events in 2015 and 2016 data-taking.

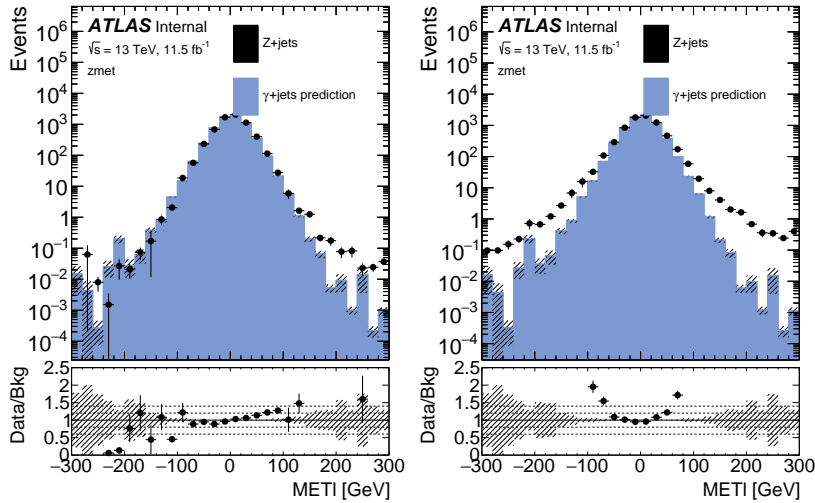


Figure 58: $E_{T,\parallel}^{\text{miss}}$ distributions in MC for $Z + \text{jets}$ and $\gamma + \text{jets}$ in an inclusive region with $H_T > 600 \text{ GeV}$.

A function to smear photon events is derived from the deconvolution of the photon and lepton response functions, taken from 1-jet CRs with no H_T cut, which are otherwise identical to the baseline Z and γ selections. In these regions, events are binned in boson p_T , and in each bin, a $E_{T,\parallel}^{\text{miss}}$ distribution is made. The smearing function is derived for each bin via the deconvolution of the $Z/\gamma^* + \text{jets}$ and $\gamma + \text{jets}$ distributions.

Next, for each photon event, the smearing function matching the event's photon p_T is sampled, yielding a smearing factor Δp_T . The photon's p_T is then adjusted according to

$$p_T^{\gamma'} = p_T^\gamma + \Delta p_T \quad (35)$$

and the corresponding change in E_T^{miss} is made,

$$E_{T,\parallel}^{\text{miss}'} = E_{T,\parallel}^{\text{miss}} - \Delta p_T. \quad (36)$$

The nominal smearing function is taken from MC in order to remove contamination from other backgrounds, and the resulting $E_{T,\parallel}^{\text{miss}}$ distributions can be seen in Figure 58. Though there is a small amount of over-smearing in the negative tail, the improvement in agreement between the distributions is clear.

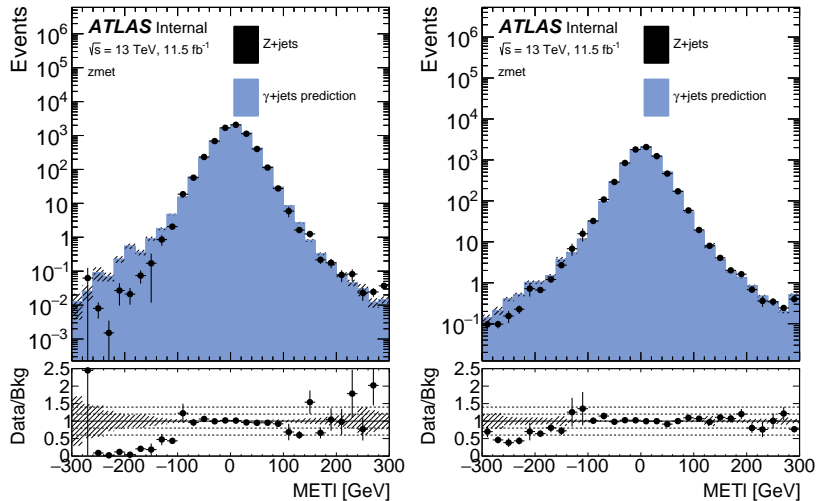


Figure 59: $E_{T,\parallel}^{\text{miss}}$ distributions in MC for $Z + \text{jets}$ and $\gamma + \text{jets}$ in an inclusive region with $H_T > 600$ GeV after the smearing procedure has been performed. These distributions have also been p_T reweighted, as described in Section 10.2.3.

10.2.3 p_T Reweighting of Photon Events

Next, the photon events are reweighted to match the boson p_T of the Z events. This is accomplished by making histograms of boson p_T

for γ and Z events, similar to that in Figure 56, and with binning identical to that used in Section 10.2.2. A reweighting factor $f(p_T)$ is then calculated in each bin, according to

$$f(x) = \frac{N_{Z/\gamma^*+\text{jets}}(x)}{N_{\gamma+\text{jets}}^i(x)} \quad (37)$$

in MC, and in data according to

$$f(x) = \frac{N_{\text{data}}(x) - N_{t\bar{t}}(x) - N_{VV}(x)}{N_{\gamma+\text{jets data}}(x)} \quad (38)$$

where the contamination from other backgrounds is taken from MC and subtracted from the Z selection. The resulting reweighting factors can be seen in Figure 59 and are calculated independently for ee and $\mu\mu$ events.

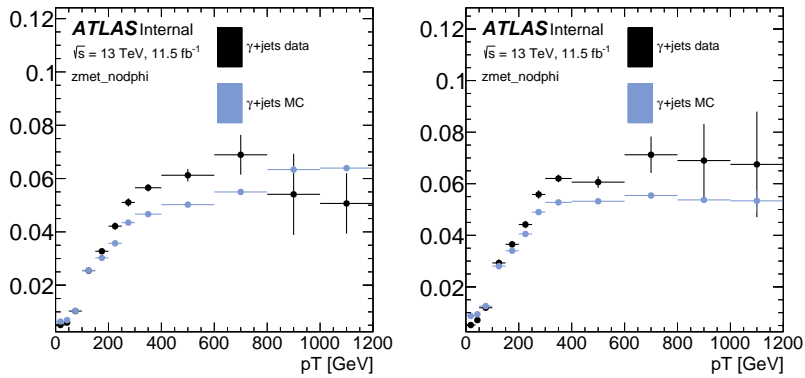


Figure 60: Photon reweighting factors for the ee (left) and $\mu\mu$ (right) channels derived from data and MC.

This reweighting, though it is performed on the boson p_T , primarily serves to produce more similar jet distributions between the γ and Z samples. Because, excluding E_T^{miss} contributions, the boson p_T must match the energy of the jet system off which it recoils, these two variables are closely tied. Once the two samples have similar amounts of hadronic energy, the E_T^{miss} contribution from mismeasurement of jet energy should also be similar.

Together, the boson smearing and p_T reweighting produce a E_T^{miss} spectrum in the modified photon events that closely match that of the Z events. Figures 60 and 61 show the comparison of the E_T^{miss} distributions before any alteration, with only p_T reweighting, and after the smearing and reweighting, demonstrating the impact of each step. Once the E_T^{miss} distribution is well described, the $\Delta\phi(\text{jet}_{12}, p_T^{\text{miss}})$ can be applied.

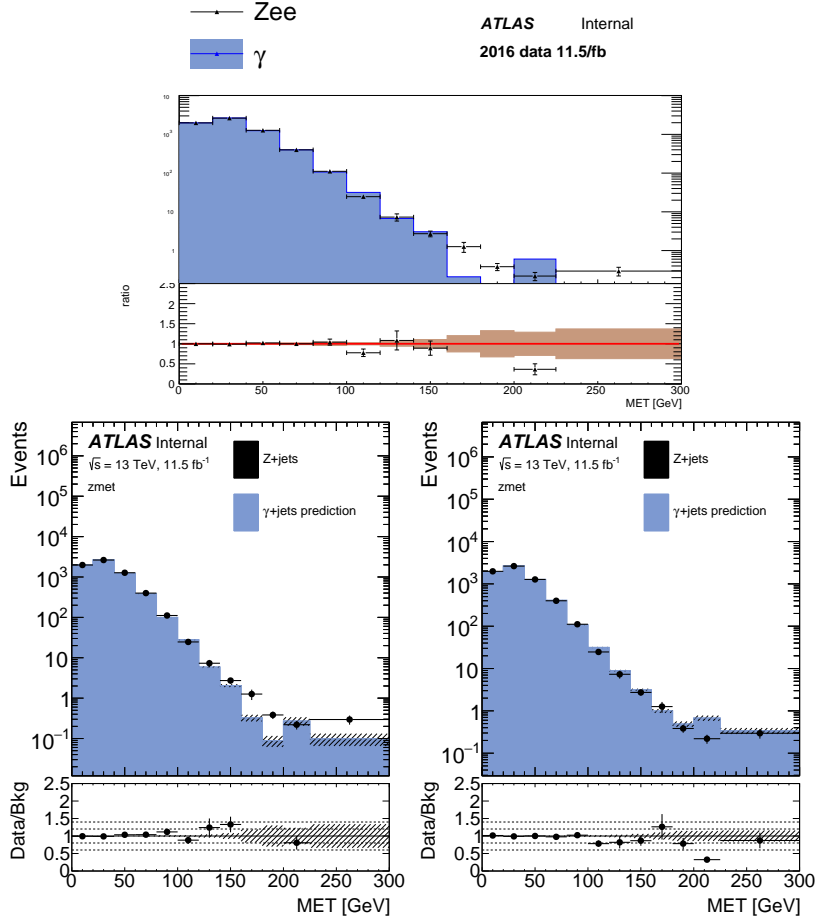


Figure 61: E_T^{miss} distribution comparing MC distributions of photon and Z events before any smearing is applied (top), with only p_T reweighting applied (bottom left), and after p_T reweighting and smearing have both been applied (bottom right) in the ee channel of 2016 data.

10.2.4 Determining the $m_{\ell\ell}$ Shape

One complication thus far ignored is that γ -jet have obvious value of $m_{\ell\ell}$, or even of H_T , which includes the p_T of the two leading leptons. Both of these variables are determined by creating histograms binned in the boson p_T and sampling.

In the case of H_T , distributions of the scalar sum of the p_T of the leading leptons are made for each Z p_T bin. A sampled value from the distribution is then added to the H_T of the jets in a photon event to produce the final estimate. This sampling is done before any reweighting is performed because the H_T is needed to make the pre-selection for the reweighting process. However, the smearing is performed inclusively in H_T , so this procedure can be performed using the smeared photon p_T to choose the distribution to sample.

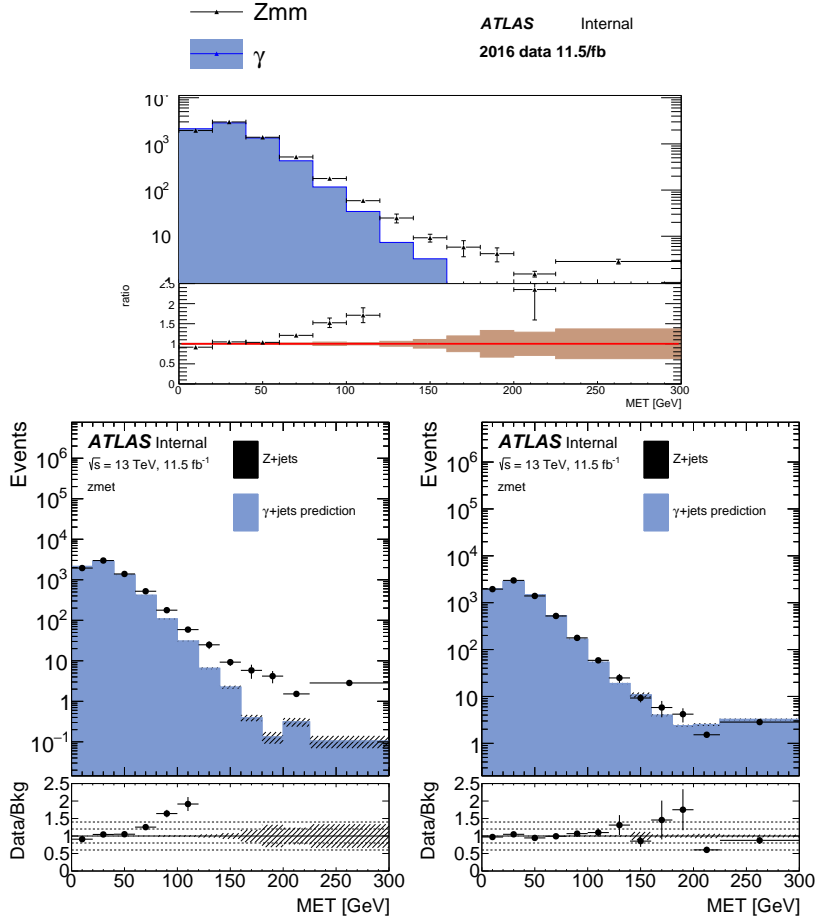


Figure 62: E_T^{miss} distribution comparing MC distributions of photon and Z events before any smearing is applied (top), with only p_T reweighting applied (bottom left), and after p_T reweighting and smearing have both been applied (bottom right) in the $\mu\mu$ channel of 2016 data.

The $m_{\ell\ell}$ determination is done after both the smearing and reweighting, and is tied closely to the smearing step. Mismeasurements in lepton p_T can create E_T^{miss} in a $Z/\gamma^* + \text{jets}$ event, but the same event is likely to migrate off the Z $m_{\ell\ell}$ window due to the mismeasured lepton. Thus it is very important that the two effects be carefully correlated in the manipulated photon events. To achieve this, MC Z events from the 1-jet CR described in Section 10.2.2 are used to make two-dimensional distributions of $m_{\ell\ell}$ as a function of the difference between reconstructed and true Z p_T for the ee and $\mu\mu$ channels. A photon event then uses its assigned Δp_T to index the distribution, and an $m_{\ell\ell}$ value is sampled from the corresponding bin.

To test the soundness of this procedure, it is repeated purely in MC, and the results of the MC prediction and the data prediction are compared to the $m_{\ell\ell}$ distribution in $Z/\gamma^* + \text{jets}$ MC in Figure 62. After the

$m_{\ell\ell}$ distribution has been emulated, a cut requiring that the photon events be “on the Z mass peak” can be required.

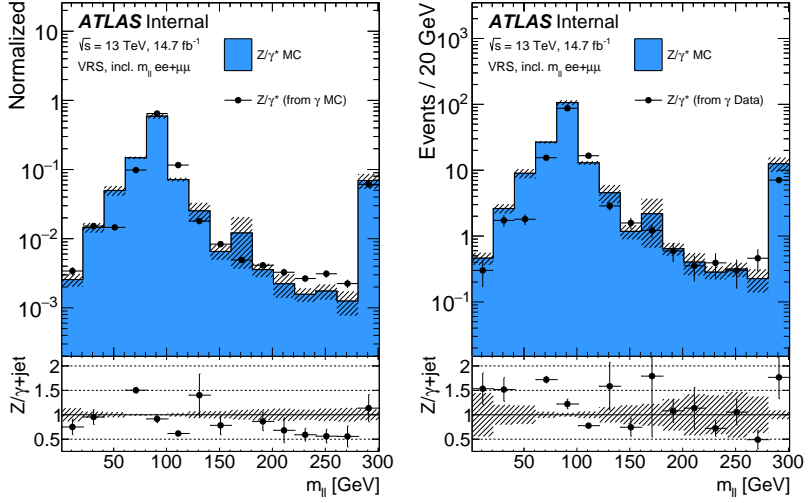


Figure 63: $Z/\gamma^* + \text{jets}$ MC $m_{\ell\ell}$ distribution compared to the prediction from $\gamma + \text{jets}$ method performed on MC (left) and the prediction from $\gamma + \text{jets}$ method performed on data (right).

10.2.5 Subtraction of $V\gamma$ Events

At high E_T^{miss} , where the signal region lies, contamination of CR- γ with $V\gamma$ events becomes significant, as shown in Figure 63. These events must be subtracted from the $\gamma + \text{jets}$ prediction because, once the photons are corrected to approximate Zs, they essentially provide a (not very accurate) prediction of diboson events, which are already accounted for in another background estimate.

This subtraction accomplished by performing the $\gamma + \text{jets}$ method on $V\gamma$ MC to approximate these backgrounds’ contribution to the final E_T^{miss} distribution. This contribution is then subtracted from the $\gamma + \text{jets}$ prediction, the impact of which can be seen in Figure 64. As expected, the impact is greatest at high E_T^{miss} where these backgrounds are most significant.

10.2.6 Validation in Data

The $\gamma + \text{jets}$ jets method is validated in a region called VRZ, defined in Table 7, which is similar to SRZ, but with an inverted E_T^{miss} cut. Figure 65 shows the low- E_T^{miss} portion of this VR where the $Z/\gamma^* + \text{jets}$ background is dominant. Here, the three data-driven background estimates, as well as the remaining MC backgrounds are stacked and compared to the data yield in this region, demonstrating excellent agreement across a wide E_T^{miss} range.

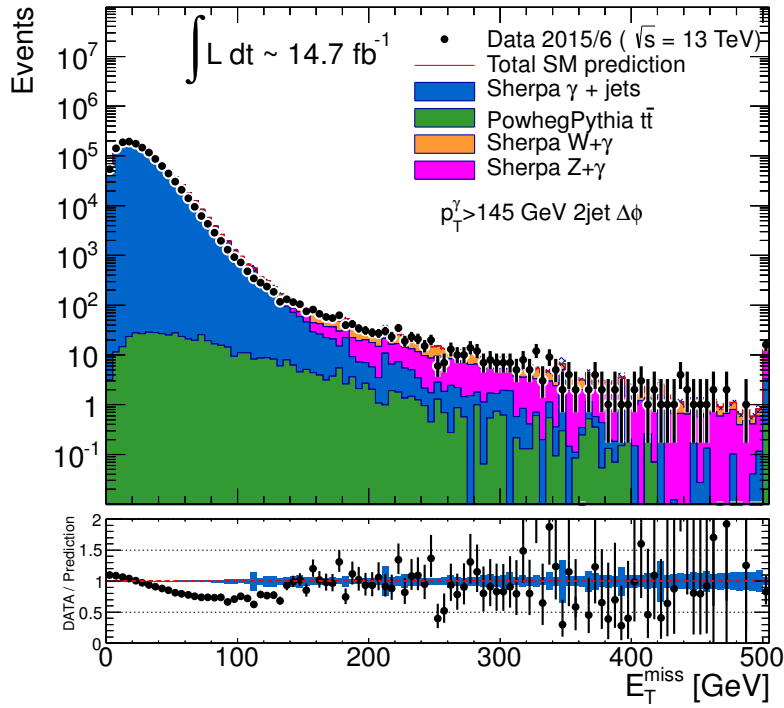


Figure 64: Comparison of data and MC in CR- γ without any H_T cut, including the contributions from various $V\gamma$ processes.

An additional check can be made in VRZ by removing the $\Delta\phi(\text{jet}_{12}, p_T^{\text{miss}})$ intended to suppress the $Z/\gamma^* + \text{jets}$ background from jet mismeasurement. Figure 66 shows the distribution of this variable in VRZ, and demonstrates that, even at low values where the $Z/\gamma^* + \text{jets}$ background is dominant, the $\gamma + \text{jets}$ method models it accurately.

10.3 FAKE AND NON-PROMPT LEPTONS

The *fakes* background consists of processes that produce only one lepton, but whose events are otherwise kinematically similar to the SR. These processes include semileptonic $t\bar{t}$, $W+\text{jets}$, and single top processes. Though these processes typically only produce one lepton, they can be reconstructed with two leptons due to a hadron being misidentified as a lepton or due to a real non-prompt lepton resulting from photon conversions or B -hadron decays. As such, it includes both events that have been properly reconstructed and many that are included in the SR due to imperfect reconstruction. As with the $Z/\gamma^* + \text{jets}$ background, it is very difficult to predict with MC because the flaws in reconstruction are typically less well described by the models used in MC production than the successes. Nonetheless, a rough estimate can be made of this background by using MC, which indicates that the number of fake events in SRZ is consistent with zero.

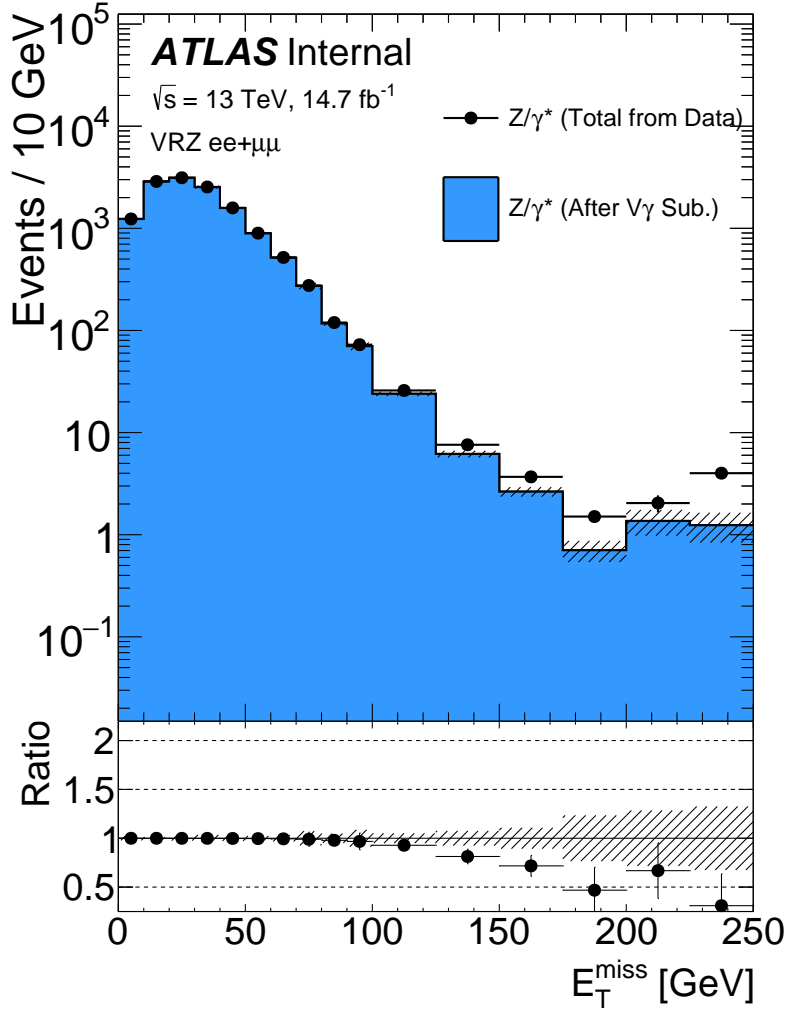


Figure 65: Total $\gamma + \text{jets}$ data prediction in SRZ (excluding the E_T^{miss} cut) and the prediction after the $V\gamma$ subtraction.

Despite the small predicted contribution in the [SR](#), a data-driven method called the *matrix method* is employed to estimate these fake events [\[16\]](#). This method is also used to estimate the fakes contribution to other control and validation regions where their impact is more significant.

In the matrix method, the quality requirements for signal leptons are loosened to give a selection of baseline leptons (see [Table 3](#) and [Table 4](#)), which consist of a higher fraction of fake leptons. In each [CR](#), [VR](#), or [SR](#), the remaining kinematic selections are made on the baseline leptons, and the number of leptons in the region which pass the signal lepton requirements (N_{pass}) and the number which fail (N_{fail}) are measured. For a 1-lepton selection, these quantities can be used

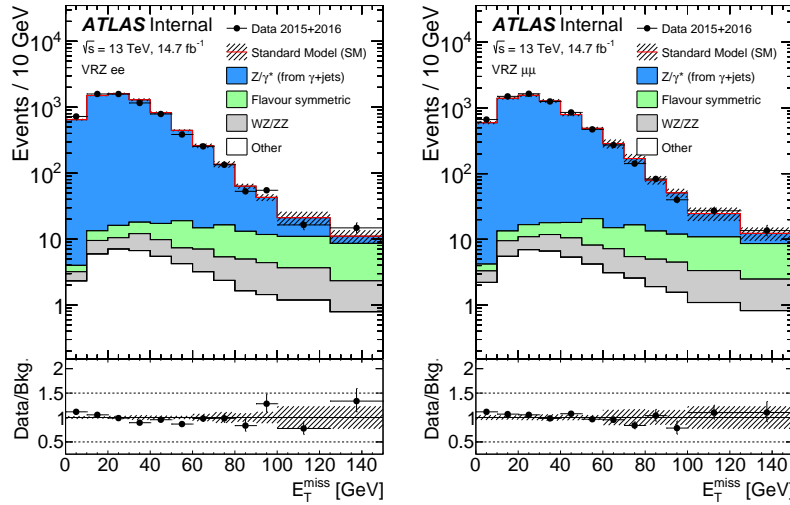


Figure 66: E_T^{miss} distribution in VRZ ee (left) and $\mu\mu$ (right) with total data yield compared to the sum of the prediction from the $\gamma + \text{jets}$ method, the prediction from the flavor symmetry method, the prediction from the fake background estimation (included under “other”), and the remaining backgrounds taken from MC.

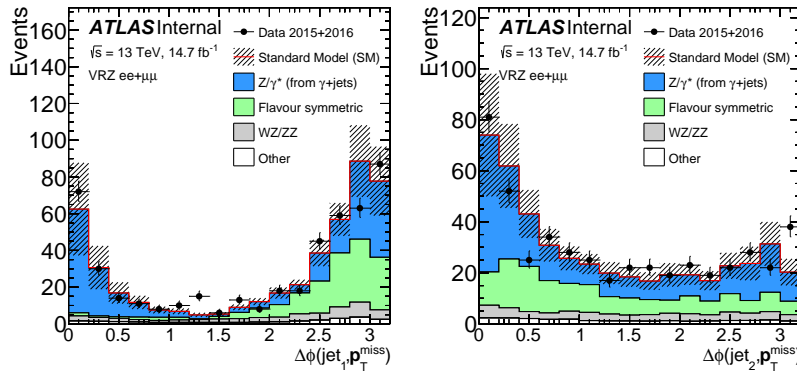


Figure 67: $\Delta\phi(\text{jet}, p_T^{\text{miss}})$ distribution in for the leading jet (left) and the sub-leading jet (right). The comparison is performed in VRZ with the cut on $\Delta\phi(\text{jet}_{12}, p_T^{\text{miss}})$ removed. The total data yield is compared to the sum of the prediction from the $\gamma + \text{jets}$ method, the prediction from the flavor symmetry method, the prediction from the fake background estimation (included under “other”), and the remaining backgrounds taken from MC.

to predict the number of fake events that pass the selection according to:

$$N_{\text{pass}}^{\text{fake}} = \frac{N_{\text{fail}} - (1/\epsilon^{\text{real}} - 1) \times N_{\text{pass}}}{1/\epsilon^{\text{fake}} - 1/\epsilon^{\text{real}}}. \quad (39)$$

The efficiencies ϵ^{real} and ϵ^{fake} give the relative identification efficiency from baseline to signal for genuine, prompt leptons and fake and non-prompt leptons, respectively. For a 2-lepton selection, the

principle is the same, but the equation is more complicated, requiring a four-by-four matrix to account for possible combinations of real and fake leptons.

To calculate ϵ^{real} , the tag-and-probe method is performed a selection of $Z \rightarrow \ell\ell$ data events, CR-real, described in [Table 14](#). In this method, one *tag* lepton passing a signal selection is required, as is another *probe* lepton passing a baseline requirement. Distributions in $m_{\ell\ell}$ for events with a tag and a passing probe and events with a tag and a failing probe are produced and fit, and the efficiency is computed using the ratio acquired from the fit. A comparison of data and MC in CR-real can be seen in [Figure 67](#).

Fakes regions	E_T^{miss} [GeV]	H_T [GeV]	n_{jets}	$m_{\ell\ell}$ [GeV]	SF/DF	OS/SS	n_{ℓ}
CR-real	–	> 200	≥ 2	81–101	2ℓ SF	OS	2
CR-fake	< 125	–	–	> 12	2ℓ SF/DF	SS	≥ 2

[Table 14](#): Control regions used to measure efficiencies of real and fake leptons. The flavour combination of the dilepton pair is denoted as either “SF” for same-flavour or “DF” for different flavour. The charge combination of the leading lepton pairs are given as “SS” for same-sign or “OS” for opposite-sign.

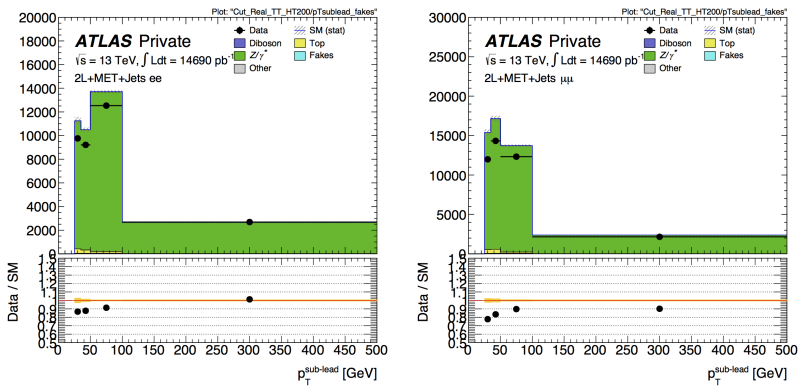


[Figure 68](#): Sub-leading lepton p_T for ee (left) and $\mu\mu$ (right) events in the tight-tight region used to measure the real-lepton efficiency for 2016.

The fake efficiency, ϵ^{fake} , is determined using the tag-and-probe method in CR-fake, also described in [Table 14](#). This region is different from all other regions considered in this analysis because it requires same-sign leptons. Very few processes genuinely produce two same-sign leptons, so this region is enhanced in fake leptons. An upper limit on E_T^{miss} is placed on CR-fake to limit the possible contamination

from [BSM](#) processes. According to [MC](#), real, prompt leptons make up about 7% (11%) of the baseline electron (muon) sample and about 10% (61%) of the signal electron (muon) sample in this region. These real lepton backgrounds are subtracted from the CR-fake yields when calculating the efficiencies. [Figure 68](#) shows a comparison of data and [MC](#) in this region.

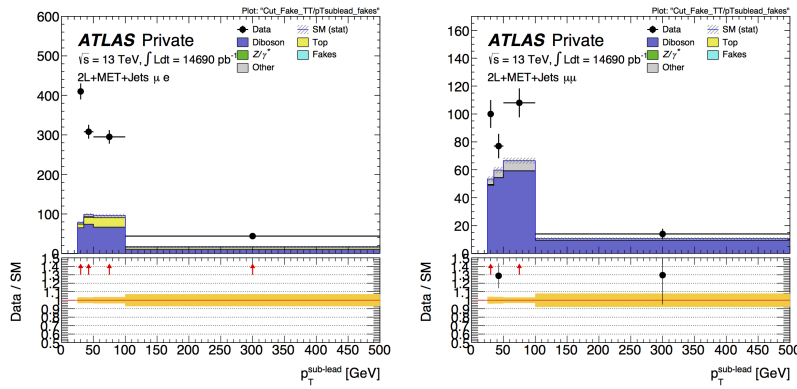


Figure 69: Sub-leading lepton p_T for μe (left) and $\mu \mu$ (right) events in the tight-tight region used to measure the fake-lepton efficiency for 2016.

This method is validated in a fakes-rich validation region with a same-sign lepton requirement, $E_T^{\text{miss}} \geq 50 \text{ GeV}$, ≥ 2 jets, and a veto on $m_{\ell\ell}$ on the Z-mass peak for same flavor channels. The results of this validation can be seen in [Figure 69](#). With the systematic uncertainties included, the prediction agrees well with the data across a wide range of $m_{\ell\ell}$ values.

10.4 DIBOSON AND RARE TOP PROCESSES

The remaining backgrounds are diboson processes (excluding WW , which is included in the [FS](#) background) and rare top processes. Dibosons events make up about 30% of the events in SRZ, while rare top process contributions are much smaller. Both are taken directly from [MC](#), with validation regions to confirm the accuracy of the prediction. These regions are described in [Table 7](#), and target different parts of these backgrounds. VR-ZZ is a four-lepton selection designed to select a very pure sample of ZZ events. VR-WZ requires three leptons and makes specific cuts on m_T , the transverse mass, and E_T^{miss} in order to select mostly $WZ \rightarrow ll\nu\nu$ events. VR-3L is similar to VR-S, but loosens the H_T and E_T^{miss} cuts and requires at least three leptons. This region is designed to target any ≥ 3 -lepton process in a region as kinematically close to SRZ as possible while still maintaining enough events to validate. The makeups of these multilepton validation regions, as well as VRS, are shown in [Table 15](#).

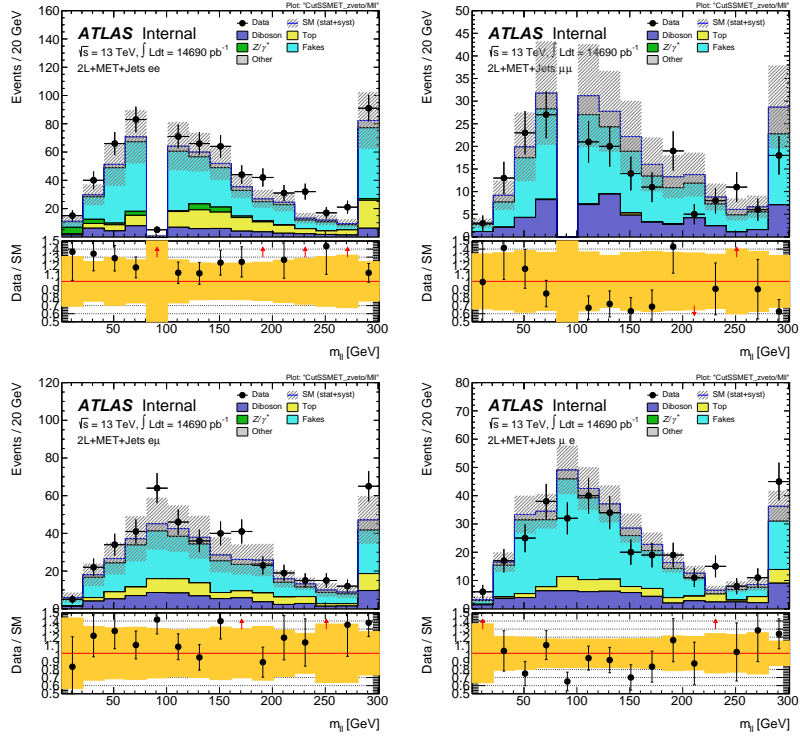


Figure 70: Same sign validation regions in the ee (top left), $\mu\mu$ (top right), $e\mu$ (bottom left) and μe (bottom right) channels combining 2015+2016 data. Uncertainty bands include both statistical and systematic uncertainties.

	VR-S	VR-WZ	VR-ZZ	VR-3L
Observed events	236	698	132	32
Total expected background	224 ± 41	613 ± 66	139 ± 25	35 ± 10
Flavour-symmetric	99 ± 8	-	-	-
WZ/ZZ events	27 ± 13	573 ± 66	139 ± 25	25 ± 10
Rare top events	11 ± 3	14 ± 3	0.44 ± 0.11	9.1 ± 2.3
$Z/\gamma^* + \text{jets}$ events	84 ± 37	-	-	-
Fake lepton events	4 ± 4	26 ± 6	-	0.6 ± 0.3

Table 15: Yields in validation regions. In VRS, data-driven background estimates are used for $Z/\gamma^* + \text{jets}$, fakes, and **FS** processes. All other backgrounds are taken from **MC**, including all backgrounds in the multi-lepton **VRs**. Uncertainties include statistical and systematic components.

To confirm that the kinematics are well modeled in the diboson validation regions, distributions of boson mass and p_T are shown in

MC and data. Figures 70 and 71 show these distributions for VR-WZ, and Figure 72 shows these distributions for VR-ZZ.

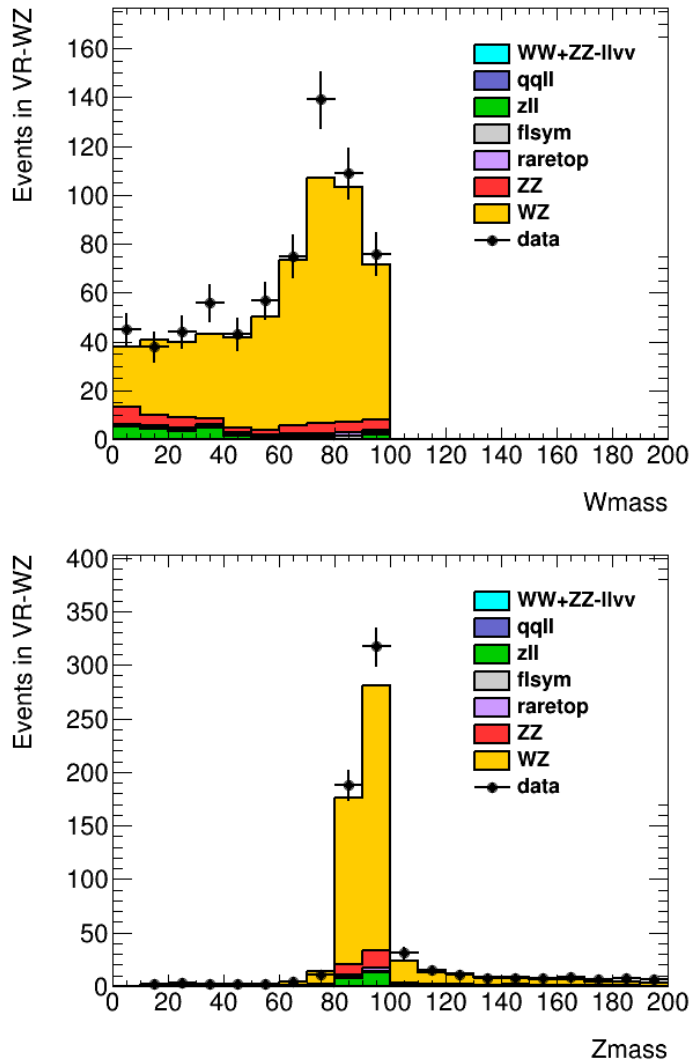


Figure 71: Distribtuions of data and MC in VR-WZ. Reconstructed transverse mass of the W (top) and mass of the Z (bottom).

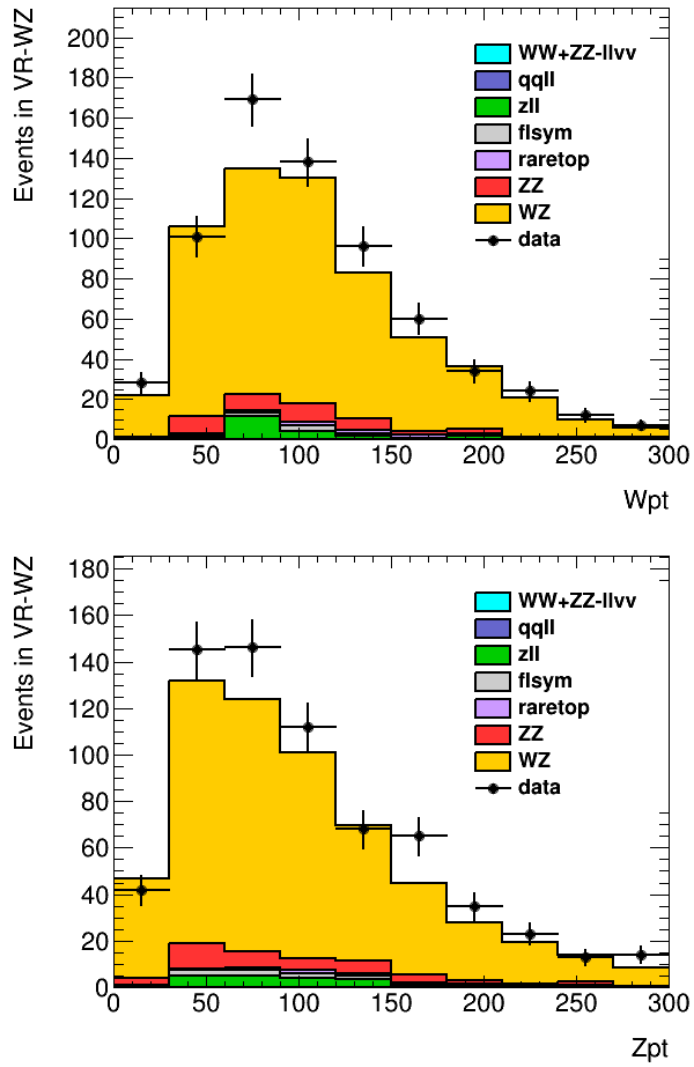


Figure 72: Distribtuions of data and MC in VR-WZ. p_T of the W (top) and Z (bottom).

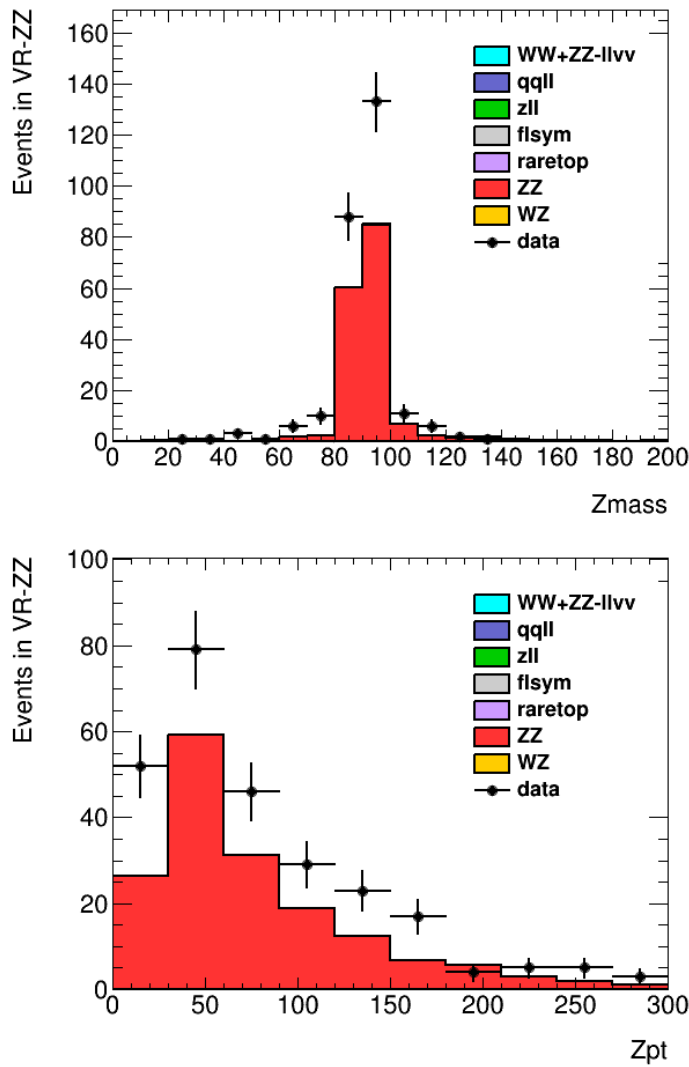


Figure 73: Distributions in VR-WZ. On the top, mass of the Z bosons in the event, and on the bottom, p_T of the Z bosons.

SYSTEMATIC UNCERTAINTIES

11.1 UNCERTAINTIES ON DATA-DRIVEN BACKGROUNDS

11.1.1 Uncertainties on the Flavor Symmetry Method

The flavor symmetry method is a data driven method that makes its estimate primarily on based events populating an SR-like CR in the different-flavor channel. The statistical uncertainty on these events makes up the dominant uncertainty on the method. To reduce this uncertainty, the $m_{\ell\ell}$ range on the CR is expanded, approximately tripling the number of events in CR-FS. The statistical uncertainty is reduced by this expansion, though it is still significantly higher than any of the other systematic uncertainties on this method, as seen in Table 16. Also included in the statistical uncertainty column is the uncertainty on the number of non-FS events in CR-FS, which is used to scale the prediction to account for contamination in the CR.

Reg.	Ch.	Pred.	Uncertainties					
			stat. clos.	MC and α	k usage	dAOD shape	$m_{\ell\ell}$	total
SRZ	ee	16.50	1.82	0.88	0.53	0.12	0.22	2.11
	$\mu\mu$	16.67	1.83	0.79	0.33	0.11	0.23	2.04
	$ee+\mu\mu$	33.16	3.66	1.07	0.86	0.23	0.45	3.94
VRS	ee	49.70	3.21	2.34	2.20	0.34	0.75	4.61
	$\mu\mu$	49.60	3.14	2.88	1.40	0.31	0.75	4.56
	$ee+\mu\mu$	99.31	6.34	4.00	3.60	0.65	1.49	8.47

Table 16: Uncertainties in the on-Z signal and validation regions. Nominal predictions are given with statistical uncertainty (including uncertainty from subtracted backgrounds), MC Closure uncertainty, uncertainty on the prediction from varying k and α by their statistical uncertainties, comparing the efficiencies from AODs to that of DAODs, and on the $m_{\ell\ell}$ widening, which includes MC statistics and a data/MC comparison in a loosened region.

The next largest contribution to the uncertainty comes from MC closure tests, which are used to determine how effective the method is in its prediction. If, for example, using weights derived from an inclusive selection at high E_T^{miss} lead to a bias, the closure test would indicate that and an appropriate uncertainty could be placed on the

estimate based on the difference between the MC prediction and the prediction from the flavor symmetry method.

In this test, the entire FS procedure is performed on $t\bar{t}$ MC, including a recalculation of weighting factors α and k . The prediction from $e\mu$ events in MC is compared to the MC ee and $\mu\mu$ events, as seen in Figure 73. The difference between the two predictions is then summed in quadrature with the statistical uncertainty on each prediction to give the total closure uncertainty seen in Table 16. In these closure tests, all predictions agree within the statistical uncertainty, so the largest contributor to the resulting error is MC statistics.

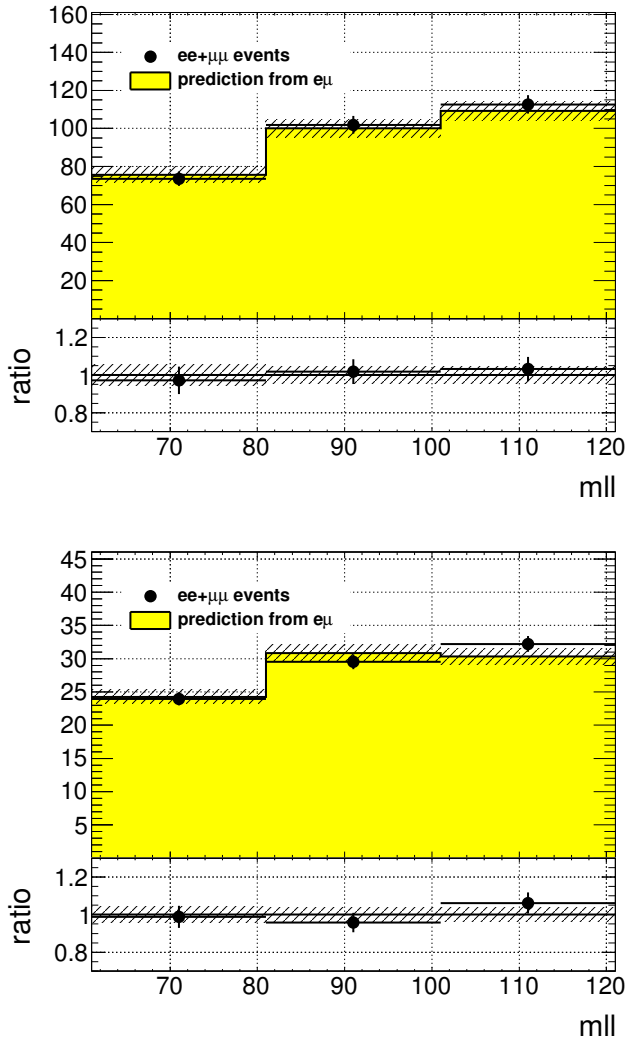


Figure 74: MC closure plots of VRS (top) and SRZ (bottom). The number of events from MC (black points) is compared to the number of events predicted from the flavor symmetry method (yellow histogram). The comparison is performed before the expanded $m_{\ell\ell}$ window is used to predict the on-Z bin, but because the shape is taken from the same MC, the result is identical.

A small uncertainty is added based on the statistical uncertainty on the k and α factors derived from data. These factors are measured in many different bins (see, for example, the different measurements of k in Figure 74), and as a consequence, some bins can have very large statistical uncertainties. To assess the uncertainty on the total estimate, each measurement of these factors is varied by its uncertainty in order to produce the maximum and minimum possible prediction. The differences with respect to the nominal prediction are used to create a symmetrized error, which is included in Table 16.

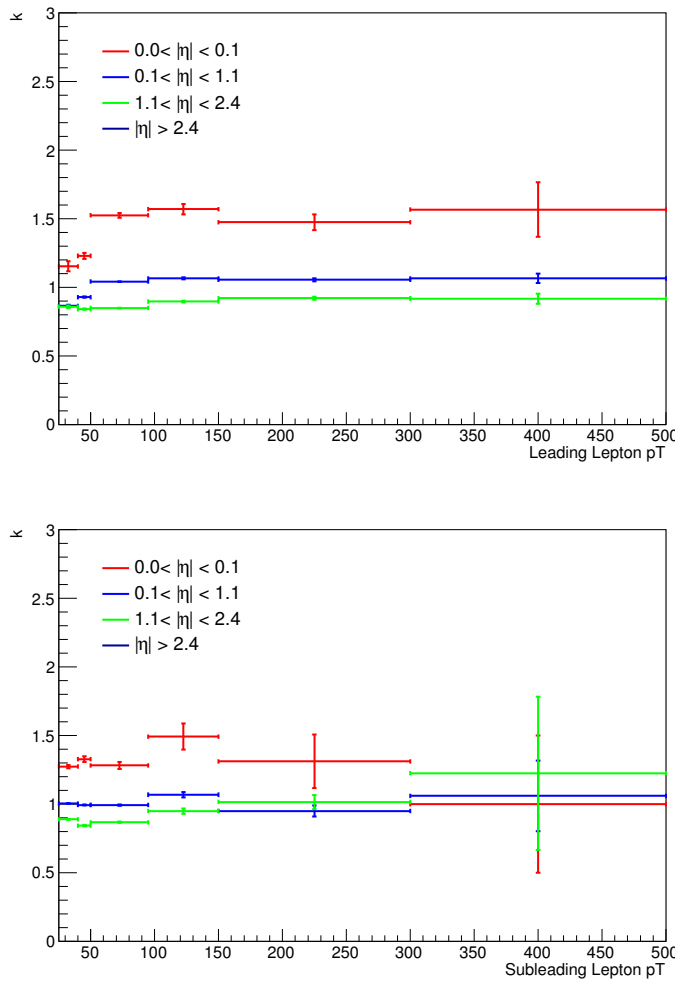


Figure 75: Measurements of k , the ratio of electron to muon events, in bins of p_T and η . On the top is the measurements indexed by the leading lepton, while the measurements indexed by the subleading lepton are on the bottom. These efficiencies are for the 2016 dataset.

The next uncertainty considers a potential bias in the way the α factors are calculated. Because they are derived from data, there is already trigger dependence in data collection; only events passing a trigger are stored. Additional trigger dependence is created by the data format used for analysis. ATLAS data and MC are stored in a for-

mat called Analysis Object Data ([AOD](#)), but smaller, slimmer versions of these datasets, called derived AODs ([dAODs](#)) are used for analysis. These [dAODs](#) are designed with specific analyses in mind, filtering on the triggers and objects required by the analyses. As a consequence, in the [dAOD](#) used in this analysis, there are explicit requirements that lepton or E_T^{miss} triggers are passed in order for events to be included.

As a consequence, the trigger efficiencies ϵ^{trig} used in [Equation 34](#) to define α do not consider all possible data events. The ϵ^{trig} factor is calculated for each trigger using events passing the kinematic selection for that trigger, outlined in [Section 9.1](#). The efficiency factor is then measured according to the equation

$$\epsilon^{\text{trig}} = \frac{N_{\text{trig}}}{N_{\text{all}}} \quad (40)$$

where N_{trig} is the number of events passing the trigger in the kinematic selection and N_{all} is all events in the selection. The latter measurement is the one subject to this bias, as it contains only the events that pass at least one trigger required for inclusion in the [dAOD](#). As a consequence of these missing events, the ϵ^{trig} values will be artificially high. However, because the ratio of trigger efficiencies for the different channels is the only quantity needed for this analysis, the missing events will only bias the prediction if the different channels are differently impacted by the trigger preselection.

Calculating the flavor symmetry method's dependence on these biases requires the use of [MC](#). With a generated [MC](#) sample, there is no trigger dependence, so an unskimmed sample can be compared to a typical skimmed [MC dAOD](#) to identify the effect of the skimming. [Figure 75](#) shows a comparison of the α factors calculated for different bins in E_T^{miss} from the nominal source, data, as well as these two [MC](#) sources. A E_T^{miss} dependence would be the most likely bias between the two [MC](#)-derived α factors because E_T^{miss} triggers are the only triggers besides lepton triggers that will allow an event to be accepted into the [dAOD](#) used by this analysis. Though there is some difference between the data-derived α and those taken from [MC](#), it is clear from this plot that there is very little dependence on the choice of an unskimmed or skimmed sample. The calculation of the uncertainty is performed by repeating the flavor symmetric method in [MC](#) with each of the two α factors and using the difference between the estimates as a symmetric error.

The last uncertainty relates to the main [MC](#) dependence of the method - the $m_{\ell\ell}$ shape of the [FS](#) background. A correction factor is taken from [MC](#) in order to account for the $m_{\ell\ell}$ widening, and the accuracy of that factor must be checked. Its shape is compared to that of data in region similar to VR-FS, but with an H_T cut lowered to 300 GeV to increase statistics. The difference between the fraction of events on the Z-mass peak in data and [MC](#) in this region is taken as

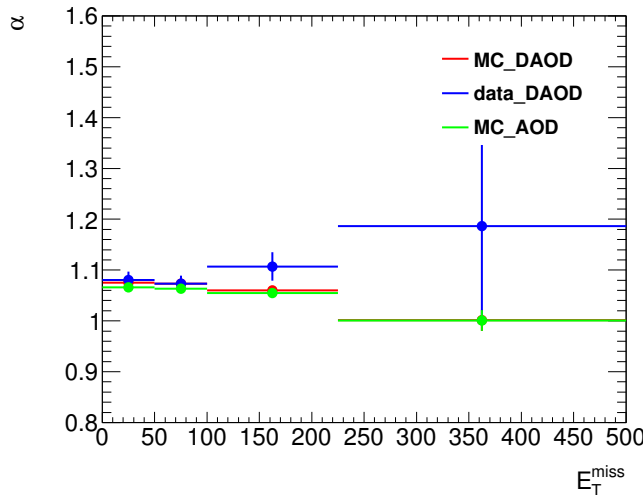


Figure 76: α , the trigger efficiency ratio, calculated as a function of E_T^{miss} from three different sources: data (blue), the usual skimmed $t\bar{t}$ MC (red), and an unskimmed $t\bar{t}$ MC (green).

a systematic uncertainty. To confirm that using this lowered H_T cut still gives a valid answer, the fractions are compared as a function of H_T in Figure 76. In these plots, especially in the higher-statistics 2016 plot, it is clear both that the data and MC agree very well and that there is no strong H_T dependence.

All the uncertainties are calculated independently for the two datasets, then added together. Statistical uncertainties, including the MC closure statistical uncertainties and the k and α uncertainties, are added in quadrature between the two years. Uncertainties that are more likely to be correlated, such as the difference between the two estimates in MC closure and the dependence on using a dAOD to calculate trigger efficiencies, are added linearly. The total uncertainty is about 12% of the nominal prediction in SRZ and about 9% in VRS.

11.1.2 Uncertainties on the $\gamma + \text{jets}$ Method

One of the largest sources of uncertainty on the $\gamma + \text{jets}$ method is derived by comparing the results from reweighting in different variables. Though boson p_T is used as the nominal reweighting variable, the differences in the kinematics of γ and Z events also impact number of jets, H_T , and E_T (which includes the mass of the boson). The $\gamma + \text{jets}$ method is repeated using each of these variables to reweight, and their E_T^{miss} distributions are shown in Figure 77. The maximum difference from the nominal prediction is symmetrized and used as an uncertainty on the method.

Another uncertainty is applied to estimate the validity of using MC in a 1-jet CR to determine the smearing functions. Smearing functions are made using data from the same 1-jet region and using MC in a

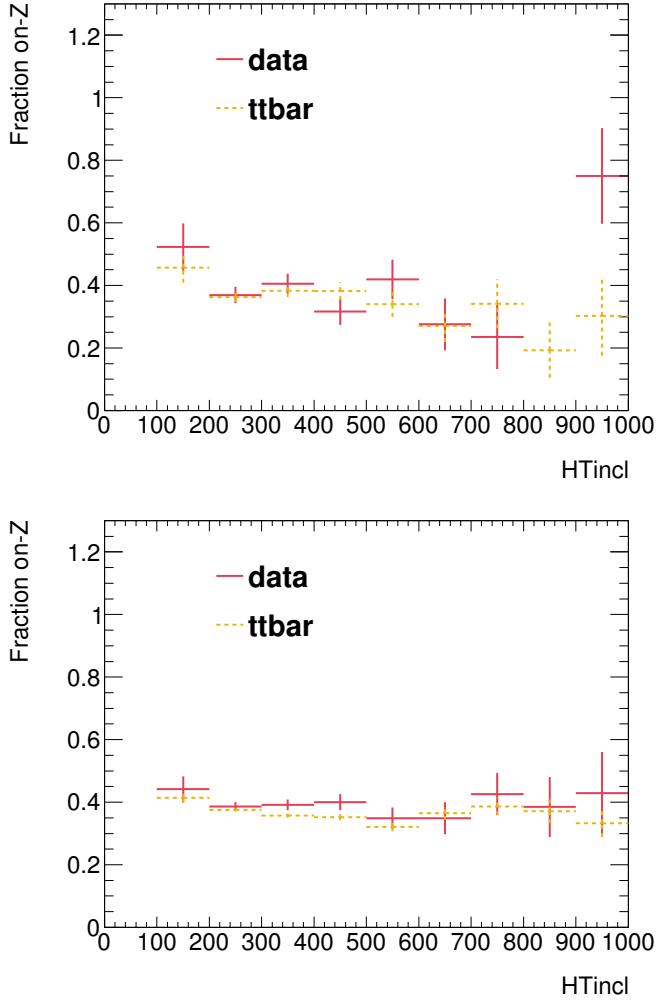


Figure 77: Plots of the fraction of on-Z events with a VR-FS-like selection as a function of H_T . The top figure shows 2015 data and MC while the bottom figure shows the same for 2016.

≥ 2 -jet region otherwise identical to the 1-jet CR. These distributions are also shown in Figure 77, and like the alternate reweighting distributions, are used to find a maximum difference from the nominal prediction which is translated into a symmetric error.

As in the flavor symmetric method, the full procedure is carried out on MC in order to test MC closure, including a recalculation of any weights that are typically derived from data. The resulting comparison between $Z/\gamma^* + \text{jets}$ MC and the $\gamma + \text{jets}$ method performed on MC can be seen in Figure 78. The final non-closure uncertainty is taken from VRS, where larger numbers of events give a clearer picture of the success of the method than in SRZ. In this region, the statistical uncertainty on the prediction is compared to the non-closure, and the larger of the two is used as the final uncertainty.

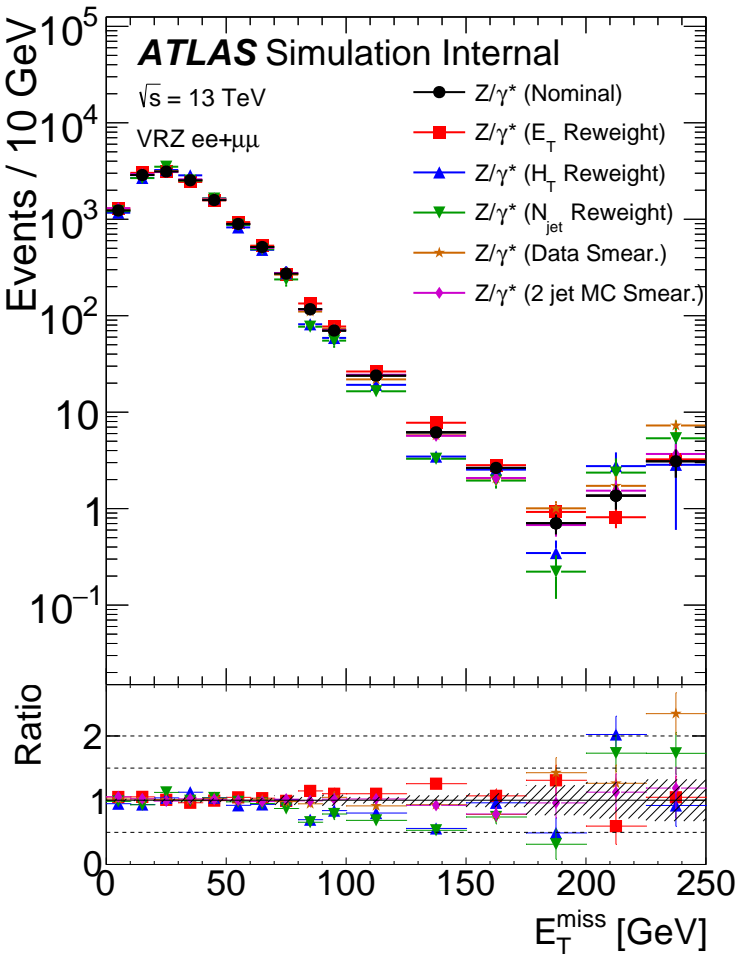


Figure 78: E_T^{miss} distributions for $\gamma + \text{jets}$ predictions using different reweighting variables, as well as distributions with the nominal reweighting but with smearing functions taken from data and from [MC](#) in a ≥ 2 -jet region.

The uncertainty on the $V\gamma$ contamination in CR- γ is also considered. An uncertainty on the [MC](#) prediction is made based on comparison of data and [MC](#) in a $W + \text{jets}$ [VR](#), shown in Figure 79. This [VR](#) is similar to CR- γ , but instead of vetoing events with leptons, requires at least one well-isolated lepton with a p_T over 25 GeV. At E_T^{miss} values over 100 GeV, region is about 90% pure in $W\gamma$ processes. The [MC](#) agrees well with data in this region, even at very high E_T^{miss} , so an uncertainty of 16% based primarily on statistical uncertainty in this [VR](#) is placed on the $V\gamma$ [MC](#). This uncertainty is propagated to the final result through the subtraction procedure.

An uncertainty on the $m_{\ell\ell}$ shape is determined using [MC](#) closure as well. The comparison of $m_{\ell\ell}$ shapes in $Z/\gamma^* + \text{jets}$ [MC](#) and the $\gamma + \text{jets}$ method applied to [MC](#) is shown in Figure 62. As with the main [MC](#) closure test, the maximum of the statistical uncertainty and the non-closure is taken as the final uncertainty on this background.

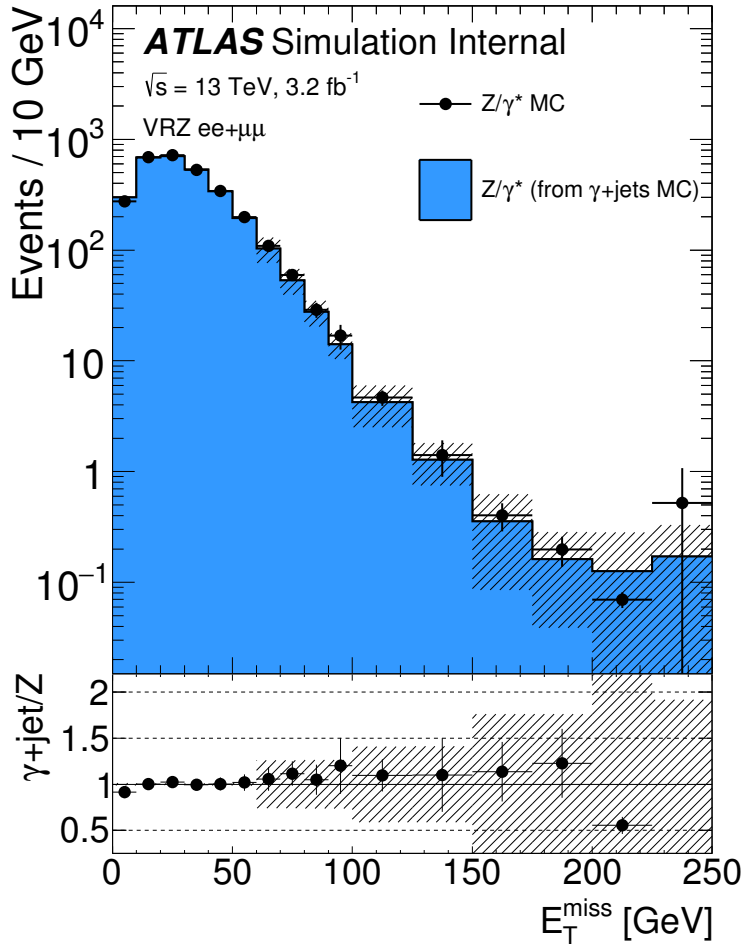


Figure 79: MC closure of the $\gamma + \text{jets}$ method as a function of E_T^{miss} comparing the MC prediction of the Z background with the $\gamma + \text{jets}$ method performed on $\gamma + \text{jets}$ MC. The uncertainty band includes both statistical and reweighting uncertainties.

One last uncertainty based on the statistical uncertainty on the number of $\gamma + \text{jets}$ data events used for this method is also included. The full breakdown of uncertainty in SRZ can be seen in [Table 17](#).

11.1.3 Uncertainties on the Fakes Background

Systematic uncertainties on the fakes background are derived from a series of variations on the nominal method. Variations include scaling the real and fake efficiencies up and down by their statistical uncertainties, scaling the prompt lepton contamination in CR-fake up and down by 20%, and by requiring and vetoing b -tagged jets in CR-fake to determine the dependence on heavy flavor. Statistical uncertainties can also be large in regions with small numbers of events in the baseline selection, such as SRZ. In other regions, the b -tagging

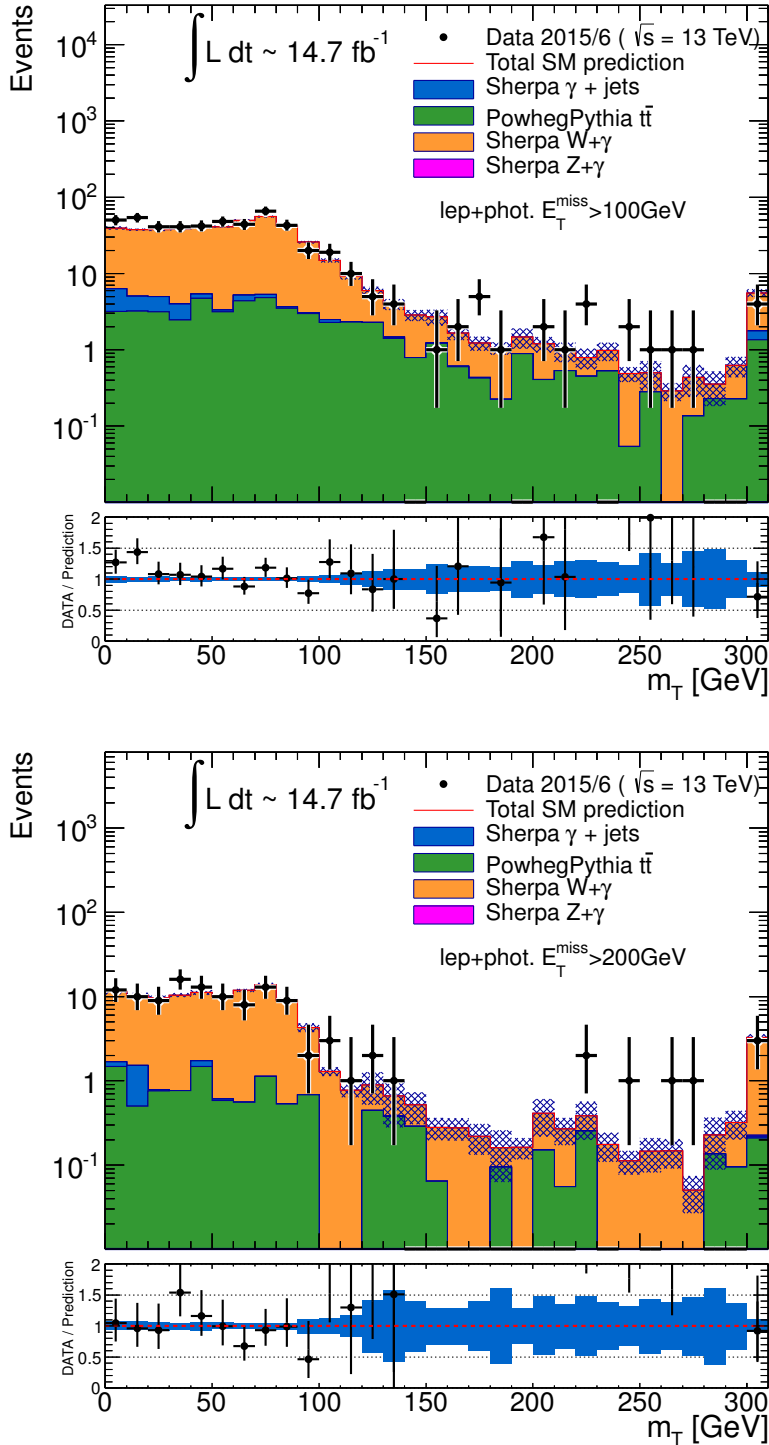


Figure 8o: Distributions of $m_T(\ell, E_T^{\text{miss}})$, the transverse mass of the lepton and the E_T^{miss} in a VR designed to target $W\gamma$ processes. Top is the distribution with a E_T^{miss} cut at 100 GeV, and bottom is the same distribution with a E_T^{miss} cut of 200 GeV.

dependence provides the largest uncertainty. The full breakdown of uncertainties for the most important regions are listed in Table 18.

Ch.	Pred.	Uncertainties (%)						
		$V\gamma$ sub.	MC clos.	$m_{\ell\ell}$ shape	re- weight	smear	stat.	total
ee	1.02	53.0	21.0	19.0	100.0	65.0	56.0	145.0
$\mu\mu$	2.08	27.0	14.0	23.0	30.0	59.0	40.0	86.0
$ee+\mu\mu$	3.1	36.0	16.0	22.0	43.0	60.0	33.0	92.0

Table 17: Uncertainty breakdown for the $\gamma + \text{jets}$ method in SRZ. Uncertainties considered are the impact of MC uncertainty on $V\gamma$ backgrounds, MC closure, uncertainty on $m_{\ell\ell}$ shape (also determined via MC closure), reweighting uncertainties, smearing uncertainties, and statistical uncertainty on the $\gamma + \text{jets}$ events used in the method.

Variation	SRZ	CRT	CRFS	VRFS	VRS	VRT
Nominal	0.10 ± 1.61	25.39 ± 5.35	3.73 ± 2.19	10.53 ± 3.56	3.64 ± 3.20	80.06 ± 9.80
EL F Up	0.15	30.23	3.96	10.93	3.56	92.46
EL F Down	0.06	21.80	3.52	10.18	3.54	70.07
EL R Up	0.25	26.17	3.92	11.10	4.13	82.57
EL R Down	-0.07	24.51	3.52	9.92	3.10	77.24
MU F Up	-0.20	32.48	4.77	16.41	5.25	86.48
MU F Down	0.29	20.17	2.91	7.04	2.87	70.12
MU R Up	0.13	25.67	3.78	10.66	3.81	81.18
MU R Down	0.05	25.04	3.67	10.38	3.44	78.72
Total Sys	$+0.26 -0.35$	$+8.64 -6.39$	$+1.08 -0.87$	$+5.92 -3.56$	$+1.70 -0.97$	$+14.24 -14.42$
Total Sys (%)	$+261.05 -354.72$	$+34.01 -25.19$	$+29.05 -23.23$	$+56.22 -33.85$	$+46.57 -26.60$	$+17.78 -18.02$
Real Cont. Up	0.23	20.97	3.06	8.08	3.15	68.79
Real Cont. Down	-0.01	29.67	4.38	12.95	4.16	90.23
b-jet	0.31	40.44	5.28	8.98	5.63	120.50
no b-jet	0.16	23.44	3.08	11.38	3.97	70.55
Total Sys	$+0.25 -0.11$	$+15.65 -4.83$	$+1.69 -0.93$	$+2.56 -2.90$	$+2.09 -0.49$	$+41.71 -14.74$
Total Sys (%)	$+260.46 -109.06$	$+61.66 -19.02$	$+45.30 -24.85$	$+24.32 -27.58$	$+57.31 -13.35$	$+52.10 -18.42$

Table 18: Systematic uncertainties on the fake-lepton background for on-Z regions for 2015+2016 yields. The nominal yield includes statistical uncertainty from the baseline selection in a given region. The following rows indicate the results of varying the real and fake lepton efficiencies up and down by their statistical uncertainty. Real cont. gives an uncertainty on the contamination of real leptons in the fake lepton efficiency. b-jet and no b-jet indicate the impact of requiring or vetoing b-tagged jets in the regions used to measure the fake efficiency.

11.2 THEORETICAL AND EXPERIMENTAL UNCERTAINTIES

Experimental uncertainties cover any detector effect or LHC condition that may not be modeled precisely correctly in MC. For each uncertainty, a standard prescription from the ATLAS experiment is followed. Uncertainties are included on the following parameters:

- Luminosity (2.9%) [3, 7]
- Jet energy scale [13]

- Jet energy resolution [13]
- Jet vertex tagging
- Heavy flavor tagging
- E_T^{miss} soft term [11]
- e/μ momentum scale
- e/μ trigger, reconstruction, and identification efficiencies
- Pile-up

These uncertainties are applied to all MC samples used in the analysis. This includes signal models, diboson and rare top samples for the nominal estimate, and all backgrounds taken from MC in the sideband fit.

Theoretical uncertainties include cross-section uncertainties, scale uncertainties, and PDF uncertainties. For the diboson samples, the scale uncertainties, given in Table 19 are calculated by varying each scale up and down by a factor of two. These are combined with a 6% cross-section uncertainty and a generator uncertainty obtained by comparing Powheg and Sherpa MC yields in a given region. This generator uncertainty, shown in Table 20, is dominant in most regions. Rare top processes are given a 13% PDF and scale variation uncertainty [28] and a 22% cross section uncertainty [38, 56, 67].

Signal models have both the central value and uncertainty on cross-sections taken from an envelope of predictions using different scales and PDF sets [62]. The signal processes are calculated at Next-to-Leading-Logarithmic Accuracy (NLO+NLL); they are initially calculated at NLO in the strong coupling constant, with additional terms from next-to-leading-logarithmic resummation of soft gluon emission [30–32, 63, 64].

11.3 IMPACT OF UNCERTAINTIES ON THE SIGNAL REGION

The breakdown of each major uncertainty's contribution to the total uncertainty in SRZ is shown in Table 21. The dominant uncertainty is the diboson generator uncertainty, followed by the statistical uncertainty from the FS background. Uncertainties smaller than 1% are not shown in the table.

$VV \rightarrow llvv$ Samples							
	SRZ	VRS	CRT	VRT	VRWZ	VRZZ	VR _{3L}
resummation	0.07	0.03	0.01	0.02	0.00	0.00	0.00
renormalization	0.13	0.17	0.16	0.22	0.00	0.00	0.00
factorization	0.01	0.01	0.01	0.03	0.00	0.00	0.00
total	0.15	0.17	0.16	0.22	0.00	0.00	0.00
$WZ \rightarrow lllv$ Samples							
	SRZ	VRS	CRT	VRT	VRWZ	VRZZ	VR _{3L}
resummation	0.07	0.05	0.13	0.08	0.02	0.00	0.01
renormalization	0.26	0.20	0.28	0.21	0.07	0.00	0.18
factorization	0.04	0.04	0.02	0.06	0.01	0.00	0.02
total	0.28	0.21	0.31	0.23	0.07	0.00	0.18
$ZZ \rightarrow llll$ Samples							
	SRZ	VRS	CRT	VRT	VRWZ	VRZZ	VR _{3L}
resummation	0.27	1.07	0.01	0.01	0.06	0.01	0.53
renormalization	0.28	0.26	0.30	0.60	0.07	0.04	0.14
factorization	0.27	0.25	0.30	0.58	0.13	0.02	0.16
total	0.48	1.13	0.43	0.84	0.16	0.05	0.57

Table 19: Fractional uncertainties of dibosons in signal and validation regions from Sherpa scale variations.

Region	Sherpa Events/fb ⁻¹	Sherpa Events	Powheg Events/fb ⁻¹	Powheg Events	% Difference
WZ Samples					
SRZ+VRZ	5.219	76.722	3.286	48.300	37.046
CRT+VRT	1.060	15.583	0.742	10.913	29.970
WW/ZZ Samples					
SRZ+VRZ	1.921	28.244	0.685	10.070	71.424
CRT+VRT	6.281	92.332	3.142	46.188	55.474

Table 20: Comparison of yields in on-Z and off-Z regions in Sherpa and Powheg diboson MC at 14.7 fb⁻¹.

Source	Relative systematic uncertainty [%]
	SRZ
Total systematic uncertainty	17
WZ/ZZ generator uncertainty	13
Flavour symmetry (statistical)	7
WZ/ZZ scale uncertainty	6
$Z/\gamma^* + \text{jets}$ (systematic)	4
Flavour symmetry (systematic)	3
$Z/\gamma^* + \text{jets}$ (statistical)	2
Fake-leptons	1

Table 21: Overview of the dominant sources of systematic uncertainty on the total background estimate in the signal regions. The values shown are relative to the total background estimate, shown in %.

12

RESULTS

13

INTERPRETATIONS

Part V

CONCLUSIONS

This section presents conclusions and an outlook for future work.

CONCLUSIONS

15

OUTLOOK

BIBLIOGRAPHY

- [1] .
- [2] .
- [3] ATLAS Collaboration. “Luminosity determination in pp collisions at $\sqrt{s} = 8$ TeV using the ATLAS detector at the LHC.” In: *to be submitted to Eur. Phys. J. C* ().
- [4] ATLAS Collaboration. “The ATLAS Experiment at the CERN Large Hadron Collider.” In: *JINST* 3 (2008), S08003. doi: [10.1088/1748-0221/3/08/S08003](https://doi.org/10.1088/1748-0221/3/08/S08003).
- [5] ATLAS Collaboration. *Search for physics beyond the Standard Model in events with a Z boson and large missing transverse momentum using $\sqrt{s} = 7$ TeV pp collisions from the LHC with the ATLAS detector.* ATLAS-CONF-2012-046. 2012. URL: <http://cdsweb.cern.ch/record/1448222>.
- [6] ATLAS Collaboration. *Search for supersymmetry in final states with jets, missing transverse momentum and a Z boson at $\sqrt{s} = 8$ TeV with the ATLAS detector.* ATLAS-CONF-2012-152. 2012. URL: <http://cds.cern.ch/record/1493491>.
- [7] ATLAS Collaboration. “Improved luminosity determination in pp collisions at $\sqrt{s} = 7$ TeV using the ATLAS detector at the LHC.” In: *Eur. Phys. J. C* 73 (2013), p. 2518. doi: [10.1140/epjc/s10052-013-2518-3](https://doi.org/10.1140/epjc/s10052-013-2518-3). arXiv: [1302.4393 \[hep-ex\]](https://arxiv.org/abs/1302.4393).
- [8] ATLAS Collaboration. “A neural network clustering algorithm for the ATLAS silicon pixel detector.” In: *JINST* 9 (2014), P09009. doi: [10.1088/1748-0221/9/09/P09009](https://doi.org/10.1088/1748-0221/9/09/P09009). arXiv: [1406.7690 \[hep-ex\]](https://arxiv.org/abs/1406.7690).
- [9] ATLAS Collaboration. *Electron efficiency measurements with the ATLAS detector using the 2012 LHC proton–proton collision data.* ATLAS-CONF-2014-032. 2014. URL: <http://cdsweb.cern.ch/record/1706245>.
- [10] ATLAS Collaboration. *Tagging and suppression of pileup jets with the ATLAS detector.* ATLAS-CONF-2014-018. 2014. URL: <http://cds.cern.ch/record/1700870>.
- [11] ATLAS Collaboration. *Expected performance of missing transverse momentum reconstruction for the ATLAS detector at $\sqrt{s} = 13$ TeV.* ATL-PHYS-PUB-2015-023. 2015. URL: <http://cds.cern.ch/record/2037700>.
- [12] ATLAS Collaboration. *Expected performance of the ATLAS b-tagging in Run-2.* ATL-PHYS-PUB-2015-022. 2015. URL: <http://cdsweb.cern.ch/record/2037697>.

- [13] ATLAS Collaboration. *Jet Calibration and Systematic Uncertainties for Jets Reconstructed in the ATLAS Detector at $\sqrt{s} = 13$ TeV*. ATL-PHYS-PUB-2015-015. 2015. URL: <http://cds.cern.ch/record/2037613>.
- [14] ATLAS Collaboration. *Measurement of performance of the pixel neural network clustering algorithm of the ATLAS experiment at $\sqrt{s} = 13$ TeV*. ATL-PHYS-PUB-2015-044. 2015. URL: <http://cdsweb.cern.ch/record/2054921>.
- [15] ATLAS Collaboration. *Robustness of the Artificial Neural Network Clustering Algorithm of the ATLAS experiment*. ATL-PHYS-PUB-2015-052. 2015. URL: <http://cdsweb.cern.ch/record/2116350>.
- [16] ATLAS Collaboration. “Search for squarks and gluinos in events with isolated leptons, jets and missing transverse momentum at $\sqrt{s} = 8$ TeV with the ATLAS detector.” In: *JHEP* 1504 (2015), p. 116. DOI: [10.1007/JHEP04\(2015\)116](https://doi.org/10.1007/JHEP04(2015)116). arXiv: [1501.03555 \[hep-ex\]](https://arxiv.org/abs/1501.03555).
- [17] ATLAS Collaboration. “Search for supersymmetry in events containing a same-flavour opposite-sign dilepton pair, jets, and large missing transverse momentum in $\sqrt{s} = 8$ TeV pp collisions with the ATLAS detector.” In: *Eur. Phys. J. C* 75 (2015), p. 318. DOI: [10.1140/epjc/s10052-015-3518-2](https://doi.org/10.1140/epjc/s10052-015-3518-2). arXiv: [1503.03290 \[hep-ex\]](https://arxiv.org/abs/1503.03290).
- [18] ATLAS Collaboration. *2015 start-up trigger menu and initial performance assessment of the ATLAS trigger using Run-2 data*. ATL-DAQ-PUB-2016-001. 2016. URL: <http://cds.cern.ch/record/2136007>.
- [19] ATLAS Collaboration. “Measurement of the differential cross-section of highly boosted top quarks as a function of their transverse momentum in $\sqrt{s} = 8$ TeV proton-proton collisions using the ATLAS detector.” In: *Phys. Rev. D* 93.3 (2016), p. 032009. DOI: [10.1103/PhysRevD.93.032009](https://doi.org/10.1103/PhysRevD.93.032009). arXiv: [1510.03818 \[hep-ex\]](https://arxiv.org/abs/1510.03818).
- [20] ATLAS Collaboration. *Modelling of the $t\bar{t}H$ and $t\bar{t}V$ ($V = W, Z$) processes for $\sqrt{s} = 13$ TeV ATLAS analyses*. ATL-PHYS-PUB-2016-005. 2016. URL: <http://cds.cern.ch/record/2120826>.
- [21] ATLAS Collaboration. *Monte Carlo Generators for the Production of a W or Z/ γ^* Boson in Association with Jets at ATLAS in Run 2*. ATL-PHYS-PUB-2016-003. 2016. URL: <http://cds.cern.ch/record/2120133>.
- [22] ATLAS Collaboration. *Multi-Boson Simulation for 13 TeV ATLAS Analyses*. ATL-PHYS-PUB-2016-002. 2016. URL: <http://cds.cern.ch/record/2119986>.

- [23] ATLAS Collaboration. “Muon reconstruction performance of the ATLAS detector in proton–proton collision data at $\sqrt{s} = 13$ TeV.” In: *Eur. Phys. J. C* 76 (2016), p. 292. doi: [10.1140/epjc/s10052-016-4120-y](https://doi.org/10.1140/epjc/s10052-016-4120-y). arXiv: [1603.05598 \[hep-ex\]](https://arxiv.org/abs/1603.05598).
- [24] ATLAS Collaboration. *Simulation of top quark production for the ATLAS experiment at $\sqrt{s} = 13$ TeV*. ATL-PHYS-PUB-2016-004. 2016. URL: <http://cds.cern.ch/record/2120417>.
- [25] Morad Aaboud et al. “A measurement of material in the ATLAS tracker using secondary hadronic interactions in 7 TeV pp collisions.” In: (2016). arXiv: [1609.04305 \[hep-ex\]](https://arxiv.org/abs/1609.04305).
- [26] S. Agostinelli et al. “GEANT4: A simulation toolkit.” In: *Nucl. Instrum. Meth. A* 506 (2003), pp. 250–303. doi: [10.1016/S0168-9002\(03\)01368-8](https://doi.org/10.1016/S0168-9002(03)01368-8).
- [27] S. Alioli, P. Nason, C. Oleari, and E. Re. “A general framework for implementing NLO calculations in shower Monte Carlo programs: the POWHEG BOX.” In: *JHEP* 1006 (2010), p. 043. arXiv: [1002.2581 \[hep-ph\]](https://arxiv.org/abs/1002.2581).
- [28] J. Alwall, R. Frederix, S. Frixione, V. Hirschi, F. Maltoni, O. Mattelaer, H. S. Shao, T. Stelzer, P. Torrielli, and M. Zaro. “The automated computation of tree-level and next-to-leading order differential cross sections, and their matching to parton shower simulations.” In: *JHEP* 07 (2014), p. 079. doi: [10.1007/JHEP07\(2014\)079](https://doi.org/10.1007/JHEP07(2014)079). arXiv: [1405.0301 \[hep-ph\]](https://arxiv.org/abs/1405.0301).
- [29] Richard D. Ball et al. “Parton distributions with LHC data.” In: *Nucl. Phys.* B867 (2013), pp. 244–289. doi: [10.1016/j.nuclphysb.2012.10.003](https://doi.org/10.1016/j.nuclphysb.2012.10.003). arXiv: [1207.1303 \[hep-ph\]](https://arxiv.org/abs/1207.1303).
- [30] W. Beenakker, R. Höpker, M. Spira, and P.M. Zerwas. “Squark and gluino production at hadron colliders.” In: *Nucl. Phys. B* 492 (1997), pp. 51–103. doi: [10.1016/S0550-3213\(97\)00084-9](https://doi.org/10.1016/S0550-3213(97)00084-9). arXiv: [hep-ph/9610490 \[hep-ph\]](https://arxiv.org/abs/hep-ph/9610490).
- [31] W. Beenakker et al. “Soft-gluon resummation for squark and gluino hadroproduction.” In: *JHEP* 0912 (2009), p. 041. doi: [10.1088/1126-6708/2009/12/041](https://doi.org/10.1088/1126-6708/2009/12/041). arXiv: [0909.4418 \[hep-ph\]](https://arxiv.org/abs/0909.4418).
- [32] W. Beenakker et al. “Squark and gluino hadroproduction.” In: *Int. J. Mod. Phys. A* 26 (2011), pp. 2637–2664. doi: [10.1142/S0217751X11053560](https://doi.org/10.1142/S0217751X11053560). arXiv: [1105.1110 \[hep-ph\]](https://arxiv.org/abs/1105.1110).
- [33] C. P. Burgess and G. D. Moore. *The standard model: A primer*. Cambridge University Press, 2006. ISBN: 9780511254857, 9781107404267, 9780521860369.
- [34] CMS Collaboration. “Search for physics beyond the standard model in events with a Z boson, jets, and missing transverse energy in pp collisions at $\sqrt{s} = 7$ TeV.” In: *Phys. Lett. B* 716 (2012), pp. 260–284. doi: [10.1016/j.physletb.2012.08.026](https://doi.org/10.1016/j.physletb.2012.08.026). arXiv: [1204.3774 \[hep-ex\]](https://arxiv.org/abs/1204.3774).

- [35] CMS Collaboration. “Measurement of the integrated and differential t-tbar production cross sections for high-pt top quarks in pp collisions at $\sqrt{s} = 8$ TeV.” In: *Phys. Rev. D* (2016). Submitted. arXiv: [1605.00116 \[hep-ex\]](#).
- [36] Matteo Cacciari, Gavin P. Salam, and Gregory Soyez. “The Anti-k(t) jet clustering algorithm.” In: *JHEP* 0804 (2008), p. 063. DOI: [10.1088/1126-6708/2008/04/063](#). arXiv: [0802.1189 \[hep-ph\]](#).
- [37] J. M. Campbell and R. K. Ellis. “An update on vector boson pair production at hadron colliders.” In: *Phys. Rev. D* 60 (1999), p. 113006. arXiv: [hep-ph/9905386 \[hep-ph\]](#).
- [38] J. M. Campbell and R. K. Ellis. “ $t\bar{t}$ W production and decay at NLO.” In: *JHEP* 1207 (2012), p. 052. arXiv: [1204.5678 \[hep-ph\]](#).
- [39] J. M. Campbell, R. K. Ellis, and C. Williams. “Vector boson pair production at the LHC.” In: *JHEP* 1107 (2011), p. 018. arXiv: [1105.0020 \[hep-ph\]](#).
- [40] S. Catani and M. Grazzini. “An NNLO subtraction formalism in hadron collisions and its application to Higgs boson production at the LHC.” In: *Phys. Rev. Lett.* 98 (2007), p. 222002. arXiv: [hep-ph/0703012 \[hep-ph\]](#).
- [41] S. Catani, L. Cieri, G. Ferrera, D. de Florian, and M. Grazzini. “Vector boson production at hadron colliders: a fully exclusive QCD calculation at NNLO.” In: *Phys. Rev. Lett.* 103 (2009), p. 082001. arXiv: [0903.2120 \[hep-ph\]](#).
- [42] ATLAS Collaboration. *Measurement of the photon identification efficiencies with the ATLAS detector using LHC Run-1 data*. 2016. eprint: [arXiv:1606.01813](#).
- [43] ATLAS Collaboration. “Muon reconstruction performance of the ATLAS detector in proton–proton collision data at $\sqrt{s}=13$ TeV.” In: (2016). DOI: [10.1140/epjc/s10052-016-4120-y](#). eprint: [arXiv:1603.05598](#).
- [44] The ALICE Collaboration. “The ALICE experiment at the CERN LHC.” In: *Journal of Instrumentation* 3.08 (2008), S08002. URL: <http://stacks.iop.org/1748-0221/3/i=08/a=S08002>.
- [45] The CMS Collaboration. “The CMS experiment at the CERN LHC.” In: *Journal of Instrumentation* 3.08 (2008), S08004. URL: <http://stacks.iop.org/1748-0221/3/i=08/a=S08004>.
- [46] The LHCb Collaboration. “The LHCb Detector at the LHC.” In: *Journal of Instrumentation* 3.08 (2008), S08005. URL: <http://stacks.iop.org/1748-0221/3/i=08/a=S08005>.
- [47] The MEG Collaboration. “Search for the Lepton Flavour Violating Decay $\mu^+ \rightarrow e^+ \gamma$ with the Full Dataset of the MEG Experiment.” In: (2016). eprint: [arXiv:1605.05081](#).

- [48] Craig J Copi, David N. Schramm, and Michael S. Turner. “Big-Bang Nucleosynthesis and the Baryon Density of the Universe.” In: (1994). DOI: [10.1126/science.7809624](https://doi.org/10.1126/science.7809624). eprint: [arXiv:astro-ph/9407006](https://arxiv.org/abs/astro-ph/9407006).
- [49] M. Czakon, P. Fiedler, and A. Mitov. “Total Top-Quark Pair-Production Cross Section at Hadron Colliders Through $O(\alpha_s^4)$.” In: *Phys. Rev. Lett.* 110 (2013), p. 252004. arXiv: [1303.6254 \[hep-ph\]](https://arxiv.org/abs/1303.6254).
- [50] M. Czakon and A. Mitov. “Top++: A Program for the Calculation of the Top-Pair Cross-Section at Hadron Colliders.” In: *Comput. Phys. Commun.* 185 (2014), p. 2930. DOI: [10.1016/j.cpc.2014.06.021](https://doi.org/10.1016/j.cpc.2014.06.021). arXiv: [1112.5675 \[hep-ph\]](https://arxiv.org/abs/1112.5675).
- [51] *Electron efficiency measurements with the ATLAS detector using the 2015 LHC proton-proton collision data*. Tech. rep. ATLAS-CONF-2016-024. Geneva: CERN, 2016. URL: <http://cds.cern.ch/record/2157687>.
- [52] “Electron performance measurements with the ATLAS detector using the 2010 LHC proton-proton collision data.” In: *Eur. Phys. J. C* 72 (2012), p. 1909. DOI: [10.1140/epjc/s10052-012-1909-1](https://doi.org/10.1140/epjc/s10052-012-1909-1). arXiv: [1110.3174 \[hep-ex\]](https://arxiv.org/abs/1110.3174).
- [53] Lyndon Evans and Philip Bryant. “LHC Machine.” In: *Journal of Instrumentation* 3.08 (2008), S08001. URL: <http://stacks.iop.org/1748-0221/3/i=08/a=S08001>.
- [54] S. Frixione, P. Nason, and C. Oleari. “Matching NLO QCD computations with parton shower simulations: the POWHEG method.” In: *JHEP* 0711 (2007), p. 070. arXiv: [0709.2092 \[hep-ph\]](https://arxiv.org/abs/0709.2092).
- [55] D. Galbraith.
- [56] M. V. Garzelli, A. Kardos, C. G. Papadopoulos, and Z. Trocsanyi. “ $t\bar{t} W^{+-}$ and $t\bar{t} Z$ Hadroproduction at NLO accuracy in QCD with Parton Shower and Hadronization effects.” In: *JHEP* 11 (2012), p. 056. DOI: [10.1007/JHEP11\(2012\)056](https://doi.org/10.1007/JHEP11(2012)056). arXiv: [1208.2665 \[hep-ph\]](https://arxiv.org/abs/1208.2665).
- [57] T. Gleisberg et al. “Event generation with Sherpa 1.1.” In: *JHEP* 0902 (2009), p. 007. arXiv: [0811.4622 \[hep-ph\]](https://arxiv.org/abs/0811.4622).
- [58] David J Griffiths. *Introduction to elementary particles; 2nd rev. version*. Physics textbook. New York, NY: Wiley, 2008. URL: [https://cds.cern.ch/record/111880](http://cds.cern.ch/record/111880).
- [59] Huang, Qing-Guo, Wang, Ke, and Wang, Sai. “Constraints on the neutrino mass and mass hierarchy from cosmological observations.” In: *Eur. Phys. J. C* 76.9 (2016), p. 489. DOI: [10.1140/epjc/s10052-016-4334-z](https://doi.org/10.1140/epjc/s10052-016-4334-z). URL: <http://dx.doi.org/10.1140/epjc/s10052-016-4334-z>.

- [60] P. Hut and K. A. Olive. “A cosmological upper limit on the mass of heavy neutrinos.” In: *Physics Letters B* 87 (Oct. 1979), pp. 144–146. DOI: [10.1016/0370-2693\(79\)90039-X](https://doi.org/10.1016/0370-2693(79)90039-X).
- [61] N. Kidonakis. “Two-loop soft anomalous dimensions for single top quark associated production with a W^- or H^- .” In: *Phys. Rev. D* 82 (2010), p. 054018. DOI: [10.1103/PhysRevD.82.054018](https://doi.org/10.1103/PhysRevD.82.054018). arXiv: [1005.4451 \[hep-ph\]](https://arxiv.org/abs/1005.4451).
- [62] Michael Kramer et al. *Supersymmetry production cross sections in pp collisions at $\sqrt{s} = 7$ TeV*. 2012. arXiv: [1206.2892 \[hep-ph\]](https://arxiv.org/abs/1206.2892).
- [63] A. Kulesza and L. Motyka. “Soft gluon resummation for the production of gluino-gluino and squark-antisquark pairs at the LHC.” In: *Phys. Rev. D* 80 (2009), p. 095004. DOI: [10.1103/PhysRevD.80.095004](https://doi.org/10.1103/PhysRevD.80.095004). arXiv: [0905.4749 \[hep-ph\]](https://arxiv.org/abs/0905.4749).
- [64] A. Kulesza and L. Motyka. “Threshold resummation for squark-antisquark and gluino-pair production at the LHC.” In: *Phys. Rev. Lett.* 102 (2009), p. 111802. DOI: [10.1103/PhysRevLett.102.111802](https://doi.org/10.1103/PhysRevLett.102.111802). arXiv: [0807.2405 \[hep-ph\]](https://arxiv.org/abs/0807.2405).
- [65] *LEP design report*. Copies shelved as reports in LEP, PS and SPS libraries. Geneva: CERN, 1984. URL: <https://cds.cern.ch/record/102083>.
- [66] Hung-Liang Lai et al. “New parton distributions for collider physics.” In: *Phys. Rev. D* 82 (2010), p. 074024. DOI: [10.1103/PhysRevD.82.074024](https://doi.org/10.1103/PhysRevD.82.074024). arXiv: [1007.2241 \[hep-ph\]](https://arxiv.org/abs/1007.2241).
- [67] A. Lazopoulos, T. McElmurry, K. Melnikov, and F. Petriello. “Next-to-leading order QCD corrections to $t\bar{t}Z$ production at the LHC.” In: *Phys. Lett. B* 666 (2008), p. 62. arXiv: [0804.2220 \[hep-ph\]](https://arxiv.org/abs/0804.2220).
- [68] A. D. Martin, W. J. Stirling, R. S. Thorne, and G. Watt. “Parton distributions for the LHC.” In: (2009). DOI: [10.1140/epjc/s10052-009-1072-5](https://doi.org/10.1140/epjc/s10052-009-1072-5). eprint: [arXiv:0901.0002](https://arxiv.org/abs/0901.0002).
- [69] Stephen P. Martin. “A Supersymmetry primer.” In: (1997). [Adv. Ser. Direct. High Energy Phys. 18, 1 (1998)]. DOI: [10.1142/9789812839657_0001](https://doi.org/10.1142/9789812839657_0001), [10.1142/9789814307505_0001](https://doi.org/10.1142/9789814307505_0001). arXiv: [hep-ph/9709356 \[hep-ph\]](https://arxiv.org/abs/hep-ph/9709356).
- [70] Johan Messchendorp. “Physics with Charmonium – A few recent highlights of BESIII.” In: *PoS Bormio2013* (2013), p. 043. arXiv: [1306.6611 \[hep-ex\]](https://arxiv.org/abs/1306.6611).
- [71] P. Nason. “A new method for combining NLO QCD with shower Monte Carlo algorithms.” In: *JHEP* 0411 (2004), p. 040. arXiv: [hep-ph/0409146 \[hep-ph\]](https://arxiv.org/abs/hep-ph/0409146).
- [72] *Official Isolation Working Points*. Geneva, 2016. URL: <https://twiki.cern.ch/twiki/bin/view/AtlasProtected/IsolationSelectionTool#Photons>.

- [73] *Photon Identification Efficiencies using 2016 Data with radiative Z boson decays.* Tech. rep. EGAM-2016-003. Geneva: CERN, 2016. URL: <https://atlas.web.cern.ch/Atlas/GROUPS/PHYSICS/PLOTS/EGAM-2016-003/index.html>.
- [74] *Photon identification in 2015 ATLAS data.* Tech. rep. ATL-PHYS-PUB-2016-014. Geneva: CERN, 2016. URL: <https://cds.cern.ch/record/2203125>.
- [75] T. Sjöstrand, S. Mrenna, and P. Skands. “PYTHIA 6.4 Physics and Manual.” In: *JHEP* 0605 (2006), p. 026. doi: [10.1088/1126-6708/2006/05/026](https://doi.org/10.1088/1126-6708/2006/05/026). arXiv: [hep-ph/0603175 \[hep-ph\]](https://arxiv.org/abs/hep-ph/0603175).
- [76] T. Sjöstrand, S. Mrenna, and P. Skands. “A Brief Introduction to PYTHIA 8.1.” In: *Comput. Phys. Commun.* 178 (2008), p. 852. doi: [10.1016/j.cpc.2008.01.036](https://doi.org/10.1016/j.cpc.2008.01.036). arXiv: [0710.3820 \[hep-ph\]](https://arxiv.org/abs/0710.3820).
- [77] F. Zwicky. “Die Rotverschiebung von extragalaktischen Nebeln.” In: *Helvetica Physica Acta* 6 (1933), 110–127.
- [78] LHCb collaboration. “Observation of $J/\Psi p$ resonances consistent with pentaquark states in $\Lambda_b^0 \rightarrow J/\Psi K^- p$ decays.” In: (2015). doi: [10.1103/PhysRevLett.115.072001](https://doi.org/10.1103/PhysRevLett.115.072001). eprint: [arXiv:1507.03414](https://arxiv.org/abs/1507.03414).
- [79] T. S. van Albada, J. N. Bahcall, K. Begeman, and R. Sancisi. “Distribution of dark matter in the spiral galaxy NGC 3198.” In: *The Astrophysical Journal* 295 (Aug. 1985), pp. 305–313. doi: [10.1086/163375](https://doi.org/10.1086/163375).